

Surface spectroscopy of model catalysts

Citation for published version (APA):

Jong, de, A. M. (1994). *Surface spectroscopy of model catalysts*. [Phd Thesis 1 (Research TU/e / Graduation TU/e), Chemical Engineering and Chemistry]. Technische Universiteit Eindhoven.
<https://doi.org/10.6100/IR420369>

DOI:

[10.6100/IR420369](https://doi.org/10.6100/IR420369)

Document status and date:

Published: 01/01/1994

Document Version:

Publisher's PDF, also known as Version of Record (includes final page, issue and volume numbers)

Please check the document version of this publication:

- A submitted manuscript is the version of the article upon submission and before peer-review. There can be important differences between the submitted version and the official published version of record. People interested in the research are advised to contact the author for the final version of the publication, or visit the DOI to the publisher's website.
- The final author version and the galley proof are versions of the publication after peer review.
- The final published version features the final layout of the paper including the volume, issue and page numbers.

[Link to publication](#)

General rights

Copyright and moral rights for the publications made accessible in the public portal are retained by the authors and/or other copyright owners and it is a condition of accessing publications that users recognise and abide by the legal requirements associated with these rights.

- Users may download and print one copy of any publication from the public portal for the purpose of private study or research.
- You may not further distribute the material or use it for any profit-making activity or commercial gain
- You may freely distribute the URL identifying the publication in the public portal.

If the publication is distributed under the terms of Article 25fa of the Dutch Copyright Act, indicated by the "Taverne" license above, please follow below link for the End User Agreement:

www.tue.nl/taverne

Take down policy

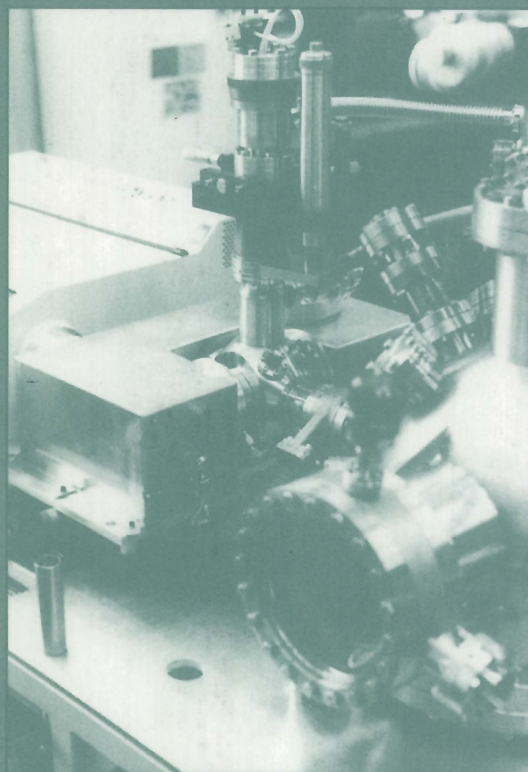
If you believe that this document breaches copyright please contact us at:

openaccess@tue.nl

providing details and we will investigate your claim.

Surface spectroscopy of model catalysts

A.M. de Jong



Surface spectroscopy of model catalysts

Proefschrift

ter verkrijging van de graad van doctor aan de Technische Universiteit Eindhoven, op gezag van de Rector Magnificus, prof.dr. J.H. van Lint, voor een commissie aangewezen door het College van Dekanen in het openbaar te verdedigen op dinsdag 6 september 1994 om 16.00 uur

door

A.M. de Jong

geboren te Dordrecht

Dit proefschrift is goedgekeurd door de promotoren:

prof.dr. R.A. van Santen

en

prof.dr. J.A.R. van Veen

copromotor: dr. J.W. Niemantsverdriet

CIP-GEGEVENS KONINKLIJKE BIBLIOTHEEK, DEN HAAG

Jong, Arie Martin de

Surface spectroscopy of model catalysts / Arie Martin de
Jong. - Eindhoven : Technische Universiteit Eindhoven
Proefschrift Eindhoven. - Met lit. opg. - Met samenvatting
in het Nederlands.

ISBN 90-386-0383-5

Trefw.: katalysatoren ; spectroscopie.



The work described in this thesis has been carried out at the Schuit Institute of Catalysis, Laboratory of Inorganic Chemistry and Catalysis, Eindhoven University of Technology (The Netherlands). Financial support has been supplied by the Netherlands Organization for Scientific Research (NWO, PGS 70-154).

voor Jet

Contents

1	Introduction	
1.1	Heterogeneous catalysis	1
1.2	Model systems in catalyst characterization	1
1.3	Scope of this thesis	3
2	Preparation and surface characterization of silica supported ZrO₂ catalysts; comparison of layered model systems with powder catalysts	
2.1	Introduction	5
2.2	Experimental	7
2.2.1	Catalyst preparation	7
2.2.2	Techniques	8
2.3	Results and discussion	9
2.3.1	ZrO ₂ /SiO ₂ powder catalysts	9
2.3.2	SiO ₂ /Si(100) model support	17
2.3.3	ZrO ₂ /SiO ₂ /Si(100) model catalysts	24
2.4	Concluding remarks	35
3	Sulfidation mechanism of molybdenum catalysts supported on an SiO₂/Si(100) model support, studied by surface spectroscopy	
3.1	Introduction	37
3.2	Experimental	39
3.2.1	Model catalysts	39
3.2.2	Techniques	39
3.3	Results	40
3.3.1	Fresh model catalyst	40
3.3.2	Reduction of MoO ₃ /SiO ₂ /Si(100)	44
3.3.3	Sulfided model catalysts	45
3.4	Discussion	50
3.5	Final remarks	56
4	Reflection absorption infrared spectroscopy	
4.1	Introduction	59
4.2	Theoretical considerations for the RAIRS experiment	59
4.3	Vibrational frequency of molecules adsorbed on metal surfaces	65
4.4	Intensity and line shape of infrared absorption bands	67

5	Apparatus for reflection absorption infrared spectroscopy on metal single crystals	
5.1	Introduction	69
5.2	Techniques	69
5.2.1	Reflection absorption infrared spectroscopy	69
5.2.2	Low energy electron diffraction	70
5.2.3	Auger electron spectroscopy	73
5.2.4	Thermal desorption spectroscopy	75
5.3	Instrumentation	77
5.3.1	UHV system	77
5.3.2	RAIRS instrumentation	79
5.3.3	LEED/AES optics	81
5.3.4	Mass spectrometer	84
5.3.5	Sample manipulation	85
5.4	RAIRS on miscellaneous adsorbate systems	88
5.4.1	Adsorption of CO on Rh(100) at high pressure	89
5.4.2	Adsorption and desorption of NO on Rh(100) with coadsorbed CO	90
5.4.3	Adsorption of ethylene and acetonitrile on Rh(100)	92
5.5	Conclusions	93
6	Adsorption of CO on Rh(100) studied with reflection absorption infrared spectroscopy	
6.1	Introduction	95
6.2	Experimental	97
6.2.1	Apparatus	97
6.2.2	Sample preparation and experimental conditions	98
6.3	Results	99
6.3.1	LEED	99
6.3.2	TDS	100
6.3.3	RAIRS	103
6.4	Discussion	110
6.5	Conclusions	118
7	Summary and conclusions	121
	Samenvatting	125
	Publications	128
	Dankwoord	129
	Curriculum vitae	130

1 Introduction

1.1 Heterogeneous catalysis

During the last decades catalysis has become more and more important in the synthesis of chemical products and in pollution control. Nowadays the majority of chemical products and processes is based on catalysis [1]. Catalysts provide new synthesis routes that are economically more attractive, due to the use of lower cost raw materials or less energetic processes. The use of highly selective catalytic processes results in a reduction of waste products. Catalysts are also widely used in the emission control of chemical plants and automotive exhaust gases.

In heterogeneous catalysis a catalytic reaction proceeds as follows. The reactants adsorb on the catalyst surface, where the intramolecular bonds of the reactants are broken or weakened. Then the adsorbed species react on the surface and the formed reaction products desorb, thereby regenerating the catalytic surface. Figure 1.1 shows an example of a typical catalytic reaction with gaseous reactants. The function of the catalyst is to provide an energetically favourable path for the reaction, in which the activation barriers for the intermediate steps are low compared to the activation energy of the gas phase reaction [2].

The catalytically active phase might be a metal, oxide, sulfide, etcetera. In many cases this active phase is supported on an oxidic material of high mechanical and thermal stability and with a high specific surface area.

1.2 Model systems in catalyst characterization

In heterogeneous catalysis the properties of a catalyst are largely determined by the atomic composition and structure of the surface, which are influenced by the preparation of the catalyst and by reaction and process conditions. Therefore, catalyst characterization with surface sensitive spectroscopic techniques yields relevant information on the performance of a catalyst. Since most catalysts are very complex systems, it is often difficult to apply these surface spectroscopies to their full potential. Model systems, then, provide a good means to study catalytic properties on a microscopic scale. Figure 1.2 shows a schematic drawing of a catalyst and some model systems.

Since most catalysts are not only complex but also insulating materials, it is difficult to obtain data of good quality with many surface spectroscopies, which make use of charged particles e.g. ions or electrons. Sample charging can be avoided by using model supports, consisting of a flat conducting substrate with a thin oxide layer of a few nanometres thick

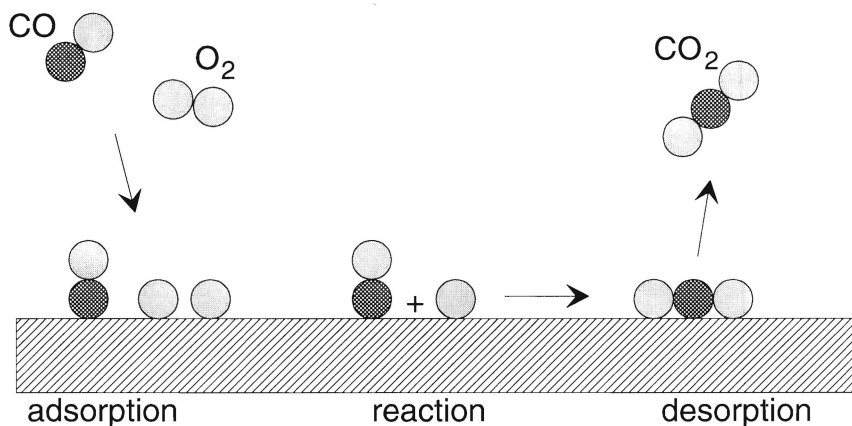


Figure 1.1

Schematic representation of a typical catalytic reaction; the oxidation of carbon monoxide. Carbon monoxide adsorbs molecularly on the surface and oxygen dissociatively. The adsorbed carbon monoxide molecules react with the oxygen atoms and a carbon dioxide molecule is formed, which desorbs from the surface.

on top of it. The active catalytic phase is then applied on this model support, usually by evaporation [3-5] or adsorption and decomposition of volatile compounds [6,7] like metal carbonyls. Such a model catalyst can also be prepared by the common wet chemical techniques as used in the practical preparation of catalysts supported on porous silica or alumina [8,9]. An additional advantage of these model catalysts is that, since they are flat, now depth sensitive information can be obtained.

On well defined single crystals the structure and composition of the surface are usually known on the atomic scale. Single crystals are used as a model for the active phase of the catalyst and make it possible to study all kinds of fundamental aspects involved in catalytic processes, e.g. adsorption and desorption mechanisms. This surface science approach in examining catalytic reactions is widely used and yields information about sites that are occupied by adsorbates and reactants, reaction intermediates and activation energies for reaction and desorption. These studies can be applied under ultra high vacuum (UHV) as well as under high pressure conditions. Most surface science techniques, using electrons or ions, cannot be performed at high pressures. However, surface techniques based on the interaction with electromagnetic radiation are applicable at high pressure conditions. Hence, such techniques could provide a link between single crystal studies and catalytic processes under realistic conditions.

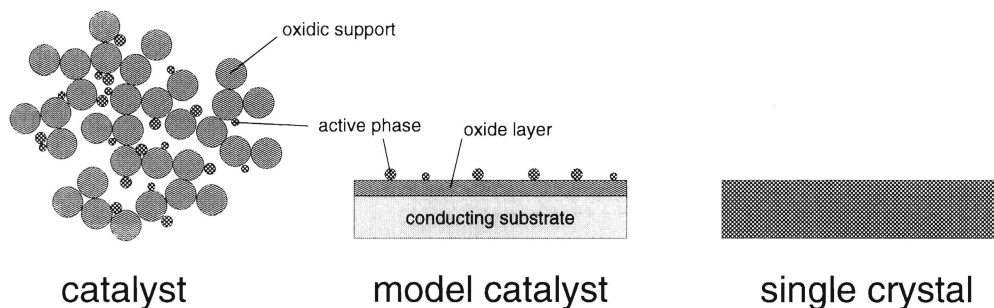


Figure 1.2

Schematic drawing of a catalyst and two model systems. The catalyst consists of an oxidic porous support on which the catalytically active particles are dispersed. The model catalyst consists of a conducting substrate with a thin oxide layer on which the active phase is applied. The single crystal models the active phase of the catalyst with a specific surface orientation.

1.3 Scope of this thesis

The primary goal of our research was the exploration of the possibilities of model catalysts, prepared by wet chemical techniques, for catalyst characterization. In Chapter 2 a study of the preparation of silica supported zirconium dioxide catalysts with surface spectroscopies is described. Two wet-chemical routes are compared to prepare a silica supported zirconia catalyst as well as a zirconia model catalyst. It is demonstrated that the results obtained on the model catalyst are comparable to those of the practical catalyst. However, the results of the model system enable a more detailed analysis.

The approach of using model catalysts prepared by wet chemical techniques has also been applied to study the sulfurization mechanism of silica supported molybdenum hydrodesulfurization catalysts, as described in Chapter 3. Molybdenum based hydrotreating catalysts are used in the oil refinery industry for the removal of sulfur from the heavier oil fractions. Sulfur removal is important for two reasons. From an environmental point of view, fuels should not contain any sulfur. Further, sulfur poisons other catalysts used in the subsequent upgrading processes. In the activation of the hydrotreating catalyst, sulfurization of molybdenum oxide to molybdenum sulfide is an essential step. We studied this sulfurization mechanism with atomic force microscopy (AFM), Rutherford backscattering spectrometry (RBS), X-ray photoelectron spectroscopy (XPS) and secondary ion mass spectrometry (SIMS). AFM gives information about the morphology of the surface. The concentration of species on the surface can be measured with RBS. XPS yields the oxidation states of molybdenum and sulfur that occur during the sulfurization and SIMS provides

information about the coordination of the molybdenum. The information obtained by using these model catalysts could not directly be obtained from the industrial catalysts, because of the electrical charging of practical catalysts.

The second goal was to develop an apparatus to perform vibrational spectroscopy on molecules adsorbed on metal single crystal surfaces. From the most commonly used vibrational spectroscopies, infrared spectroscopy and electron energy loss spectroscopy (EELS) are the most suited to study adsorbed molecules on a surface. The advantage of infrared spectroscopy is that it is applicable at higher pressures, which EELS is not, since it employs electrons. The disadvantage of infrared spectroscopy is that it is difficult to measure low vibrational modes (i.e. lower than 800 cm^{-1}). Infrared spectroscopy of species adsorbed on metal surfaces has to be performed in reflection since metals are opaque for infrared light. This technique is called reflection absorption infrared spectroscopy (RAIRS) [10]. Chapter 4 describes the principles of this technique. The resolution obtained in RAIRS spectra is much better than with EELS. Therefore, data obtained with RAIRS will have a significant contribution in evaluating vibrational data of adsorbed species reported in the literature. Most of these data were earlier provided by EELS measurements.

The apparatus consists of an UHV chamber, equipped with techniques for sample cleaning and characterization, and a separate cell for the RAIRS experiments. In the UHV chamber the surface structure of the sample and of adsorbates can be studied with low energy electron diffraction (LEED) and desorption products can be measured as a function of the temperature with a mass spectrometer. The RAIRS cell can be isolated from the UHV chamber allowing for RAIRS experiments up to one atmosphere. In Chapter 5 the apparatus is described and the performance is demonstrated for several adsorption systems, while Chapter 6 deals with the adsorption of carbon monoxide on rhodium with a (100) surface orientation, examined with RAIRS, LEED and thermal desorption spectroscopy (TDS).

References

- [1] J.A. Cusumano in *Perspectives in catalysis*, J.M. Thomas and K.I. Zamaraev, Eds.; Blackwell scientific publications, London, p. 1, 1992.
- [2] J.W. Niemantsverdriet, *Spectroscopy in catalysis*, VCH, Weinheim, 1993.
- [3] L.H. Dubois, P.K. Hansma and G.A. Somorjai, *Appl. Surf. Sci.* **6**, 173 (1980).
- [4] P.A. Spevack and S. McIntyre, *Appl. Catal.* **64**, 191 (1990).
- [5] D.N. Belton, Y.-M. Sun and J.M. White, *J. Phys. Chem.* **88**, 5172 (1984).
- [6] B.G. Frederick, G. Apai and T.N. Rhodin, *J. Am. Chem. Soc.* **109**, 4797 (1987).
- [7] D.N. Belton and S.J. Schmieg, *Appl. Surf. Sci.* **32**, 173 (1988).
- [8] A. Jiménez-González and D. Schmeisser, *J. Catal.* **130**, 332 (1991).
- [9] J. Nickl, R. Schlögl, A. Baiker, H. Knözinger and G. Ertl, *Catal. Lett.* **3**, 379 (1989).
- [10] R.G. Greenler, *J. Chem. Phys.* **44**, 310 (1966).

2 Preparation and surface characterization of silica supported ZrO₂ catalysts; comparison of layered model systems with powder catalysts*

Abstract

The preparation of technical ZrO₂/SiO₂ catalysts has been studied by surface spectroscopic techniques. The reaction of zirconium ethoxide, dissolved in ethanol, with the hydroxyl groups of the silica support yields a well dispersed ZrO₂/SiO₂ catalyst with a satisfactory thermal stability. Preparation by incipient wetness impregnation from an aqueous zirconium nitrate solution results in a much less dispersed and less thermally stable catalyst.

Since these oxidic materials are insulators, most surface spectroscopic techniques like X-ray photoelectron spectroscopy (XPS) and secondary ion mass spectrometry (SIMS) are seriously limited by charging effects. In order to explore the possibilities that flat conducting models offer for surface analysis, the preparation was repeated on model supports consisting of a thin layer of SiO₂ on a silicon single crystal. The same wet chemical preparation methods were used as in the preparation of technical catalysts. Auger depth profiling and angle-dependent XPS confirm that catalysts prepared by the reaction between zirconium ethoxide and hydroxyl groups on the SiO₂ contain a highly dispersed zirconium phase that is converted to ZrO₂ upon calcination. The results are in good agreement with those on ZrO₂ catalysts on porous silica supports. The advantage of model catalysts is that surface spectroscopies can be used to their full potential.

2.1 Introduction

In heterogeneous catalysis, the performance of a catalyst is largely determined by the atomic composition and structure of the surface. Identification of factors in the preparation which influence the surface structure of the eventual catalyst, is an important goal of catalyst characterization. Surface sensitive spectroscopies such as XPS, Static SIMS and Auger electron spectroscopy (AES) are able to yield relevant information on this subject.

* The content of this chapter has been published: A.C.Q.M. Meijers, A.M. de Jong, L.M.P. van Gruijthuisen and J.W. Niemantsverdriet, *Appl. Catal.* **70**, 53 (1991), L.M. Eshelman, A.M. de Jong and J.W. Niemantsverdriet, *Catal. Lett.* **10**, 201 (1991) and A.M. de Jong, L.M. Eshelman, L.J. van IJzendoorn and J.W. Niemantsverdriet, *Surf. Int. Anal.* **18**, 412 (1992).

The applicability of surface spectroscopic techniques on oxide supported, insulating catalysts is often limited by inhomogeneous charging, which causes shifted and broadened peaks in XPS and AES spectra and makes detection of secondary ions in SIMS difficult. Sample charging can be avoided with model catalysts by using a silicon or aluminum crystal with an oxidized layer of a few nanometres thick as a model support [1-5]. The active phase is usually deposited onto the support by evaporation [1-3] or by adsorbing volatile metal compounds like carbonyls, which are then decomposed [4,5]. However, model catalysts can also be prepared by the common wet chemical techniques that are used in the preparation of technical catalysts [6,7]. In this chapter this is illustrated for the catalyst system $\text{ZrO}_2/\text{SiO}_2$.

Zirconium oxide catalysts are of interest for a great number of catalytic processes such as isosynthesis, methanol synthesis and catalytic cracking [8,9]. Because of its amphoteric character zirconia is also attractive as a support material. In methanol synthesis the selectivity to methanol is much higher for zirconia supported catalysts than for most catalysts with another support [10]. In steam reforming and Fischer-Tropsch synthesis inclusion of zirconia in the support improves the thermal and hydrothermal stability. Catalysts used in oil refinery processes require frequent regeneration. To minimise the loss of activity the supports are stabilized with zirconia, which makes them more resistant to sintering. Zirconia is also used in complete oxidation reactions, such as in the auto exhaust catalyst, because of its ability to stabilize the active metal at high operation temperatures against diffusion into the support [11].

Highly dispersed zirconium oxide on a silica support is of special interest, because this system combines the chemical properties of zirconium oxide with the mechanical stability and high surface area of the silica support [12-14]. Such a $\text{ZrO}_2/\text{SiO}_2$ system can be prepared by means of two methods: incipient wetness impregnation from an aqueous solution of zirconium nitrate, and a surface reaction between a suitable zirconium compound and hydroxyl groups of the silica support, after which the zirconium oxide is formed by heating in air. Here we used zirconium ethoxide for this purpose. We used XPS and SIMS to study the preparation of the catalysts. As XPS is surface sensitive, the XPS Zr/Si intensity ratio reflects the dispersion of the ZrO_2 over the SiO_2 . The catalyst prepared by the second method appears to have a higher dispersion and to be more thermostable than the catalyst prepared by incipient wetness impregnation.

To make a ZrO_2 model catalyst on a $\text{SiO}_2/\text{Si}(100)$ support, we use the same two wet chemical preparation techniques as we used for the porous $\text{ZrO}_2/\text{SiO}_2$ system. First we examine this model support with angle-dependent XPS and Static SIMS. Next we use angle-dependent XPS, Static SIMS and AES depth profiling to study the effect of the preparation method on the morphology of the $\text{ZrO}_2/\text{SiO}_2/\text{Si}(100)$ model catalyst, and compare the results with those obtained on the porous $\text{ZrO}_2/\text{SiO}_2$ catalysts. Finally, Rutherford backscattering spectrometry is used to determine the surface concentration of the ZrO_2 on the $\text{ZrO}_2/\text{SiO}_2/\text{Si}(100)$ model catalyst. The work illustrates that flat, conducting model supports

offer good possibilities for studying supported catalysts in a way that surface spectroscopies are used to their full potential. In particular, Auger depth profiling and take-off angle-dependent XPS become feasible because the direction perpendicular to the surface is defined.

2.2 Experimental

2.2.1 Catalyst preparation

An 8 wt% $\text{ZrO}_2/\text{SiO}_2$ catalyst was prepared by pore volume impregnation of 5 grams of silica (Grace 322, surface area $250 \text{ m}^2/\text{g}$) with 8 ml zirconium nitrate (BDH Chemicals Ltd.) solution in water with a concentration of 150 g/l. Catalysts with a 16 and 24 wt% loading were made by applying sequential impregnation steps. These samples were dried at $40 \text{ }^\circ\text{C}$ and next calcined in air at temperatures up to $700 \text{ }^\circ\text{C}$. These catalysts were used for thermal stability studies with XPS. A fourth nitrate derived sample with a ZrO_2 loading of 20 wt% was made by one step incipient wetness impregnation. This sample was used for SIMS. We also prepared a 16 wt% catalyst by letting zirconium ethoxide react with the OH groups of the silica surface: 5 g of silica was added to a solution of 2 g of zirconium ethoxide (97%, Aldrich Chemicals Co.) in 70 ml of ethanol p.a. and 1 ml concentrated acetic acid. It is imperative to use water free ethanol to prevent precipitation of zirconium hydroxide. The mixture was stirred overnight and filtrated afterwards. The loading of this catalyst, determined by comparing the weight of this catalyst after calcination at $680 \text{ }^\circ\text{C}$ with that of the untreated silica after calcination at $680 \text{ }^\circ\text{C}$, was $16 \pm 0.5 \text{ wt}\%$ of ZrO_2 . This catalyst, dried at $40 \text{ }^\circ\text{C}$ and next calcined in air at temperatures up to $700 \text{ }^\circ\text{C}$, was used for thermal stability studies with XPS. A second ethoxide derived catalyst was made with an approximately fivefold diluted solution and had a loading of about $9 \pm 1.5 \text{ wt}\%$ ZrO_2 . This catalyst was used for SIMS.

As a model support we used a silicon single crystal ($10 \times 10 \times 1 \text{ mm}$) with a (100) surface orientation. First, the crystal was sputter-cleaned with 6 keV Ar^+ ions and then oxidized at $500 \text{ }^\circ\text{C}$ in air for 12 hours. The impregnated model catalyst was prepared by placing a drop of an aqueous solution of zirconium nitrate with a concentration of 0.015 g/l on the oxidized silicon crystal. The excess solution was removed by holding a paper tissue against the edge of the crystal. In this way we obtained a very thin film of solution on the model support. The model for the zirconium ethoxide derived catalyst was prepared by soaking the silicon crystal in a solution of 0.1 g zirconium ethoxide in 50 ml ethanol p.a. and 0.5 ml concentrated acetic acid. The solution was stirred slowly and heated to $70 \text{ }^\circ\text{C}$. After 15 minutes the sample was taken out of the solution and rinsed with ethanol p.a. at room temperature to remove unreacted zirconium ethoxide. The samples were dried at $40 \text{ }^\circ\text{C}$ and calcined in air at temperatures up to $480 \text{ }^\circ\text{C}$. These samples were used for angle-dependent

XPS measurements.

The impregnated model systems that were used for the AES and SIMS measurements were prepared by placing a drop of an aqueous solution of zirconium nitrate with a concentration of 0.045 g/l on the model support. These samples were allowed to dry in an evacuated desiccator. While the drop dried in such a manner that the edges were heavily loaded, in the centre of the samples the zirconium was distributed more uniformly and this was the region chosen for study. The ethoxide derived catalysts were prepared by soaking the silicon wafer in a solution of 2.4 g zirconium ethoxide, 20 ml ethanol and 1 ml acetic acid for 15 minutes at 70 °C. The samples were rinsed to remove unreacted ethoxide and oxidized in a tube furnace for 5 minutes at 500 °C in a flow of 10% O₂ in N₂. A small chlorine contaminant corresponding to 0.1 - 0.3 of a monolayer, originating from the tube furnace, was detected with AES on a few of the samples after the oxidation treatment.

2.2.2 Techniques

XPS spectra were obtained with a VG Escalab 200 spectrometer equipped with a monochromatic Al K α source, a hemispherical analyzer connected to a five channel detector and a manipulator which enables one to vary the take-off angle between 0 and 90 degrees. XPS spectra of the model support and the model catalysts were measured at 20 eV pass energy and those of the powder catalysts at 50 eV pass energy. Measuring the powder catalysts at lower pass energy did not result in narrower peaks. The porous catalysts were pressed in indium foil. Charging was corrected for by using the C1s peak at 284.6 eV as a reference.

Static SIMS spectra were measured with a Leybold SSM200 spectrometer. We used a 2 keV Ar⁺ primary ion beam with a current density of 10 nA/cm²s for the model catalysts. The powder catalysts were pressed in Indium foil and here we used a 5 keV primary ion beam with a current density of 3 μ A/cm²s. Charge compensation was not employed.

Auger depth profiling was performed in a Physical Electronics 550 spectrometer equipped with a double pass cylindrical mirror analyzer collecting the electron excited Auger spectra while the surface was bombarded with 5 keV Ar⁺ ions. The argon beam was rastered over an area of 6 \times 6 mm around the point of impact of the electron beam (energy 3 keV, diameter approximately 1 mm).

RBS spectra were measured with an incident beam of 3.94 MeV He⁺ produced with the AVF-cyclotron at Eindhoven University of Technology [15]. Details concerning the He beam optics, detectors and scattering geometry have been published elsewhere [16,17].

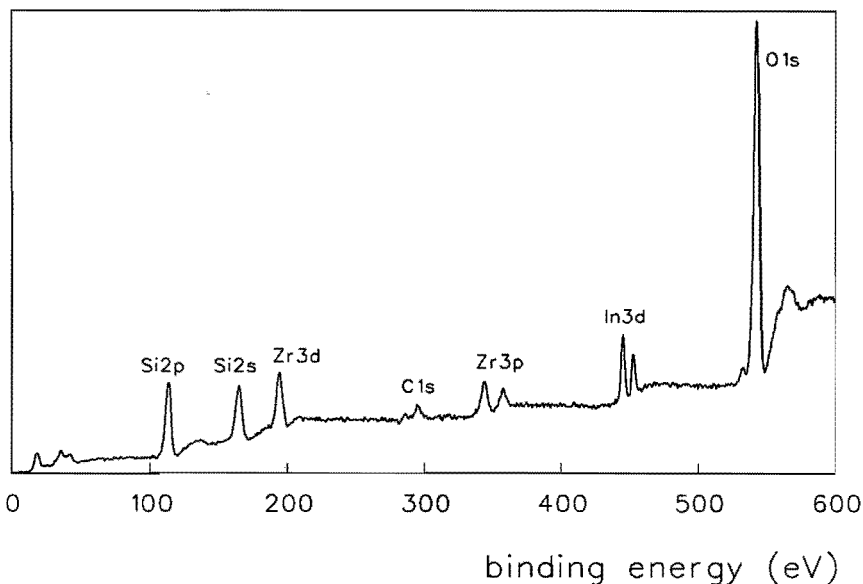


Figure 2.1

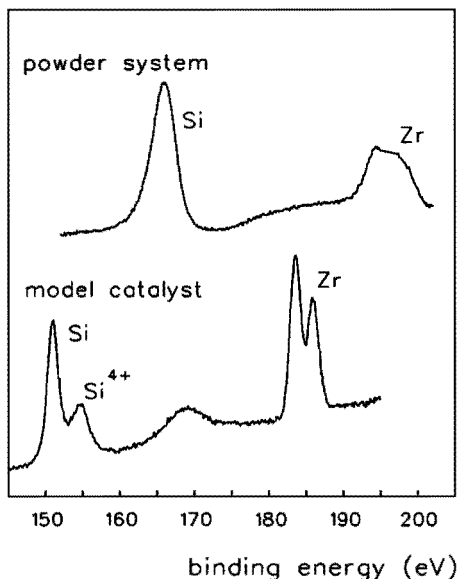
XPS spectrum of a $\text{ZrO}_2/\text{SiO}_2$ catalyst.

2.3 Results and discussion

2.3.1 $\text{ZrO}_2/\text{SiO}_2$ powder catalysts

XPS is based on the photoelectric effect. A substance radiated with X-rays will emit core electrons. The binding energy of these electrons is characteristic of the element they originate from, and of the chemical state of this element. An XPS spectrum thus shows the intensity of the emitted electrons as a function of the binding energy. Since the mean free path of electrons in a solid is small, only electrons from the surface region will be detected. Figure 2.1 shows a typical XPS spectrum of a $\text{ZrO}_2/\text{SiO}_2$ catalyst. At 110 and 165 eV we see the Si 2p and Si 2s peaks of the support. The Zr 3d peak is at 195 eV and the peaks at 345 and 360 eV originate from the Zr 3p doublet. As the samples were pressed in indium foil, we also see the peaks at 445 and 453 eV of the In 3d doublet. At 285 and 530 eV we see the peaks of C 1s and O 1s respectively originating from the indium foil. The C 1s and O 1s peaks of the charged catalyst appear at 295 and 540 eV.

As silica supported zirconia is an insulator, its XPS spectrum is affected by charging. This is illustrated in Figure 2.2, where we compare XPS spectra in the range between 150 and

**Figure 2.2**

XPS spectra in the range of the Si 2s and Zr 3d peaks of a real $\text{ZrO}_2/\text{SiO}_2$ catalyst (top) and of a conducting model system of ZrO_2 on a support consisting of a 2 nm thick layer of SiO_2 on a Si wafer (bottom), showing the effect of electrical charging. The spectrum of the real catalyst exhibits a charge shift of about 11 eV and is severely broadened in comparison to that of the model catalyst. Note that the spectrum of the latter contains two Si 2s peaks, one at about 151 eV for zero-valent Si from the substrate and the other at about 154.5 eV for Si^{4+} from the SiO_2 layer.

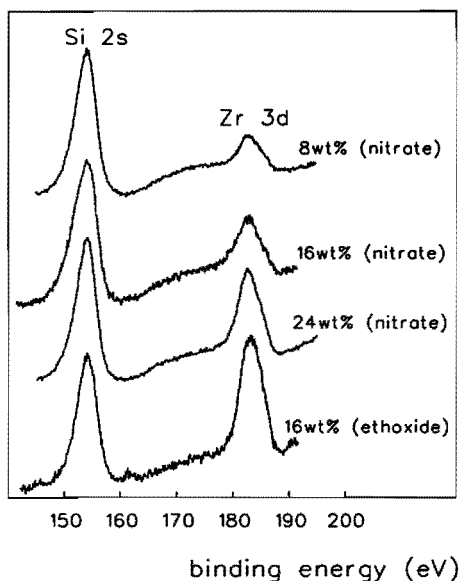
200 eV of a $\text{ZrO}_2/\text{SiO}_2$ catalyst and an electrically conducting model system. The spectrum of the real catalyst shows a single broad Si 2s peak at about 166 eV and a poorly resolved Zr 3d doublet with the $3d_{5/2}$ component at about 195 eV. The expected values for Si 2s of SiO_2 and Zr $3d_{5/2}$, however, are about 12 eV lower, 154 and 182.4 eV [18], respectively. Charge shifts observed in the XPS spectra of the other $\text{ZrO}_2/\text{SiO}_2$ samples ranged from 8 to 25 eV, depending on the amount of catalyst powder present on the indium sample holder. The use of a monochromatic X-ray source causes this shift to be so large. The sample is not in line of sight of the actual source which makes it impossible for secondary stray electrons from the source to compensate for the charging as in a conventional source. Charging was considerably more severe in reference samples of pure zirconium ethoxide, nitrate and oxide, from which XPS spectra could not be obtained at all.

The XPS spectrum of a conducting $\text{ZrO}_2/\text{SiO}_2/\text{Si}$ model catalyst, on the other hand (Figure 2.2), exhibits a sharp and well resolved Zr 3d doublet with a Zr $3d_{5/2}$ binding energy of 183.4 eV, a Si 2s peak for the oxide layer at 155 eV as well as one at 151 eV for the

Table 2.1

XPS intensity ratio of the N 1s and Si 2s peaks of the $\text{ZrO}_2/\text{SiO}_2$ catalysts prepared from zirconium nitrate for two calcination temperatures.

loading (wt %)	N 1s / Si 2s	
	110°C	200°C
8	3.9×10^{-2}	1×10^{-2}
16	7.2×10^{-2}	2×10^{-2}
24	12.0×10^{-2}	5×10^{-2}

**Figure 2.3**

XPS spectra in the range from 150 to 200 eV, showing the Zr 3d and Si 2s peaks of the ZrO₂/SiO₂ catalysts after calcination at 700 °C. All XPS spectra have been corrected for electrical charging by positioning the Si 2s peak at 154 eV. The spectra labeled 'nitrate' correspond to the catalysts prepared by incipient wetness impregnation with an aqueous solution of zirconium nitrate, the spectrum labeled 'ethoxide' to that prepared by the reaction of zirconium ethoxide with the hydroxyl groups of the silica support.

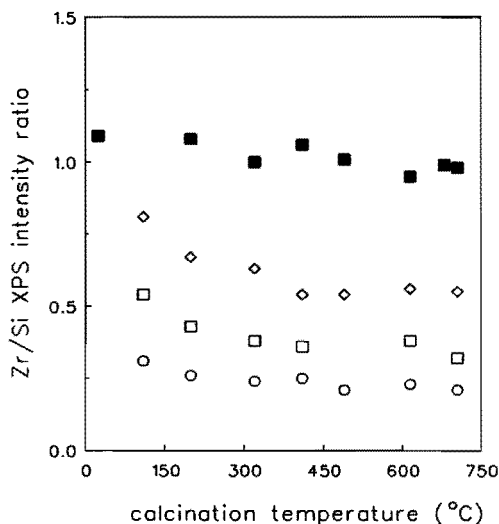
semi-conducting Si substrate. In this case the charge shift of both the ZrO₂ and the SiO₂ amounts to 1 eV only. The peak at 168 eV is a plasmon loss peak of Si 2s from the silicon substrate.

In order to investigate the thermal stability of the catalysts, XPS spectra were measured of the 8, 16, and 24 wt% ZrO₂/SiO₂ catalysts prepared from zirconium nitrate and the 16 wt% catalyst from ethoxide, as a function of calcination temperature. All spectra yielded a corrected Zr 3d_{5/2} binding energy in the range 182.5 ± 0.5 eV, which indicates that Zr is present in the 4+ oxidation state. O 1s spectra showed one broad peak at a corrected binding energy of 532.3 ± 0.3 eV. A weak N 1s signal with a binding energy of 407.3 eV consistent with the presence of nitrate [18], was observed in the spectra of the impregnated catalysts

Table 2.2

XPS intensity ratio of the C 1s and Si 2s peaks of the ZrO₂/SiO₂ catalysts prepared from zirconium ethoxide as a function of calcination temperature.

calcination temperature (°C)	C 1s / Si 2s
25	0.9±0.15
200	0.4±0.10
320	0.16±0.07
410	0.11±0.05
490	0.12±0.06
615	0.22±0.08
680	0.16±0.07

**Figure 2.4**

XPS Zr 3d / Si 2s intensity ratios for the ZrO_2/SiO_2 catalysts from zirconium ethoxide (■: 16 wt%) and from zirconium nitrate (◇: 24 wt%, □: 16 wt%, ○: 8 wt%) as a function of calcination temperature.

after drying at 110 and 200 °C. The intensities compared to those of Si 2s are shown in Table 2.1. The spectra of the catalysts from ethoxide showed a broad C 1s signal at a binding energy of 284.6 eV. Contributions at higher binding energies which would be characteristic of ethoxide could not be detected due to a poor signal to noise ratio. The intensity of the C 1s signal compared to the Si 2s signal is given in Table 2.2. The data indicate that catalysts calcined at 320 °C and higher contain significantly less carbon than those calcined at lower temperatures.

Figure 2.3 shows XPS spectra of the ZrO_2/SiO_2 catalysts after calcination in air at 700 °C. All spectra were corrected for charging by positioning the Si 2s peak at a binding energy of

Table 2.3

Dispersion in ZrO_2/SiO_2 catalysts calcined at 700 °C as derived from the Zr 3d / Si 2s XPS intensity ratios by means of Kuipers' model [19].

loading (wt%)	Zr 3d / Si 2s	D %	A m^2/g	d nm	r nm
<i>catalysts from zirconium nitrate</i>					
8	0.22±0.01	12±1	5	2.7	6.0
16	0.37±0.04	8±1	7	4.2	9.5
24	0.55±0.02	7±0.5	9	4.8	10.8
<i>catalyst from zirconium ethoxide</i>					
16	1.0±0.05	75±15	67	0.42	0.95

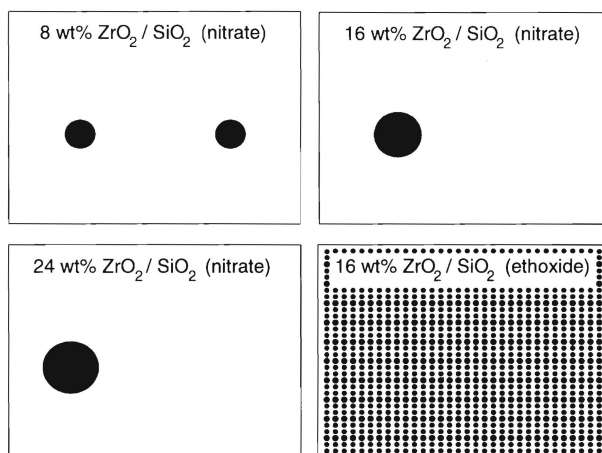


Figure 2.5

Schematic representation of the dispersion of ZrO_2 particles and the extent to which the silica support is covered in the case of the three $\text{ZrO}_2/\text{SiO}_2$ catalysts prepared by impregnation with an aqueous zirconium nitrate solution, and for the one prepared via an exchange reaction of the support with zirconium ethoxide. The rectangles represent 100 nm^2 of silica support area, the circles represent a half-spherical particle of ZrO_2 seen from above. See Table 2.3 for corresponding numbers.

154 eV. The intensity of the Zr signal relative to that of Si is determined by the ZrO_2 content of the catalyst and by its dispersion over the silica. For the three catalysts prepared from nitrate, Figure 2.3 shows that, as expected, the Zr intensity goes up as the ZrO_2 loading increases. Note however, that the Zr 3d intensity of the catalyst prepared from zirconium ethoxide is significantly larger than that of the nitrate derived catalyst with the same ZrO_2 loading. This proves that the dispersion of the catalyst from ethoxide is higher than that of the conventionally impregnated catalysts.

The Zr/Si XPS intensity ratios for the four catalysts treated at a number of calcination temperatures are given in Figure 2.4. The Zr/Si ratio of the catalyst from ethoxide decreases from about 1.1 for the freshly dried catalyst to about 1.0 for the catalysts calcined at around 700°C . The weak dependence of the Zr/Si intensity ratio on the calcination temperature indicates that the catalysts are rather stable with respect to sintering.

The $\text{ZrO}_2/\text{SiO}_2$ catalyst with the same loading, but prepared by incipient wetness impregnation exhibits not only a lower dispersion but also a lower thermal stability, as Figure 2.4 shows. The catalyst with the highest loading, 24 wt%, shows the largest decrease in Zr/Si ratio, whereas the Zr/Si ratio of the catalyst with 8 wt% ZrO_2 loading is almost constant. We further note that the most significant loss of dispersion occurs at calcination

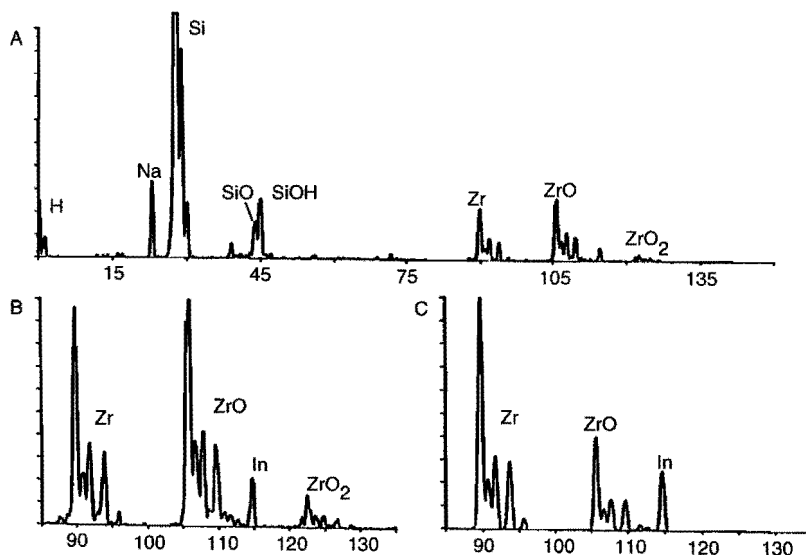


Figure 2.6

Positive SIMS spectrum of the 9 wt% ZrO_2/SiO_2 catalyst prepared from zirconium ethoxide, dried at 40 °C (A), and two spectra of the Zr-ZrO-ZrO₂ region for a dried catalyst (B) and a calcined one (C).

temperatures between 25 and 400 °C.

In order to interpret the Zr/Si ratios quantitatively, we have used the model published by Kuipers et al. [19]. These authors showed that for randomly oriented samples a unique relation exists between the XPS intensity ratio of the supported phase and the support on one hand and the dispersion of the supported phase on the other. Hence, the Zr/Si ratios of Figure 2.4 can be converted to dispersions, and to characteristic dimensions of some likely particle geometries: layers with a uniform thickness d , spheres with a diameter $2r$ ($=3d$) or half spheres with radius r ($=2.25d$). Table 2.3 summarizes these values for the catalysts which were calcined at 700 °C. Figure 2.5 presents a highly schematic but instructive visualisation of what the calculated dispersions and support coverages mean if the ZrO_2 particles were present in the form of half spheres.

When a substance is bombarded with a primary ion beam, secondary ions, neutrals and clusters are emitted from the surface. These secondary particles are detected with a mass spectrometer. The detected masses are plotted in a SIMS spectrum, showing the intensity of each mass. This reveals the elements present on the surface and clusters provide information about which elements are in direct contact with each other. From SIMS spectra the transformation to the zirconium oxide phase can be observed. Figure 2.6a shows a typical

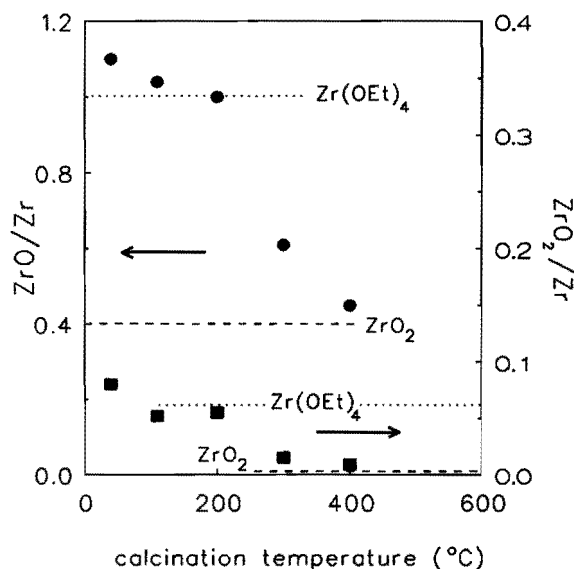


Figure 2.7

Positive SIMS ZrO^+/Zr^+ and $\text{ZrO}_2^+/\text{Zr}^+$ ratios as a function of calcination temperature for an 9 wt% $\text{ZrO}_2/\text{SiO}_2$ catalyst prepared from zirconium ethoxide, along with the ZrO^+/Zr^+ and $\text{ZrO}_2^+/\text{Zr}^+$ ratios measured from zirconium ethoxide and zirconium oxide reference samples.

positive SIMS spectrum of a catalyst prepared from zirconium ethoxide. It contains peaks of H^+ , C^+ , O^+ , Na^+ , Si^+ , K^+ , Ca^+ , SiO^+ , SiOH^+ , Zr^+ , ZrO^+ , ZrOH^+ , In^+ , and ZrO_2^+ . The relatively high intensities of Na, K and Ca are a well known artefact of SIMS; traces of these elements already give high yields in positive SIMS. The In^+ peak arises from the indium foil into which the catalyst powder was pressed. We also detected peaks from Hf^+ and HfO^+ (not shown), which is a well known impurity (1-3%) of zirconium [20].

We found that the most useful SIMS information is in the relative intensities of the Zr^+ , ZrO^+ , ZrOH^+ and ZrO_2^+ ions. This is illustrated in Figure 2.6b and Figure 2.6c which show the isotopic pattern of these ions of a freshly dried (Figure 2.6b) and a calcined (Figure 2.6c) catalyst. Note that the SIMS spectrum of the freshly dried catalyst contains small but significant contributions of ZrOH^+ ions, see for example the peaks at 107 amu ($^{90}\text{ZrOH}^+$ and $^{91}\text{ZrO}^+$) and 111 amu ($^{94}\text{ZrOH}^+$). ZrOH^+ is probably a fragment ion from zirconium ethoxide or acetate. In the sample which was calcined at 400 °C the isotopic pattern of ZrO resembles the pattern of Zr , indicating that no more ZrOH species are present.

Figure 2.7 shows the ZrO^+/Zr^+ and $\text{ZrO}_2^+/\text{Zr}^+$ ratios from the SIMS spectra for the ethoxide derived catalysts as a function of calcination temperature. We also included these ratios for zirconium ethoxide and zirconium oxide reference samples. Figure 2.7 clearly shows that catalysts prepared from zirconium ethoxide which were calcined below 200 °C have a ZrO^+/Zr^+ and $\text{ZrO}_2^+/\text{Zr}^+$ ratio about equal to that of the zirconium ethoxide reference compound. However, samples calcined above 300 °C have a ZrO^+/Zr^+ and $\text{ZrO}_2^+/\text{Zr}^+$ ratio which decreases towards that measured for ZrO_2 . Hence, the SIMS spectra clearly indicate

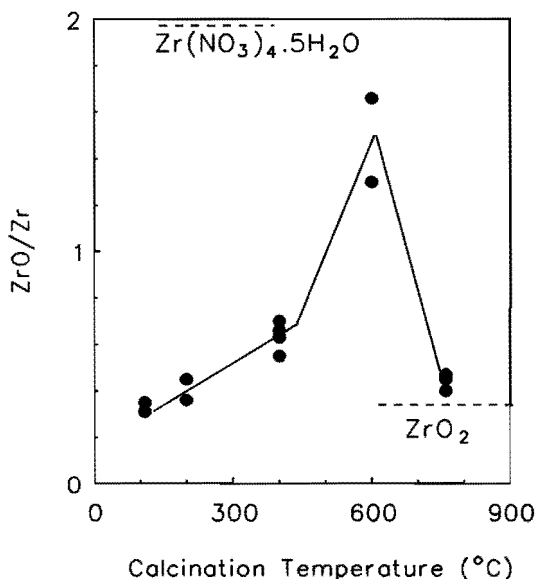


Figure 2.8

Positive SIMS ZrO^+/Zr^+ ratio for a 20 wt% ZrO_2/SiO_2 catalyst prepared by incipient wetness impregnation from an aqueous solution of zirconium nitrate, along with the ZrO^+/Zr^+ ratios from zirconium nitrate and zirconium oxide reference samples.

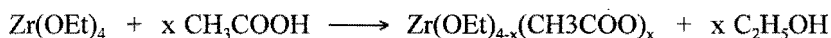
that the formation of ZrO_2 in catalysts prepared by ion exchange from zirconium ethoxide occurs during calcination in air at temperatures between 300 °C and 400 °C.

The SIMS spectra of the zirconium catalysts which were prepared by incipient wetness impregnation from a nitrate solution are of comparable quality as the spectra in Figure 2.6. The spectrum of the freshly prepared sample dried at 40 °C gives clear evidence that the Zr species present on the silica surface is not $Zr(NO_3)_4$. Pure $Zr(NO_3)_4$ has a high ZrO^+/Zr^+ ratio of about 2 (Figure 2.8). The ratio for the spectra of the fresh catalyst, however, is about 0.35, which is more characteristic of zirconium oxide or perhaps, hydroxide or oxyhydroxide. The ZrO^+/Zr^+ ratio increases at calcination temperatures above 400 °C and finally drops back to the value characteristic of ZrO_2 . The ZrO^+/Zr^+ ratio of the zirconium nitrate reference sample decreases continuously with time spent in the vacuum system, which is probably caused by decomposition of the nitrate [21].

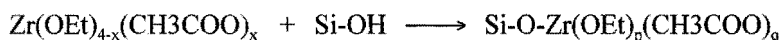
In negative SIMS the following species were observed: C^- , O^- , OH^- , H_2O^- , F^- , C_2^- , C_2H^- , $C_2H_2^-$, Si^- , SiO^- , $SiOH^-$, SiO_2^- , ZrO^- and ZrO_2^- . No higher ethoxide fragments nor any nitrate fragments were found. A major problem is that a number of potentially interesting ions have the same masses, e.g. SiO^- and CO_2^- (mass 44) and $SiOH^-$ and $C_2H_5O^-$ (mass 45).

Concluding we state that the most important difference between a ZrO_2/SiO_2 catalyst prepared via the ethoxide-hydroxyl reaction and one prepared by incipient wetness impregnation is the much higher dispersion of the former. XPS shows that a 16 wt% ZrO_2/SiO_2 catalyst from ethoxide has a dispersion of typically 75% whereas the dispersion of a 16 wt% ZrO_2/SiO_2 catalyst from nitrate is an order of magnitude lower (Table 2.3). XPS

also shows (Figure 2.4) that the ethoxide derived catalyst has a higher thermostability. We propose that the formation of ZrO₂ from zirconium ethoxide on silica takes place in the following way. In the solution of zirconium ethoxide and acetic acid in ethanol, ethoxide and acetate groups interchange according to the reaction:



This is a well-known reaction of metal alkoxides with organic acids and it increases the solubility of zirconium ethoxide. The value of *x* is small, typically 1 [22]. When the silica is added, the following reaction takes place:



During calcination between 200 °C and 300 °C, zirconium ethoxide/acetate is decomposed and ZrO₂ begins to form. This is concluded from the decrease in carbon content observed with XPS (Table 2.2) and the decreasing ZrO⁺/Zr⁺ and ZrO₂⁺/Zr⁺ ratios in SIMS (Figure 2.7). After calcination at 400 °C the formation of ZrO₂ is complete.

The catalyst prepared from zirconium nitrate behaves quite differently. The Zr/Si XPS intensity ratio indicates that the initially deposited Zr phase has characteristic dimensions on the order of a few nm (Table 2.3). Upon calcination some loss of dispersion occurs (Figure 2.4). The final dispersion of the catalysts is below 10%. The SIMS spectra and in particular the ZrO⁺/Zr⁺ ratios (Figure 2.8) indicate that at least the majority of the phase deposited on the silica during impregnation is not zirconium nitrate but probably zirconium hydroxide or oxyhydroxide. Nitrate groups are nevertheless present after impregnation and disappear at 200 °C (Table 2.1). These results on both, the ethoxide and nitrate derived catalysts, are in good agreement with the results from infrared and temperature programmed oxidation experiments [23].

2.3.2 SiO₂/Si(100) model support

First we address the question whether a thin layer of SiO₂ on Si(100) is an acceptable model for high surface area SiO₂. The Si 2p XPS peaks of the model support are shown in Figure 2.9. One can clearly see the oxidic Si 2p peak grow upon higher oxidation temperature as the oxide layer becomes thicker. At the same time the oxidic Si 2p peak shifts from 102.8 eV to 103.4 eV. The latter is the binding energy of a Si⁴⁺ peak in amorphous silica [24]. From this we conclude that it is important to oxidize the model support at a high enough temperature, e.g. 500 °C, in order to get a type of oxide, which gives at least the Si 2p binding energy of a silica support.

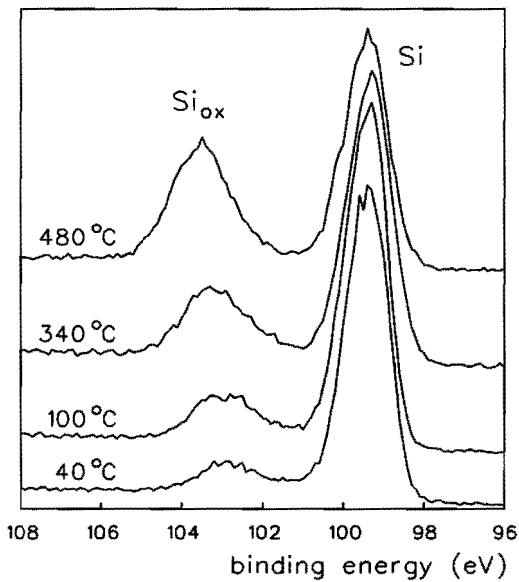


Figure 2.9

XPS spectra of the Si 2p region measured on the SiO_x/Si(100) model support for different oxidation temperatures.

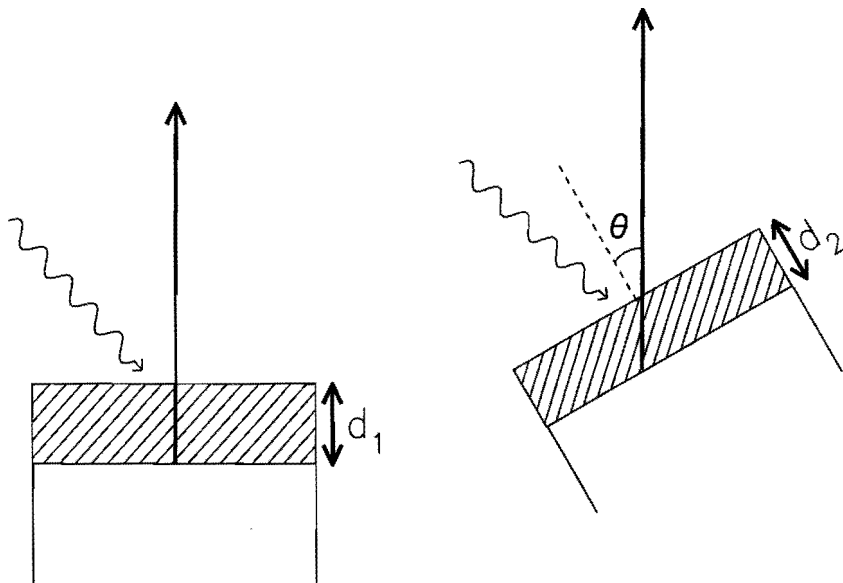


Figure 2.10

Principle of angle-dependent XPS. With increasing take-off angle θ , the effective probe depth (d) becomes smaller ($d_2 < d_1$).

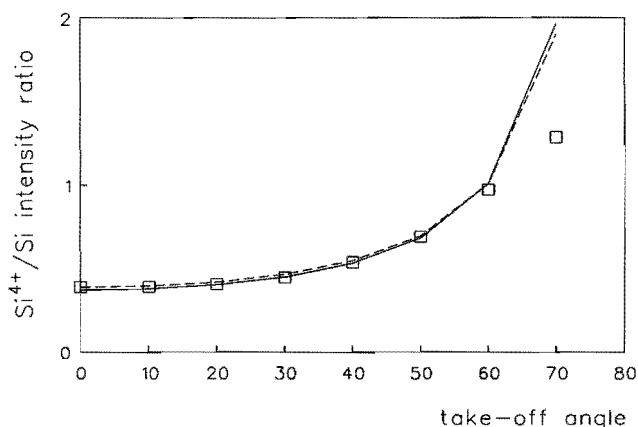
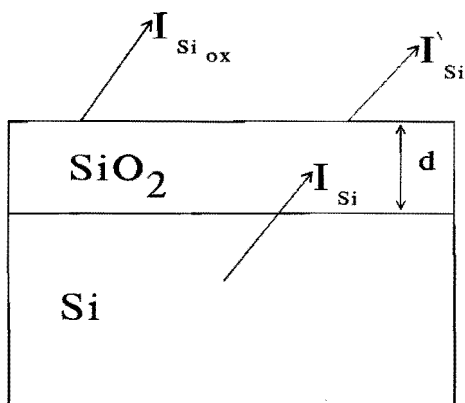


Figure 2.11

Si^{4+}/Si XPS intensity ratios (\square) as function of the take-off angle of a $Si(100)$ crystal with a native oxide layer together with theoretical fitted profiles.

The thickness of this oxide layer can be determined with angle-dependent XPS. The principle of this technique is shown in Figure 2.10. By varying the angle of detection with respect to the surface normal, θ , the so called take-off angle, the mean escape depth of the detected electrons is changed. Thus with increasing take-off angle we detect progressively more electrons originating from the surface region.

Figure 2.11 shows the Si^{4+}/Si intensity ratios from angle-dependent XPS spectra of a $Si(100)$ single crystal with a native oxide layer. Assuming that the SiO_2 forms a homogeneously thick layer we can calculate the expected photoelectron intensities in the following way:



$$\begin{aligned}
I_{Si} &= T(E_{Si}) \cdot n_{Si} \cdot \sigma_{Si} \cdot A \cdot (\cos\theta)^{-1} \cdot \int_0^{\infty} e^{-x/\lambda_{Si}(E_{Si}) \cdot \cos\theta} dx \\
&= -T(E_{Si}) \cdot n_{Si} \cdot \sigma_{Si} \cdot A \cdot \lambda_{Si}(E_{Si}) \cdot \left[e^{-x/\lambda_{Si}(E_{Si}) \cdot \cos\theta} \right]_0^{\infty} \\
&= T(E_{Si}) \cdot n_{Si} \cdot \sigma_{Si} \cdot A \cdot \lambda_{Si}(E_{Si})
\end{aligned} \tag{2.1}$$

$$I_{Si}^{\cdot} = I_{Si} \cdot e^{-d/\lambda_{SiO_2}(E_{Si}) \cdot \cos\theta} \tag{2.2}$$

$$\begin{aligned}
I_{Si^{4+}} &= T(E_{Si^{4+}}) \cdot n_{Si^{4+}} \cdot \sigma_{Si^{4+}} \cdot A \cdot (\cos\theta)^{-1} \cdot \int_0^d e^{-x/\lambda_{SiO_2}(E_{Si^{4+}}) \cdot \cos\theta} dx \\
&= -T(E_{Si^{4+}}) \cdot n_{Si^{4+}} \cdot \sigma_{Si^{4+}} \cdot A \cdot \lambda_{SiO_2}(E_{Si^{4+}}) \cdot \left[e^{-x/\lambda_{SiO_2}(E_{Si^{4+}}) \cdot \cos\theta} \right]_0^d \\
&= T(E_{Si^{4+}}) \cdot n_{Si^{4+}} \cdot \sigma_{Si^{4+}} \cdot A \cdot \lambda_{SiO_2}(E_{Si^{4+}}) \cdot \left(1 - e^{-d/\lambda_{SiO_2}(E_{Si^{4+}}) \cdot \cos\theta} \right)
\end{aligned} \tag{2.3}$$

If we consider E_{Si} and E_{SiO_2} equal then:

$$\lambda_{SiO_2}(E_{Si}) = \lambda_{SiO_2}(E_{Si^{4+}}) \tag{2.4}$$

The Si^{4+}/Si intensity ratio as function of the take-off angle can now be calculated with the following relation:

$$\frac{I_{Si^{4+}}}{I_{Si}} = \frac{\sigma \cdot n_{Si^{4+}} \cdot \lambda_{SiO_2} \cdot \left(1 - e^{-d/\lambda_{SiO_2} \cdot \cos\theta} \right)}{\sigma \cdot n_{Si} \cdot \lambda_{Si} \cdot e^{-d/\lambda_{SiO_2} \cdot \cos\theta}} \tag{2.5}$$

in which:

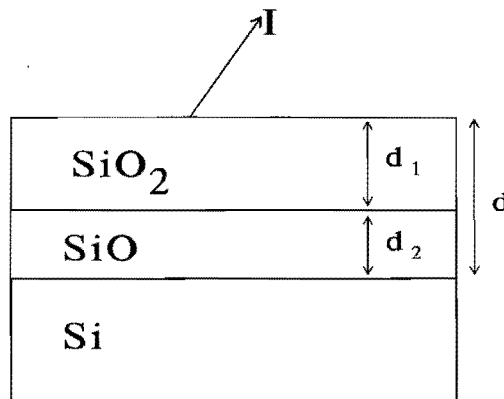
- $I_{Si^{4+}}$ and I_{Si} are the XPS intensities of the Si 2p peaks for the SiO_2 and Si components
- $n_{Si^{4+}}$ (0.036 mol/cm^3) and n_{Si} (0.083 mol/cm^3) are the atomic densities in SiO_2 and Si respectively
- σ (0.817) is the cross section for $AlK\alpha$ radiation according to Scofield [25], equal for Si^{4+} and Si
- A is the analyzer sample area

- E_{Si} (1387.2 eV) and $E_{\text{Si}^{4+}}$ (1383.2 eV) are the kinetic energies of the photoelectrons originating from Si and Si^{4+}
- T is the analyser transmission function [26] at the prevalent kinetic energy, considered equal for Si and Si^{4+}
- θ is the take-off angle with respect to the surface normal
- d is the thickness of the SiO_2 overlayer
- λ_{Si} (31.6Å) and λ_{SiO_2} (28.3Å) are the inelastic mean free paths, in Si and SiO_2 at the prevalent kinetic energy according to Tanuma et al. [27,28]

According to the Committee E-42 on Surface Analysis of the American Society of Testing and Materials, the inelastic mean free path is defined as the average distance that an electron with given energy travels between successive inelastic collisions [29].

For a 19 Å thick SiO_2 layer we get the solid curve in Figure 2.11. The curve fits very well with the experimental values except for the higher take-off angles. This deviation at higher take-off angles might be explained, after Bashenko and Nesmeev [30], by the effect of elastic scattering of the photoelectrons in the solid.

Al-Bayati et al. [31] found with high depth resolution medium energy ion scattering that the native oxide on an Si(100) single crystal is about 20 Å thick, which is in good agreement with the 19 Å we find. Although we find no indication that there are other silicon oxidation states than Si^{4+} , Al-Bayati et al. [31] also found that the native oxide consist of a SiO_2 layer at the surface and a suboxide at the interface between the oxide and the silicon substrate, whereas thermally grown oxide layers consist mainly of SiO_2 . To show that the analysis as used by us remains valid, we also calculated angle-dependent XPS intensity ratios for the case that the oxide layer consists of an SiO_2 on top of an SiO layer. Considered that the inelastic mean free paths of the photoelectrons are the same in both materials, we get the following:



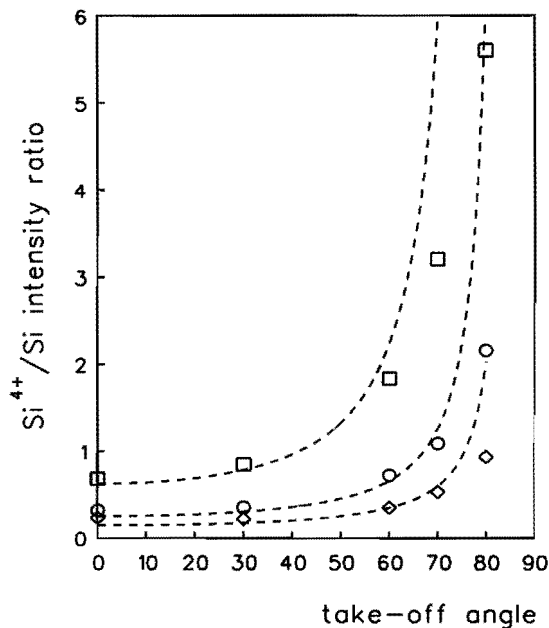


Figure 2.12

Angle-dependent XPS data of the $\text{SiO}_2/\text{Si}(100)$ model support for several oxidation temperatures together with theoretical fits (---). The oxide is formed by heating in air at 100 °C (\diamond); 350 °C (\circ) and 480 °C (\square).

$$I_{\text{Si}} = T(E_{\text{Si}}) \cdot n_{\text{Si}} \cdot \sigma_{\text{Si}} \cdot A \cdot \lambda_{\text{Si}}(E_{\text{Si}}) \cdot e^{-d / \lambda_{\text{SiO}_x}(E_{\text{Si}}) \cdot \cos\theta} \quad (2.6)$$

$$I_{\text{SiO}_2} = T(E_{\text{SiO}_2}) \cdot n_{\text{SiO}_2} \cdot \sigma_{\text{SiO}_x} \cdot A \cdot \lambda_{\text{SiO}_x}(E_{\text{SiO}_x}) \cdot \left(1 - e^{-d_1 / \lambda_{\text{SiO}_x}(E_{\text{SiO}_x}) \cdot \cos\theta}\right) \quad (2.7)$$

$$I_{\text{SiO}} = T(E_{\text{Si}_{\text{ox}}}) \cdot n_{\text{SiO}} \cdot \sigma_{\text{Si}_{\text{ox}}} \cdot A \cdot \lambda_{\text{SiO}_x}(E_{\text{Si}_{\text{ox}}}) \cdot \left(1 - e^{-d_2 / \lambda_{\text{SiO}_x}(E_{\text{Si}_{\text{ox}}}) \cdot \cos\theta}\right) \cdot e^{-d_1 / \lambda_{\text{SiO}_x}(E_{\text{Si}_{\text{ox}}}) \cdot \cos\theta} \quad (2.8)$$

The atomic density n_{SiO} is 0.048 mol/cm³. The $\text{Si}_{\text{ox}}/\text{Si}$ intensity ratio as function of the take-off angle can be calculated by:

$$\frac{I_{\text{SiO}_2} + I_{\text{SiO}}}{I_{\text{Si}}} \quad (2.9)$$

Now we find an SiO_2 layer of 10 Å on an SiO layer of 8 Å for the dashed curve in Figure 2.11. For both models we find approximately the same thickness of the oxide layer,

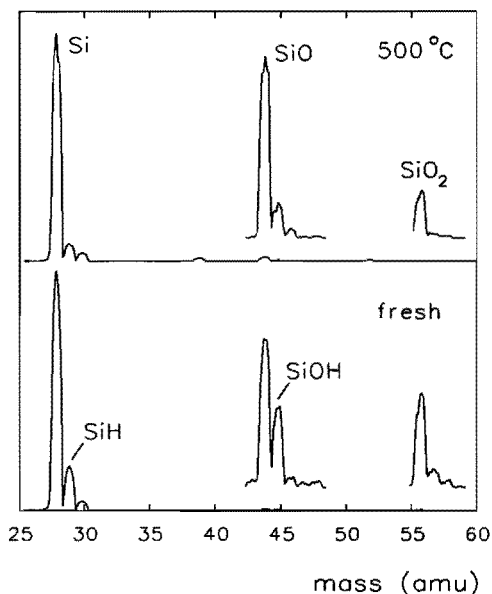


Figure 2.13

Static SIMS spectra of the $\text{SiO}_2/\text{Si}(100)$ model support before (lower part) and after heating at 500 °C in air (upper part).

implying that our method remains valid irrespective of the nature of the oxide layer.

Figure 2.12 shows the Si^{4+}/Si intensity ratios from angle-dependent XPS spectra of the $\text{SiO}_2/\text{Si}(100)$ model support for several oxidation temperatures. Each oxidation step took 12 hours and was done in air. The initial Si^{4+}/Si ratio increases with higher oxidation temperature and at the same time the angle-dependence becomes more pronounced. This means that the silicon oxide layer grows with increasing oxidation temperature. The dashed lines in Figure 2.12 are the fitted theoretical curves of the Si^{4+}/Si ratio as function of the take-off angle, assuming that the SiO_2 forms a homogeneously thick layer. These profiles are calculated using equation (2.5). When we use $d=27 \text{ \AA}$ we get the uppermost curve, which agrees well with the measured values for the oxide layer formed at 500 °C. Thus the $\text{SiO}_2/\text{Si}(100)$ model support formed during 12 hours oxidation at 500 °C in air has an SiO_2 layer of about 3 nm thick.

The surface of a technical silica support contains hydroxyl groups, that desorb upon heating to temperatures above approximately 450 °C. Static SIMS spectra confirm that the surface of the $\text{SiO}_2/\text{Si}(100)$ model support contains SiOH groups, as indicated by the peak at 45 amu in the lower part of Figure 2.13. In the upper part of Figure 2.13 the static SIMS spectrum of the same model support is plotted, but now after heating at 500 °C in air for about half an hour. Most of the OH groups have disappeared. This means that regarding hydroxyl groups, the SiO_2/Si model support behaves similarly as a porous silica support. This is in qualitative agreement with results from M. Niwano et al. [32], who showed with photon stimulated desorption that, on a thermally grown SiO_2 layer of 3 nm on an Si(100) substrate, Si-OH groups are present on the outermost layer of the SiO_2 film.

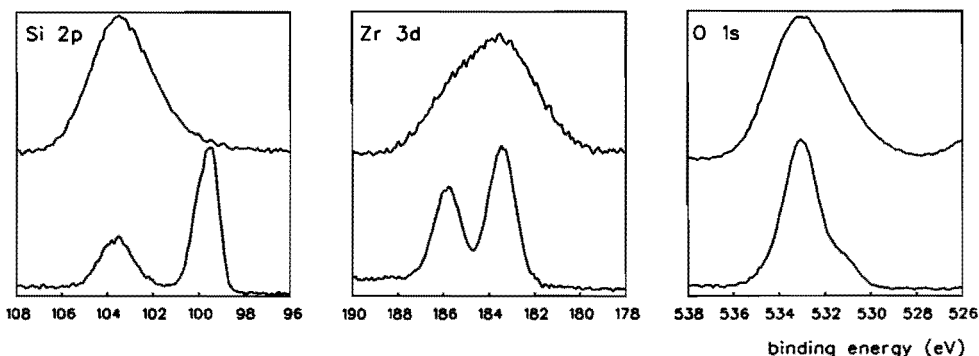


Figure 2.14

XPS spectra of the Si 2p, Zr 3d and O 1s peaks of a calcined ZrO_2/SiO_2 powder catalyst (top) and a calcined $ZrO_2/SiO_2/Si(100)$ model catalyst (bottom). The spectra of the powder catalyst have been corrected for charging.

2.3.3 $ZrO_2/SiO_2/Si(100)$ model catalysts

Figure 2.14 shows clearly the great advantage that a model catalyst offers with respect to spectral resolution. The XPS spectra of the model catalyst are much better resolved than those of the powder catalyst. Typical zirconium 3d and silicon 2p doublet and oxygen 2s singlet XPS peaks for the calcined powder and model catalysts, prepared via the zirconium ethoxide route, are shown in Figure 2.14. XPS parameters are given in Table 2.4. The peaks in the spectra of the powder catalyst are broad and exhibit a charge shift of 7 eV. The spectra of Figure 2.14 have been corrected for this shift by using the Si 2p peak of SiO_2 at 103.4 eV as an internal reference for the binding energy [18].

The spectra of the model catalyst, obtained using the same instrument settings, show a much better resolution. The zirconium 3d doublet is resolved into its 5/2 and 3/2 components quite readily. The line width of the $Zr\ 3d_{5/2}$ peak is 1.4 eV, as compared to 3.3 eV in the spectrum of the powder catalyst. The $Zr\ 3d_{5/2}$ binding energy in the spectrum of the model system of 183.3 eV is somewhat higher than the value found for the powder catalyst, but remains fully characteristic of Zr^{4+} .

The O 1s spectrum contains two contributions. The dominant peak at a binding energy of 532.9 eV is characteristic of O^{2-} in SiO_2 , the smaller peak at 531.0 eV is assigned to the ZrO_2 . Note that the spectrum of the powder catalyst does not allow for a distinction between two types of oxide.

The Si 2p spectrum of the model catalyst consists of two peaks, one at 103.4 eV due to SiO_2 and the other at 99.5 eV due to the silicon substrate. The latter peak is actually an unresolved $2p_{3/2} - 2p_{1/2}$ doublet, which is the reason that the Si 2p signal of the substrate is

Table 2.4*XPS parameters of the ZrO₂ catalysts.*

peak	B.E. (eV)	FWHM (eV)	assignment
<i>powder catalyst</i>			
Zr 3d _{5/2}	183.0 ^a	3.3	Zr ⁴⁺
Si 2p	103.4 ^a	3.3	Si ⁴⁺ of SiO ₂
O 1s	532.6 ^a	3.4	O ²⁻ of SiO ₂
<i>model catalyst</i>			
Zr 3d _{5/2}	183.3 ^b	1.4	Zr ⁴⁺
Si 2p	103.4 ^b	1.8	Si ⁴⁺ of SiO ₂
	99.5	1.1	Si ⁰ of substrate
O 1s	532.9 ^b	1.8	O ²⁻ of SiO ₂
	531.0 ^b	1.8	O ²⁻ of ZrO ₂

^a corrected for a charge shift of 7 eV^b corrected for a charge shift of 0.2 eV

slightly asymmetric. The intensity ratio of the Si⁴⁺ and Si⁰ peaks corresponds to an SiO₂ layer thickness of approximately 3 nm.

The Zr 3d_{5/2} binding energy does not vary outside the limits of accuracy for the differently prepared model catalysts. Whether the model catalyst is prepared by exchange from zirconium ethoxide or by impregnation from zirconium nitrate, the binding energy is 183.3 ± 0.2 eV. On the freshly prepared model catalyst from zirconium nitrate a small amount of nitrogen is detected. The binding energy of the N 1s peak is 408 eV, corresponding to nitrate species. The nitrate disappears at higher temperatures. The main difference between freshly prepared and calcined model catalysts is that the former contain a more intense C 1s signal (not shown), which disappears largely upon calcination.

Because charging has been circumvented, Auger electron spectroscopy and static SIMS may also be used to characterize the model catalysts. Auger spectroscopy is based on the Auger decay process of electrons. A core electron is emitted by bombarding a substance with high energy electrons (3-5 keV). The formed core hole is filled by an electron of a higher shell. The energy released by this process is used to emit another electron. The kinetic energy of this so called Auger electron is element specific. In an Auger spectrum the intensity of the detected electrons is plotted against their kinetic energy. In Figure 2.15 we show, as an example, the Auger survey spectra of the fresh and the oxidized model catalysts prepared by impregnation from the zirconium nitrate solution. The spectra in Figure 2.15 show clearly the Si LMM Auger transitions at 76 and 92 eV of SiO₂ and Si, respectively, the Zr MNN transitions at about 115 and 145 eV, the C KVV transition at 272 eV and the

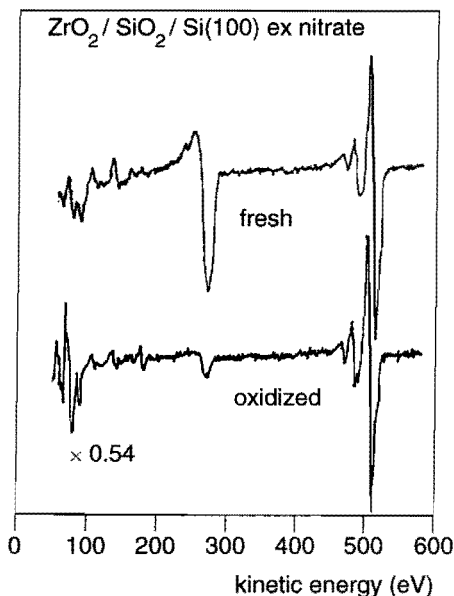


Figure 2.15

Electron beam excited Auger spectra of the ZrO_2 model catalyst prepared by impregnation from a nitrate solution.

O KVV transitions with the main peak at 503 eV.

The intense C KVV signal indicates that the freshly impregnated catalyst is severely contaminated by carbon. Note that this carbon overlayer distorts the relative intensities of Si, Zr and O because of the energy dependence of the electron mean free path. Most of the carbon is removed upon oxidation. However, the Zr intensity decreases with respect to both Si and O in spite of the removal of carbon. If we exclude vaporization, this decrease in intensity indicates that a significant loss of dispersion occurs upon oxidation. Finally, the spectrum of the oxidized catalyst shows that the Si LMM peak at 76 eV has grown in comparison to that of the fresh catalyst, indicating that the SiO_2 layer has become thicker.

Auger spectra of similar quality were obtained from the model catalyst prepared from zirconium ethoxide. In this case, the relative Zr intensities before and after oxidation were about equal, indicating that the ethoxide derived catalyst possesses a better thermal stability than the impregnated catalyst. This is in agreement with the results obtained with the porous silica supported zirconia catalysts as discussed above.

SIMS can be used under static conditions on model catalysts to characterize the surface, which is not possible on charging materials. When SIMS is performed under static conditions, the dose of primary ions is very low, so that less than 1% of the surface is damaged during a measurement. If we assume that molecular cluster ions result from direct emission [33], SIMS spectra give information about the coordination of the zirconium. Figure 2.16 shows the positive SIMS spectra of an ethoxide derived model catalyst after

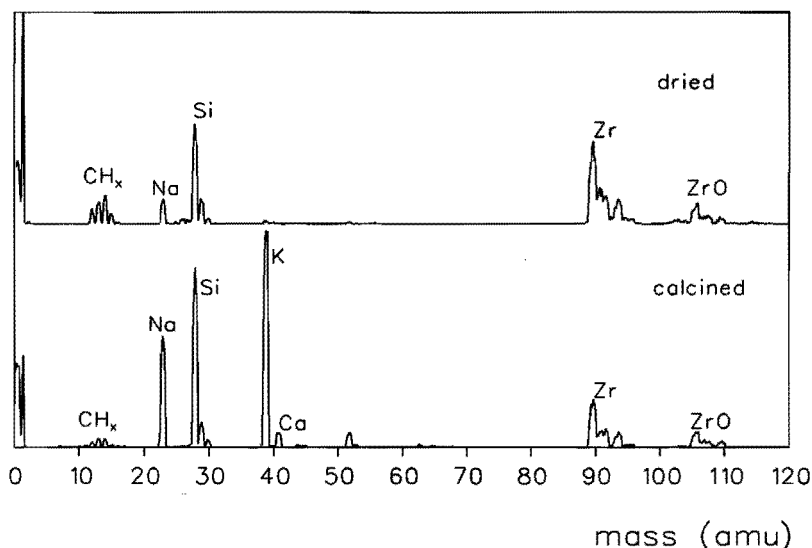


Figure 2.16

Positive SIMS spectra of a dried (top) and calcined (bottom) ethoxide derived $\text{ZrO}_2/\text{SiO}_2/\text{Si}(100)$ model catalyst.

drying at 40 °C (top) and after calcination at 480 °C in air (bottom). They contain peaks of H^+ , CH_x^+ , Na^+ , Si^+ , K^+ , SiC^+ , Ca^+ , Zr^+ , ZrC^+ , ZrO^+ , Hf^+ and HfO^+ (the latter two are not shown). The spectrum of the dried catalyst contains small contributions of ZrOH^+ ions. This is probably a fragment ion from zirconium ethoxide. The first thing to notice is that the relative amount of hydrocarbons on the surface decreases upon calcination, as confirmed by XPS and AES. This can be explained by two processes. Firstly, the removal of atmospheric hydrocarbon contamination by oxidation, and secondly by the decomposition of the zirconium ethoxide. The removal of ethoxide groups is also indicated by a decrease of the H^+ , SiH^+ , SiC^+ , ZrH^+ and ZrC^+ signals relative to the Si^+ signal. Spectra with a ten times higher ion beam current showed that calcination resulted in a decrease of the ZrCO^+ and an increase of the ZrO_2^+ signal. Although these spectra were taken under conditions that are not truly static, they show clearly the conversion from zirconium ethoxide into zirconium oxide. The spectra after calcination also show an increase in the SiO^+/Si^+ and ZrO^+/Zr^+ ratios, which means that the SiO_2 layer has become somewhat thicker, as was seen with AES, and that the zirconium phase has become oxidic. We note that, while this is not the case for the fresh catalyst, the ZrO^+/Zr^+ ratio of the calcined model catalyst resembles that of the powder reference compound as discussed in relation to Figure 2.7.

Since the model catalysts are flat samples, angle-dependent XPS and Auger depth profiling become feasible. Figure 2.17 shows the $\text{Zr } 3d / \text{Si}^{4+}$ XPS intensity ratio of an

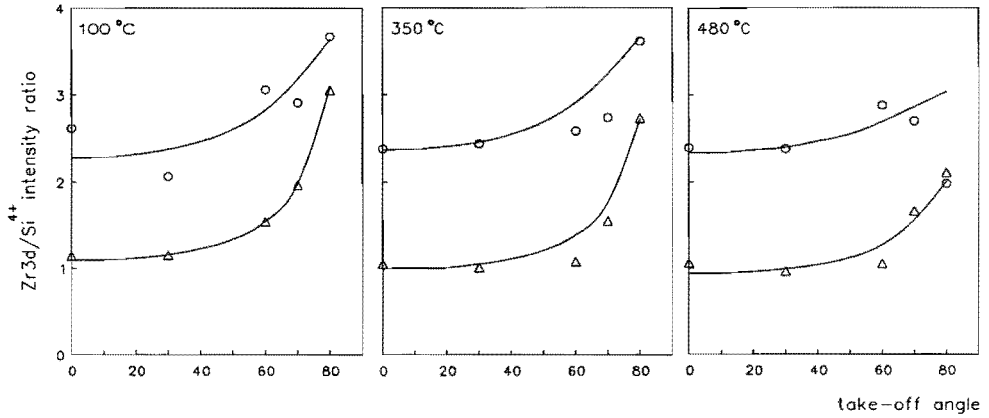


Figure 2.17

Zr 3d / Si 2p_{ox} XPS intensity ratios as a function of the take-off angle of the ZrO₂/SiO₂/Si(100) model catalyst derived from zirconium ethoxide (Δ) and zirconium nitrate (○) for calcination at 100 °C (a), 350 °C (b) and 480 °C (c). The solid lines are the theoretically fitted curves of the Zr 3d / Si 2p intensity ratios.

ethoxide and nitrate derived model catalyst after calcination at 100 °C, 350 °C and 480 °C. The ethoxide derived model catalyst shows a more pronounced angle-dependent behaviour of the Zr/Si ratio than the nitrate derived model catalyst. This indicates that the ethoxide derived ZrO₂ covers the SiO₂ surface to a greater extent than the nitrate derived ZrO₂. This is not caused by a higher loading of ZrO₂ of the ethoxide derived model catalyst, since the values of the Zr 3d / Si 2p ratio at perpendicular take-off angle of the nitrate derived model catalyst are higher, which implies that it is the catalyst prepared from nitrate that has the higher loading.

The following calculations substantiate qualitative conclusions on the ZrO₂ dispersion. The angle dependent Zr/Si⁴⁺ ratios have been fitted with a model in which we assume that ZrO₂ forms layers of thickness d , which covers a fraction ϑ of the support, and that photoemission from the edges of the layers can be ignored. Under these conditions we obtain the following relations:

$$I_{Zr3d} = T(E_{Zr}) \cdot \vartheta \cdot n_{ZrO_2} \cdot \sigma_{Zr} \cdot A \cdot \lambda_{ZrO_2}(E_{Zr}) \cdot \left(1 - e^{-d_{ZrO_2} / \lambda_{ZrO_2}(E_{Zr}) \cdot \cos\theta}\right) \quad (2.10)$$

$$\begin{aligned}
I_{\text{SiO}_2} = & T(E_{\text{SiO}_2}) \cdot \vartheta \cdot n_{\text{SiO}_2} \cdot \sigma_{\text{Si}} \cdot A \cdot \lambda_{\text{SiO}_2}(E_{\text{SiO}_2}) \cdot (e^{-d_{\text{ZrO}_2} / \lambda_{\text{ZrO}_2}(E_{\text{SiO}_2}) \cdot \cos\theta} \\
& - e^{(-\lambda_{\text{SiO}_2}(E_{\text{SiO}_2}) \cdot d_{\text{ZrO}_2} - \lambda_{\text{ZrO}_2}(E_{\text{SiO}_2}) \cdot d_{\text{SiO}_2}) / \lambda_{\text{ZrO}_2}(E_{\text{SiO}_2}) \cdot \lambda_{\text{SiO}_2}(E_{\text{SiO}_2}) \cdot \cos\theta}) + \\
& T(E_{\text{SiO}_2}) \cdot (1 - \vartheta) \cdot n_{\text{SiO}_2} \cdot \sigma_{\text{Si}} \cdot A \cdot \lambda_{\text{SiO}_2}(E_{\text{SiO}_2}) \cdot (1 - e^{-d_{\text{SiO}_2} / \lambda_{\text{SiO}_2}(E_{\text{SiO}_2}) \cdot \cos\theta})
\end{aligned} \tag{2.11}$$

in which:

- $I_{\text{Zr}3d}$ is the intensity of the Zr 3d peak
- I_{SiO_2} is the intensity of the Si 2p peak of the SiO₂ component
- n_{ZrO_2} (0.047 mol/cm³) and n_{SiO_2} (0.036 mol/cm³) are the atomic densities
- σ_{Zr} (7.04) and σ_{Si} (0.817) are the cross sections [25]
- θ is the take-off angle with respect to the surface normal
- d_{ZrO_2} and d_{SiO_2} (30Å) are the thicknesses of the ZrO₂ and SiO₂ layer respectively
- ϑ is the fraction of the SiO₂ surface covered by ZrO₂
- $\lambda_{\text{ZrO}_2}(E_{\text{Zr}})$ (23Å), $\lambda_{\text{ZrO}_2}(E_{\text{SiO}_2})$ (24Å) and $\lambda_{\text{SiO}_2}(E_{\text{SiO}_2})$ (28.3Å) are the inelastic mean free paths at the prevalent kinetic energy through ZrO₂ and SiO₂

As far as we are aware, values for inelastic mean free paths through ZrO₂ are not known. We have estimated that λ_{ZrO_2} is about 20% higher than for Zr, analogous as in SiO₂ [27,28]. The spectrometer transmission functions T for both kinetic energies diverge for only about 3% [26]. This difference is neglected in the calculations. The curves in Figure 2.17 are fits based on Equation (2.10) and (2.11); the corresponding parameters are given in Table 2.5. The data indicate that the ZrO₂ deposited on the support via the ethoxide preparation has significantly smaller dimensions and covers the SiO₂ to a greater extent than the ZrO₂ particles made via impregnation. It is also clear that the increase of the particle size upon calcination is relatively greater for the zirconium nitrate derived model catalysts. Hence, these results also lead to the conclusion that the preparation by a surface reaction between zirconium ethoxide and the hydroxyl groups on the silica support yields a better dispersed and more thermostable catalyst than preparation by impregnation from zirconium nitrate.

Since all elements of interest were readily detected by AES within a collection time of a few seconds, Auger depth profiling could be used to obtain concentrations as a function of depth. Now some specific AES signals are monitored, while layer by layer is removed from the surface by an ion beam, that is rastered over the surface. To get a better insight into Auger sputter depth profiles, Figure 2.18 shows two schematic profiles corresponding to two limiting cases. The left profile will be obtained when the SiO₂ layer is entirely covered by the ZrO₂ layer, the right when the SiO₂ layer is only partially covered by large ZrO₂ particles. In the first case the zirconium signal will start to decrease together with the oxygen signal. When the ZrO₂ layer is removed the O signal is still decreasing, because the O

Table 2.5

Effective thickness, support coverage and surface concentration of Zr as follow from the fits of the angle dependent Zr/Si XPS intensity ratios (Figure 2.17).

calcination temperature (°C)	ex ethoxide			ex nitrate		
	d(Å)	ϑ	$N_{Zr}(\text{at}/\text{cm}^2)$	d(Å)	ϑ	$N_{Zr}(\text{at}/\text{cm}^2)$
100	7.8	0.33	7.3×10^{14}	21	0.29	1.7×10^{15}
350	7.8	0.30	6.6×10^{14}	22	0.29	1.8×10^{15}
480	10	0.23	6.5×10^{14}	27	0.25	1.9×10^{15}

originates from both the ZrO_2 and SiO_2 layer. In other words, the half life time of the Zr signal is significantly lower than of the O signal. The silicon signal will increase to a maximum when all the oxide is removed. In the second case the Zr and O signal will again drop simultaneously. However, at the time all the ZrO_2 is removed, most of the SiO_2 will be removed as well, except for that amount that was covered by the ZrO_2 particles. So now the half life time of the Zr and O signal will be about equal.

In Figure 2.19 the depth profiles are shown for the fresh and oxidized nitrate and ethoxide derived model catalysts (different but similarly prepared samples as used for the XPS). Although all instrument settings were the same for each experiment, we can not guarantee that the sputter conditions were entirely identical, due to a small irreproducibility in the positioning of the sample. Hence, conclusions should not be based on absolute sputter times, but on changes in Auger intensities of the four elements with respect to each other. Since the intensities of each element are reported relative to the intensity of the clean silicon substrate (I_{Si}^0), these intensities may be compared between the four experiments.

The relative time dependence of the zirconium and oxygen signals from the ethoxide derived samples is markedly different from that of the nitrate derived samples. The zirconium intensity has a much shorter half life than the oxygen intensity, for both the fresh and the oxidized ethoxide samples. This behaviour is indicative of a layered structure in which the zirconium phase is on top of the silica layer. On the other hand, the normalized zirconium signal follows the oxygen signal almost identically for both the nitrate derived model catalysts. This and the steeper increase in the silicon intensity during sputtering indicate that the zirconium phase consists of relatively large particles which leave a large portion of the SiO_2 substrate uncovered.

As has already been discussed in connection with Figure 2.15, the freshly prepared catalysts are covered by a significant amount of carbon, which is removed by oxidation. However, the nature of the carbon layers on the two differently prepared fresh catalysts appears to be different. This can be seen in Figure 2.20, showing the initial sputter profiles of both the fresh model catalysts. In the nitrate derived zirconia catalyst the carbon is

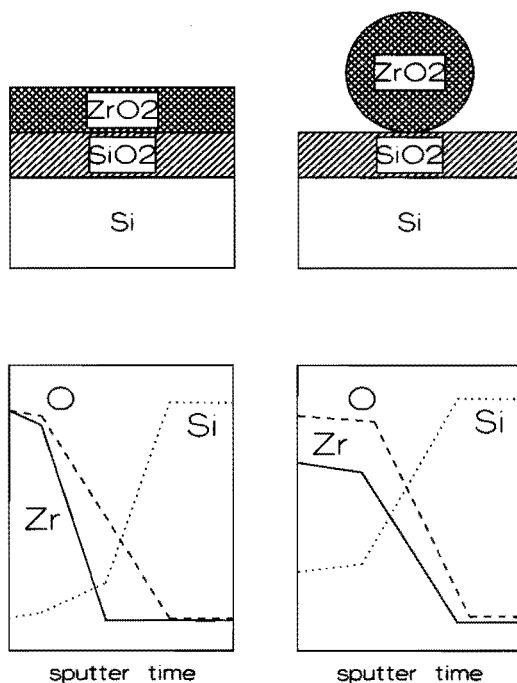


Figure 2.18

Schematic Auger sputter depth profiles of a layer of ZrO_2 covering the entire model support (left) and of large particles, partially covering the support (right).

removed relatively fast by sputtering, and the Auger intensities of Zr and O go up significantly, and do not decrease until about 75% of the carbon is removed. This suggests that the carbon is present as a layer which covers the entire model catalyst. On the other hand, the carbonaceous layer on the fresh ethoxide derived catalyst appears to be thicker, and mixed with zirconium and oxygen to a much greater extent, as suggested by the fact that the Zr and O signals increase only briefly initially and then decrease simultaneously with the C signal. Note, however, that the carbon is almost entirely removed when the Zr signal is still at 50% of its maximum intensity. This suggests that no ethoxide ligands are present at the level of the Zr-O-Si interface. From SIMS spectra (see above) we concluded that the Zr atoms have ethoxide ligands as neighbours. IR experiments on the powder catalysts [23] showed that ethanol also adsorbed on the silica surface. In Figure 2.21 we show a model of the Zr phase on the silica which explains the different nature of the carbon layers. Both the surfaces, of the ethoxide and nitrate derived catalyst are covered by a hydrocarbon contamination layer that originates from the air and the solvents. The layer of carbon of the

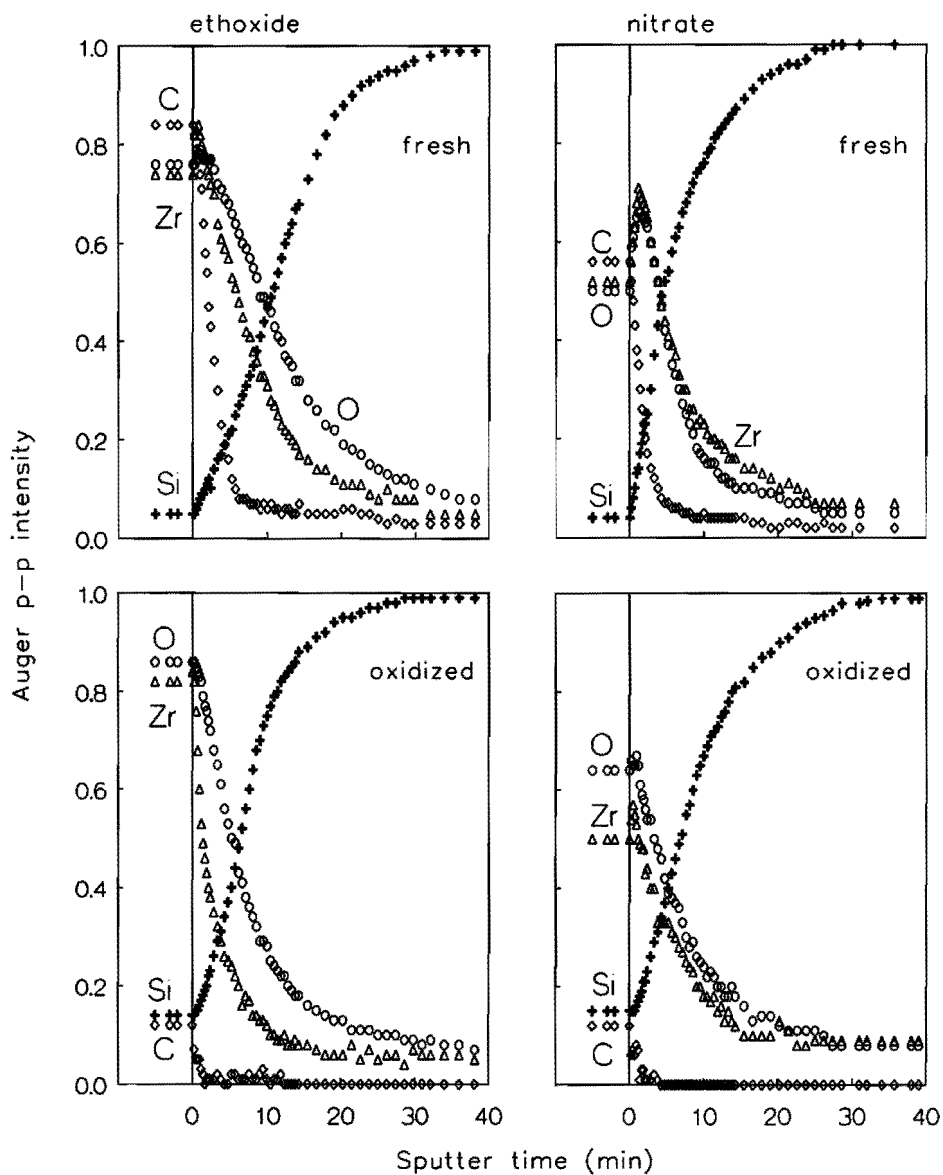


Figure 2.19

Auger sputter depth profiles of freshly prepared (above) and oxidized (below) zirconium oxide model catalysts prepared from zirconium ethoxide (left) and zirconium nitrate (right). The following magnification factors were used: Si (+) $\times 1$; O (o) $\times 2$; C (◇) $\times 4$; Zr (Δ) (above, left) $\times 12$; Zr (below, left) $\times 24$; Zr (right) $\times 20$.

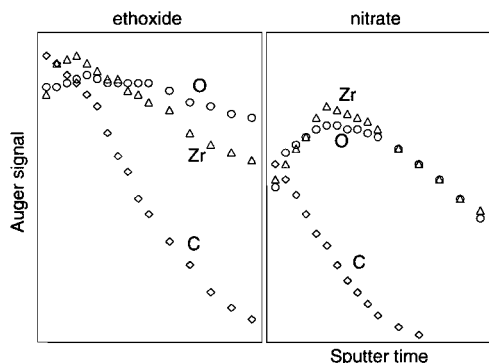


Figure 2.20

The initial regions of the Auger sputter depth profiles of the fresh ethoxide (left) and nitrate (right) derived model catalysts, showing the different nature of the carbon layers.

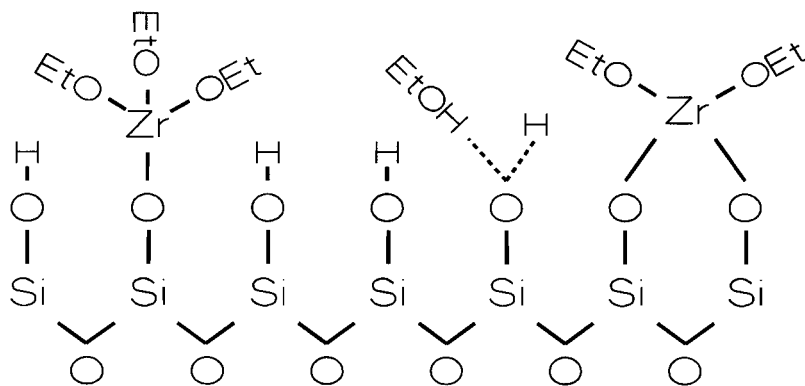


Figure 2.21

Model of the zirconium phase formed by the reaction of zirconium ethoxide with the silica surface.

ethoxide model catalyst is thicker because of the ethoxide ligands and ethanol in the plane of the zirconium phase. This also explains why the carbon is mixed with the Zr and O to a higher extent.

The carbon concentration of the oxidized catalysts is much smaller, and the carbon is removed rapidly upon sputtering. The sputter profile of the oxidized catalyst prepared from zirconium ethoxide is characteristic of a layered system in which the thickness of the zirconia is probably smaller than that of the underlying silicon oxide layer. The depth profile of the oxidized zirconia catalyst prepared by impregnation, on the other hand, shows no features characteristic of layered structures. The simultaneous removal of Zr and O at a rate that compared to the increase in the Si signal is significantly slower than for the ethoxide derived

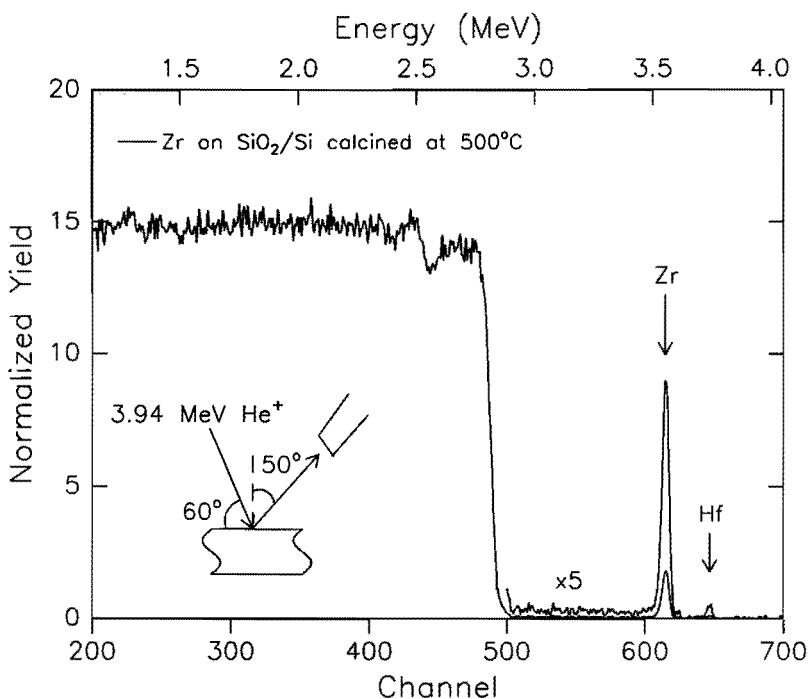


Figure 2.22

RBS spectrum of a $\text{ZrO}_2/\text{SiO}_2/\text{Si}(100)$ model catalyst prepared by impregnation from an aqueous solution of zirconium nitrate, measured with an incident beam of 3.94 MeV He^+ ions.

catalyst, is consistent with the presence of poorly dispersed ZrO_2 particles which leave a considerable fraction of the support uncovered.

Preparing supported model catalysts by wet chemical methods has the disadvantage that the amount of deposited zirconia, whether from nitrate or from ethoxide, is not known. Although Zr concentrations can be estimated indirectly from angle-dependent XPS, as we have shown above, RBS offers a more direct way to determine the Zr concentration. RBS is based on the scattering of high energetic (0.5-5 MeV) ions of low mass, e.g. He. These ions lose a certain amount of energy when they collide with the nuclei of the atoms in the probed substance. Ions that scatter from heavy atoms lose less energy than ions that scatter from light atoms. In an RBS spectrum the intensity of the detected backscattered ions is plotted against their kinetic energy. The energy of the backscattered ions depends on the masses of the atoms the ions scattered with. Actually, this energy spectrum can be regarded as a mass spectrum of the probed material. Because of the high energy of the incident ions, RBS is not surface sensitive. The advantage of RBS is that the composition of the sample

can be determined rather accurately. Figure 2.22 shows the RBS spectrum of a ZrO₂/SiO₂/Si(100) catalyst prepared by impregnation from zirconium nitrate in water (different sample as used for XPS or for AES). The spectrum shows sharp peaks at 3.554 MeV corresponding to Zr and at 3.738 MeV corresponding to Hf (a known impurity of Zr [20]) and a broad continuum below 2.8 MeV due to the Si substrate. The structure between 2.5 and 2.8 MeV is attributed to a nuclear resonance [34].

The amount of Zr on the sample has been calculated from Figure 2.22 from the ratio of the integrated Zr peak and the Si signal height below channel 350. This region corresponds to incident He ions which have slowed down to an energy below 3.7 MeV just before scattering, which is the empirical limit for Rutherford scattering in Si [34]. In this way the Zr concentration can be calculated from the Zr and Si cross sections and the stopping power of Si [35] without the need to measure the ion dose with a Faraday cup. The concentration of Zr thus determined is $5.7 \pm 0.2 \times 10^{15}$ atoms per cm², while Hf corresponds to $7 \pm 1 \times 10^{13}$ atoms/cm². The Zr areal density is appreciably higher than the 1.8×10^{15} Zr/cm² derived from XPS. However, direct comparison is not appropriate as RBS and XPS were done on different although similarly prepared samples. We included this section to illustrate the potential of RBS as a technique to determine accurate surface concentrations on model catalysts.

2.4 Concluding remarks

In this chapter we have explored the possibilities of using a thin layer of silicon dioxide on a silicon substrate as a model support for preparing model catalysts, and we have compared surface analysis of the ZrO₂ model catalysts with surface analysis of ZrO₂ powder catalysts.

Preparation of ZrO₂/SiO₂ catalysts by reaction of zirconium ethoxide dissolved in ethanol with the hydroxyl groups of the silica support yields a well dispersed catalyst with a satisfactory thermal stability. Preparation by incipient wetness impregnation from an aqueous zirconium nitrate solution results in a much less dispersed and less thermostable catalyst.

A flat, conducting model support consisting of a few nanometres of SiO₂ on an Si (100) substrate, offers attractive possibilities for the application of XPS, AES and other charge-sensitive surface spectroscopies, to study aspects of the surface chemistry involved in catalyst preparation. First, electrical charging is avoided, which means that not only the spectral resolution of XPS improves, but also that Auger spectroscopy becomes feasible. Second, the flat geometry of the support makes the application of sputter depth profiling and angle-dependent XPS and AES studies meaningful. The results demonstrate that conducting model catalysts can successfully be prepared by the same wet chemical procedures as used in the preparation of powder catalysts. It has become clear that the same features in the catalyst preparation can be studied on the model catalysts as on the powder catalysts. This shows that

model catalysts are adequate systems to study catalyst preparation and they offer the possibility to study surface chemical aspects of catalyst preparation by means of surface spectroscopies that are either not applicable or not applicable to their full potential on powder catalysts.

References

- [1] L.H. Dubois, P.K. Hansma and G.A. Somorjai, *Appl. Surf. Sci.* **6**, 173 (1980).
- [2] P.A. Spevack and S. McIntyre, *Appl. Catal.* **64**, 191 (1990).
- [3] D.N. Belton, Y.-M. Sun and J.M. White, *J. Phys. Chem.* **88**, 5172 (1984).
- [4] B.G. Frederick, G. Apai and T.N. Rhodin, *J. Am. Chem. Soc.* **109**, 4797 (1987).
- [5] D.N. Belton and S.J. Schmieg, *Appl. Surf. Sci.* **32**, 173 (1988).
- [6] A. Jiménez-González and D. Schmeisser, *J. Catal.* **130**, 332 (1991).
- [7] J. Nickl, R. Schlögl, A. Baiker, H. Knözinger and G. Ertl, *Catal. Lett.* **3**, 379 (1989).
- [8] N.B. Jackson and J.G. Ekerdt, *J. Catal.* **126**, 31 (1990).
- [9] K. Tanabe, *Mater. Chem. Phys.* **13**, 347 (1985).
- [10] T. Iizuka, M. Kojima and K. Tanabe, *J.C.S. Chem. Communication*, 638 (1983).
- [11] R. Burch, Zirconium in catalysis-its uses and potential, Reading University, England.
- [12] T. Iizuka, Y. Tamaka and K. Tanabe, *J. Catal.* **76**, 1 (1982).
- [13] P.D.L. Mercera, J.G. van Ommen, E.B.M. van Doesburg, A.J. Burggraaf and J.R.H. Ross, *Appl. Catal.* **57**, 127 (1990).
- [14] T. Yamaguchi, T. Morita, T.M. Salama and K. Tanabe, *Catal. Lett.* **4**, 1 (1990).
- [15] H.L. Hagedoorn, J.W. Broer and F. Schutte, *Nucl. Instr. and Meth.* **86**, 253 (1970).
- [16] H.J. Borg, L.C.A. van den Oetelaar, L.J. van IJzendoorn and J.W. Niemantsverdriet, *J. Vac. Sci. Technol. A* **10**, 2737 (1992).
- [17] A.M. de Jong, L.M. Eshelman, L.J. van IJzendoorn and J.W. Niemantsverdriet, *Surf. Int. Anal.* **18**, 412 (1992).
- [18] C.D. Wagner, W.M. Riggs, L.E. Davis, J.F. Moulder and G.E. Muilenberg, *Handbook of XPS*, Perkin Elmer Corporation, Eden Prairie MN, USA, 1978.
- [19] H.P.C.E. Kuipers, H.C.E. van Leuven and W.M. Visser, *Surf. Int. Anal.* **8**, 235 (1986).
- [20] R.C. Weast, Ed.; *Handbook of chemistry and physics*, 52nd edition, The chemical rubber co., Ohio, 1971.
- [21] K. Hirokawa and Y. Danzaki, *Surf. Int. Anal.* **4**, 63 (1982).
- [22] B.E. Yoldas, *J. Mater. Sci.* **21**, 1080 (1986).
- [23] A.C.Q.M. Meijers, A.M. de Jong, L.M.P. van Gruijthuijsen and J.W. Niemantsverdriet, *Appl. Catal.* **70**, 53 (1991).
- [24] T.E. Madey, C.D. Wagner and A. Joshi, *J. Elec. Spectr.* **10**, 359 (1977).
- [25] J.H. Scofield, *J. Elec. Spectr. Rel. Fenom.* **8**, 129 (1976).
- [26] M.P. Seah and G.C. Smith, *Surf. Int. Anal.* **15**, 751 (1990).
- [27] S. Tanuma, C.J. Powell and D.R. Penn, *Surf. Int. Anal.* **17**, 911 (1991).
- [28] S. Tanuma, C.J. Powell and D.R. Penn, *Surf. Int. Anal.* **17**, 927 (1991).
- [29] C.J. Powell, *J. Elec. Spectr. Rel. Fenom.* **47**, 197 (1988).
- [30] O.A. Bashenko and A.E. Nesmeev, *J. Elec. Spectr. Rel. Fenom.* **57**, 33 (1991).
- [31] A.H. Al-Bayati, K.G. Orrman-Rossiter, J.A. van den Berg and D.G. Armour, *Surf. Sci.* **241**, 91 (1991).
- [32] M. Niwano, Y. Takakuwa, H. Katakura and N. Miyamoto, *J. Vac. Sci. Technol. A* **9**, 212 (1991).
- [33] H. Oechsner in *Secondary Ion Mass Spectrometry SIMS III, Proc. 3rd Int. Conf.*; A. Benninghoven, A.J. Giber, J. Laszlo, M. Riedel and H.W. Werner, Eds.; Springer, Berlin, p. 106, 1982.
- [34] J.A. Leavitt and L.C. McIntyre Jr., *Nucl. Instr. and Meth. B* **56/57**, 734 (1991).
- [35] J.F. Ziegler, J.B. Biersack and U. Littmark, *The Stopping and Range of Ions in Solids*, Vol I, Pergamon Press, New York, 1985.

3 Sulfidation mechanism of molybdenum catalysts supported on an SiO₂/Si(100) model support, studied by surface spectroscopy*

Abstract

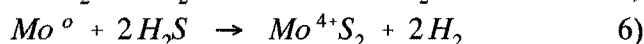
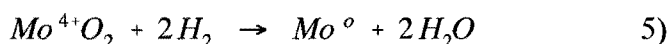
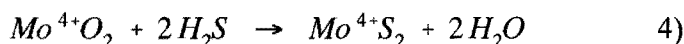
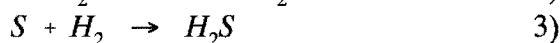
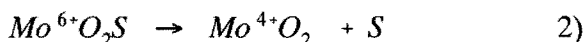
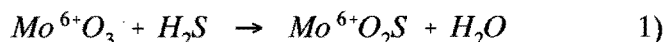
The sulfidation of disk shaped MoO₃ particles with a thickness of 5-10 nm supported on a 5 nm thick layer of SiO₂ on Si(100) in a mixture of 10% H₂S in H₂ at atmospheric pressure has been studied as a function of temperature. XPS and SIMS indicate the formation of Mo⁴⁺OS_x at the surface and Mo(IV) oxides (probably H_{1,6}MoO₃, or MoO₂) in the interior of the particles at temperatures between 20 and 100 °C, whereas MoS₂ forms at temperatures of 125 °C and higher. Sulfur is present in two forms, as S²⁻, and in a second form which is most probably S₂²⁻ or SH, but not elemental sulfur. The additional sulfur species disappear at temperatures between 150 and 200 °C. Rutherford backscattering analysis indicates S:Mo atomic ratios of 1 to 1.5 at sulfidation temperatures below 100 °C and of 2 to 2.5 above 100 °C. It is concluded that the sulfidation of MoO₃ to MoS₂ proceeds through a Mo(IV) oxysulfide, formed initially at the outside of the particles, and Mo(IV) oxide in the interior of the particles. Sulfidic species are believed to facilitate the reduction of MoO₃ to Mo(IV) species at low temperatures.

3.1 Introduction

Sulfidation of molybdenum oxide to MoS₂ is an essential step in the activation of hydrotreating catalysts, used for the removal of sulfur and nitrogen from heavy oil fractions [1]. Although a wealth of spectroscopic information is available on the working HDS catalysts [1,2], much less is known about the sulfidation mechanism of the catalysts. Moulijn and coworkers [3-6] extensively studied the sulfidation mechanism of alumina, silica and carbon supported molybdenum and cobalt-molybdenum catalysts with temperature programmed sulfidation (TPS). This technique measures the consumption and evolution of H₂S, H₂ and H₂O by a catalyst as a function of temperature and gives valuable information on the sulfur content and the extent of reduction. Although H₂S is consumed over almost the entire temperature range up to 700 °C where sulfidation is complete, H₂S actually evolves

* The content of this chapter has been published: A.M. de Jong, H.J. Borg, L.J. van IJzendoorn, V.G.F.M. Soudant, V.H.J. de Beer, J.A.R. van Veen and J.W. Niemantsverdriet, *J. Phys. Chem.* **97**, 6477 (1993).

in a sharp peak around 250 °C, accompanied with significant hydrogen consumption. The authors attribute this to the hydrogenation of excessive sulfur, assumed to be present in elemental form. Arnoldy et al. [4] propose the following mechanism for the sulfidation of unsupported MoO₃ under temperature programmed conditions:



Noteworthy features of the scheme are the appearance of an Mo(VI)O₂S oxysulfide which decomposes to MoO₂ and elemental sulfur, as well as two alternative routes from MoO₂ to MoS₂, one proceeding through metallic molybdenum.

In this chapter we follow the sulfidation of silica supported molybdenum oxide as a function of temperature by means of atomic force microscopy (AFM), Rutherford backscattering spectrometry (RBS), X-ray photoelectron spectroscopy (XPS) and secondary ion mass spectrometry (SIMS). We also studied the reduction of silica supported molybdenum oxide in hydrogen with XPS as a reference case, for understanding the reduction processes that accompany the sulfidation.

Oxide supported catalysts charge up during XPS and SIMS analysis, leading to peak broadening and consequently loss of resolution in XPS and to diminished intensities in SIMS. These problems can be avoided by using a conducting model support, consisting of a thin oxide layer on a conducting substrate [7-12]. Here we use a 5 nm thick layer of SiO₂ on a Si single crystal, onto which Mo is applied by wet chemical impregnation. Such model catalysts have the additional advantage that the direction perpendicular to the surface is defined, and that depth selective information can be obtained [10-12].

It is important to realize that temperature programmed studies concern reactions in which either of the gases H₂S, H₂ and H₂O are consumed or produced under non equilibrium conditions. The spectroscopic results presented here, on the other hand, reveal the stable Mo and S phases in the catalyst after a certain isothermal sulfidation treatment, i.e. under equilibrium conditions (at least at higher temperatures). It should be kept in mind that both approaches highlight different aspects of the sulfidation mechanism.

3.2 Experimental

3.2.1 Model catalysts

A silicon wafer with (100) surface orientation and a diameter of 75 mm was oxidized in air at 500 °C for 24 hours. Angle-dependent XPS experiments done as explained in Chapter 2 [12,13] indicated that the SiO₂ layer is 5.1 nm thick. Molybdenum was applied from a solution of MoO₂Cl₂ (Alfa products, Johnson Matthey GmbH) in ethanol (concentration 2 g/l). Ethanol was used as the solvent because it wets the silicon oxide much better than water. In order to obtain a good macroscopic spreading, the wafer was spincoated at a speed of 2800 rpm according to a procedure described by Kuipers and coworkers [14]. The 75 mm wafer was cut into pieces of about 1 cm².

Reduction and sulfidation experiments were done in a quartz tube reactor. Sulfidation was done at 1 bar with a mixture of 10% H₂S in H₂ at a flow rate of 50 ml/min. The catalyst was heated at a rate of 5 °C/min to the desired temperature, and kept there for 3 hours. After sulfidation, the catalyst was cooled under helium to room temperature. Next the reactor was closed and introduced into a nitrogen-filled glove box, where the sample was transferred to a vessel for transport under nitrogen to the XPS and SIMS spectrometers. Each sulfidation experiment was done with a fresh piece of model catalyst from the same wafer. It was checked that sulfidation of the bare SiO₂/Si wafer does not occur. Reduction was done under a 1.5 bar H₂ flow for 30 minutes at the desired temperature. After reduction the reactor was transported under hydrogen to the glove box. All the reduction experiments were carried out on the same piece of model catalyst.

3.2.2 Techniques

Atomic force images were taken with a Topometrix TMX 2000 atomic force microscope, operating in constant force-contact mode, using a 1 μm piezo electric scanner.

RBS spectra were measured with an incident beam of 3.94 MeV or 2 MeV He⁺ at the AVF-cyclotron at Eindhoven University of Technology [15]. Details concerning the He beam optics and detectors have been published elsewhere [11,12]. We adopted a scattering geometry with the incoming beam directed along the surface normal and a scattering angle of 170°. We assume that the cross sections are accurate within 5%. The resulting overall energy resolution was measured to be 18 keV.

XPS spectra were obtained with a VG Escalab 200 spectrometer equipped with a standard and a monochromatic Al K_α source and a hemispherical analyzer connected to a five channel detector. The reduced samples were measured with the monochromatic X-ray source at 10 eV pass energy, the sulfided samples with the standard X-ray source at 20 eV pass

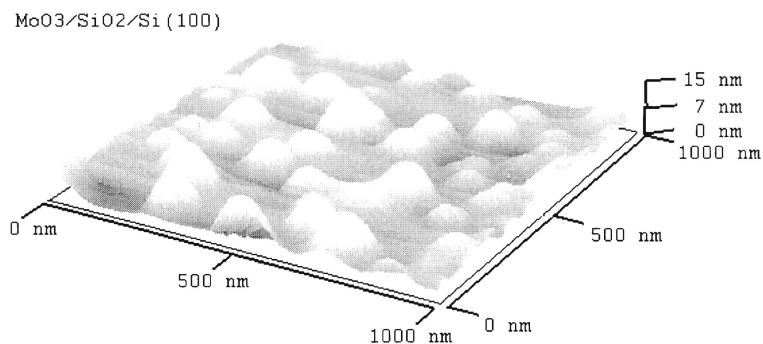


Figure 3.1

AFM image of a MoO₃/SiO₂/Si(100) model catalyst prepared by spin coating an SiO₂/Si(100) model support with a solution of MoO₂Cl₂ in ethanol at 2800 rpm.

energy. Charging was corrected for by using the C1s peak at 284.6 eV as a reference. The spectra have been fitted with the VGS program fit routine. We applied a Shirley background subtraction and used Gauss-Lorentz curves for the fits. The Gauss-Lorentz ratios are between 1 and 30%.

SIMS spectra were measured with a Leybold SSM 200 quadrupole mass spectrometer, using a 5 keV Ar⁺ primary ion beam with a current density of 0.5 μA/cm²s. The total time for recording a positive and a negative spectrum was approximately 500 s, estimated to result in the removal of about one monolayer. Charge compensation was not applied.

3.3 Results

3.3.1 Fresh model catalyst

With AFM three-dimensional images of a surface can be depicted. A very sharp tip is scanned over the surface and the repulsive force interaction between the surface and the tip is detected. If this interaction is kept constant, the displacement of the tip represents the topography of the surface. Figure 3.1 shows an AFM image of a freshly prepared model

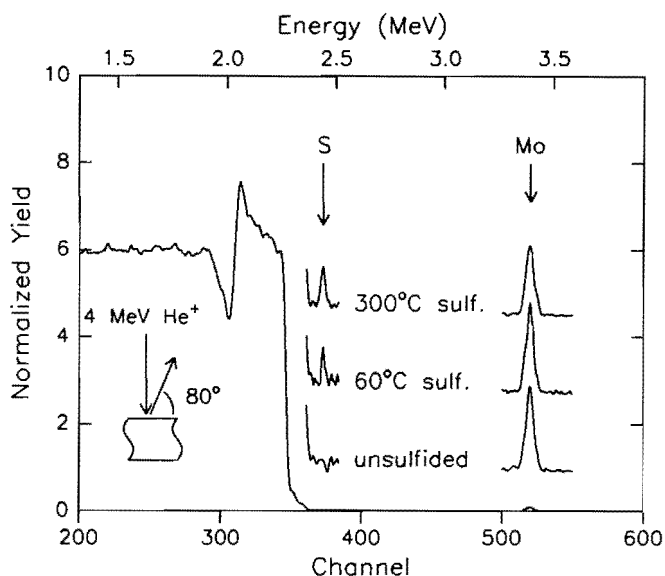


Figure 3.2

RBS spectra of the $\text{MoO}_3/\text{SiO}_2$ model catalysts after sulfidation in 1 bar of $\text{H}_2\text{S}/\text{H}_2$ for 3 hours at the indicated temperatures. The inset shows the scattering geometry. The S and Mo peaks are magnified by a factor 20.

catalyst made by spin coating from MoO_2Cl_2 in ethanol. The particles appear round in the plane parallel to the support with diameters in the range of approximately 100-150 nm, and have maximum thicknesses between 5 and 10 nm. Analysis of different parts of the spin coated wafer reveals that the macroscopic spreading of particles on a scale of centimeters is quite satisfactory, although on the micrometer scale the local density of particles varies somewhat. The AFM picture of Figure 3.1 corresponds to one of the more densely populated regions.

RBS spectra taken from eight different parts of the wafer (see Figure 3.2 for an example) indicate that the samples contain between 1.1×10^{15} and 1.4×10^{15} Mo atoms per cm^2 (Table 3.3). As the diameter of the incident ion beam is about 2 mm, the results confirm that the spin coating procedure results in a satisfactory macroscopic spreading of the deposited particles. This means that different samples from one wafer appear homogeneous with respect to XPS, RBS and SIMS which probe areas in the order of several mm^2 .

The XPS spectrum of the freshly prepared sample (Figure 3.6) yields a binding energy of 232.6 eV for the Mo $3d_{5/2}$ peak, consistent with Mo^{6+} ions as in MoO_3 (Table 3.1). Measurement of the Cl 2p region showed no detectable signal due to chlorine, in agreement with the instability of MoO_2Cl_2 in air. SIMS spectra (Figure 3.8) reveal the characteristic

Table 3.1*Binding energies of Mo and S in reference compounds.*

state	compound	E_B (eV)	reference
Mo^{6+}	MoO_3	232.6	21
		232.5	16
		232.4	17,18
		232.6	this work
Mo^{5+}		230.9-231.4	18
		230.8	21
Mo^{4+}	MoO_2	229.4	16
		229.2	17
		229.1	18,21
	MoS_2	228.9	16
		228.8	17
	228.8	20	
	228.7	this work	
Mo^0	Mo	227.7	19
S^{2-}	MoS_2	162.2	16
		161.6	17
		161.9	20
		161.5	this work
S_2^{2-}	FeS_2	162.5	this work
SH^-		161.5-162.9 ^a	22
S^0	S_n, S_8	164.1	19
		164.4	this work

^{a)} S $2p_{3/2}$ binding energy of thiol ligands in a series of nickel complexes

positive and negative secondary ion patterns of MoO_3 , as we discuss later on. The negative SIMS spectrum showed only trace amounts of Cl^- ions at the usual impurity levels detected in SIMS.

Thus the freshly impregnated catalyst consists of MoO_3 particles of lateral diameter between 100 and 150 nm, thickness on the order of 5-10 nm, and a good macroscopic spreading over the model support. AFM studies show that the particles can be heated in air to approximately 325 °C without affecting their shape significantly, whereas heating at temperatures above 350 °C results in serious sintering and volatilization [23].

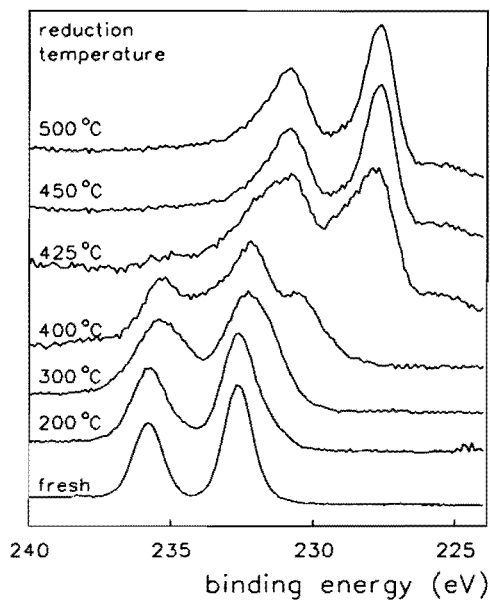


Figure 3.3
XPS spectra of the Mo 3d region of the MoO₃/SiO₂/Si(100) model catalyst after reduction at the indicated temperatures.

Table 3.2

XPS binding energies, line widths, intensities and assignments for the spectra in Figure 3.3.

T _{red} (°C)	BE (eV)	fwhm (eV)	I (kcounts·eV/s)	assignment
-	232.6	1.20	4.17	Mo ⁶⁺ in MoO ₃
200	232.6	1.50	4.72	Mo ⁶⁺ in MoO ₃
300	232.2	2.21	4.53	Mo ⁶⁺
400	232.2	1.53	1.00	Mo ⁶⁺
	230.5	2.00	1.03	Mo ⁵⁺
425	231.9	1.50	0.20	Mo ⁶⁺
	230.4	1.42	0.16	Mo ⁵⁺
	228.8	1.80	0.58	Mo ⁴⁺
	227.7	1.29	0.61	Mo ⁰
450	227.5	0.95	1.47	Mo ⁰
500	227.5	0.90	1.06	Mo ⁰

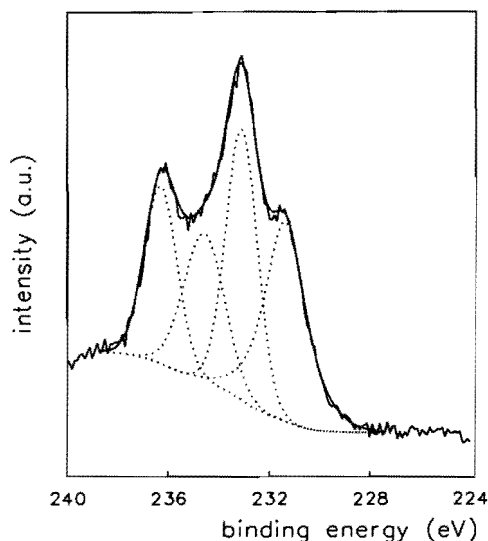


Figure 3.4

Fit of the Mo 3d XPS spectrum, obtained from the catalyst after reduction at 400 °C. The smooth solid line shows the total envelope of the fitted spectrum, whereas the dashed curves represent the separate components.

3.3.2 Reduction of MoO₃/SiO₂/Si(100)

Figure 3.3 shows the XPS spectra of the MoO₃/SiO₂/Si(100) model catalyst after reduction in H₂ at different temperatures. Upon reduction at 200 and 300 °C the peaks of the Mo 3d doublet of the Mo⁶⁺ species broaden on the lower binding energy side, indicating a slight reduction and a less defined MoO₃ structure. After reduction at 400 °C the spectrum can be resolved in a Mo⁶⁺ and a Mo⁵⁺ doublet. Above 400 °C most of the molybdenum is reduced to a molybdenum state with a binding energy of 227.7 eV, corresponding to metallic Mo (Table 3.1). After reduction at 500 °C there is only Mo⁰ left. The asymmetry of the XPS peaks is characteristic of metallic samples. Thomas et al. [24] found with TPR that MoO₃ on a silica support reduces at 480 °C for a low loading, i.e. less than 3 wt%, of MoO₃. Considering that reductions for a given length of time under isothermal conditions proceed further than in temperature programmed reductions, this is in reasonable agreement with our results of MoO₃ on a silica model support, which indicate that significant reduction does not occur until approximately 400 - 425 °C. The results clearly show that MoO₃ in H₂ reduces to metallic molybdenum above 400 °C. In Table 3.2 the results of the fits of the Mo 3d spectra are listed, showing the different molybdenum species that occur during reduction. From Table 3.2 we can also see that the Mo 3d signal diminishes significantly at high temperatures (the Si 2p signal remained about constant for all measurements). This means that molybdenum is sintering or evaporating from the surface as stated in section 3.3.1.

To give an impression of how the different types and amounts of molybdenum are obtained from the XPS spectra, a typical fit of a Mo 3d spectrum is shown in Figure 3.4.

Table 3.3

Loadings of Mo and S and the S/Mo atomic ratio as determined from the RBS spectra of sulfided MoO₃/SiO₂/Si(100) model catalysts.

T _{sulf} °C	Mo loading atoms / cm ²	S loading atoms / cm ²	S/Mo atomic ratio
-	1.2×10 ¹⁵	-	-
20	1.1×10 ¹⁵	1.6×10 ¹⁵	1.45
60	1.3×10 ¹⁵	1.6×10 ¹⁵	1.23
100	1.3×10 ¹⁵	2.7×10 ¹⁵	2.08
125	1.2×10 ¹⁵	3.1×10 ¹⁵	2.58
150	1.4×10 ¹⁵	3.0×10 ¹⁵	2.15
200	1.3×10 ¹⁵	2.9×10 ¹⁵	2.23
300	1.3×10 ¹⁵	3.2×10 ¹⁵	2.46

errors in Mo and S loading: 5%; in S/Mo: 10%

This spectrum matches with two Mo 3d doublets. The ratio of the areas of the Mo 3d_{5/2} and the Mo 3d_{3/2} peaks is kept at 6:4, corresponding to the electron occupancy of those levels.

3.3.3 Sulfided model catalysts

RBS spectra were taken of all sulfided catalysts. Two representative spectra of catalysts sulfided at 60 and 300 °C are shown in Figure 3.2. The large continuum below 2.3 MeV is due to the silicon substrate. Both the peaks due to Mo and S were integrated and loadings of Mo and S atoms were calculated, see Table 3.3. The S/Mo atomic ratio (Figure 3.5) calculated from the RBS spectra is between 1 and 1.5 for the catalysts sulfided at room temperature and at 60 °C, but increases to values between 2 and 2.5 when the sulfidation temperature is 100 °C or higher.

Figure 3.6 shows the Mo 3d and S 2p XPS spectra of the MoO₃/SiO₂/Si(100) model catalysts after sulfidation for 3 hours at different temperatures. Sulfidation in H₂S/H₂ at room temperature shifts the Mo 3d spectrum from the Mo⁶⁺ position to a lower binding energy of 229.9 eV, characteristic of molybdenum in a 4+ oxidation state (Table 3.1). This value would be consistent with MoO₂, but the presence of oxysulfide species or molybdenum bronzes is conceivable as well, as will be argued later. As Figure 3.6 shows, this Mo⁴⁺ state predominates in catalysts sulfided up to 100 °C. Sulfidation at 125 °C and higher gives a Mo 3d_{5/2} XPS signal with a binding energy of 228.4-228.9 eV, characteristic of Mo⁴⁺ ions in MoS₂ (Table 3.1). In addition to Mo, also the S 2s peak is visible at binding energies around 226 eV. The results of the fits of these spectra are given in Table 3.4.

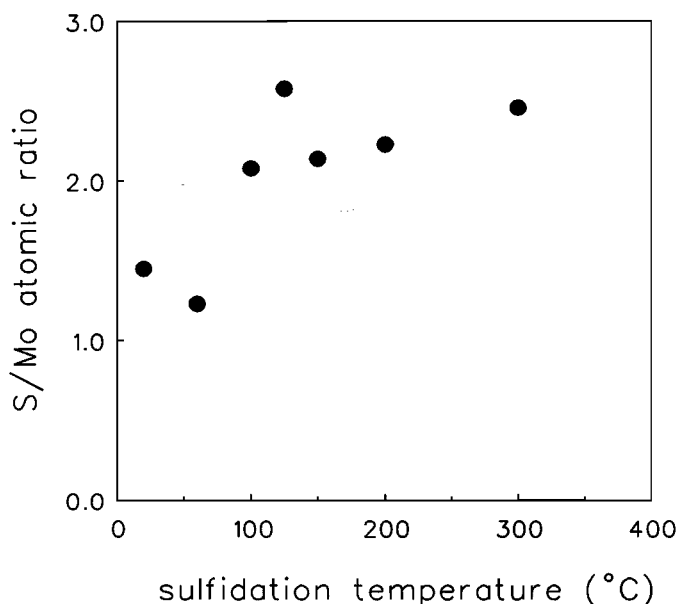


Figure 3.5

S/Mo atomic ratio for the $\text{MoO}_3/\text{SiO}_2$ model catalysts as a function of sulfidation temperature, determined from RBS.

Figure 3.6 also contains the S 2p spectra of the sulfided model catalysts. The step in the background from 159 to 165 eV is an artifact of the silicon substrate. In order to facilitate the interpretation, we measured the S 2p spectra of three reference compounds, MoS_2 (S^{2-}), FeS_2 (S_2^{2-}) and elemental sulfur, see Figure 3.7 and Table 3.1. The spectra obtained after sulfidation of the model catalysts up to 150 °C appear broader than after sulfidation at 300 °C. The latter spectrum can successfully be fitted with one S 2p doublet, with a S $2p_{3/2}$ binding energy of 161.7 eV, in agreement with the presence of S^{2-} ions (Table 3.1). In order to fit the other spectra, a second doublet has been included, with a S $2p_{3/2}$ binding energy of 162.2–162.9 eV. The value expected for elemental sulfur is significantly higher, 164.4 eV (Table 3.1). Possible assignments for the intermediate sulfur species are disulfide ions, S_2^{2-} , as occur for example in FeS_2 , or sulfhydryl groups [22], SH^- . As first, SH^- groups are highly unstable and not expected to survive evacuation and secondly SIMS spectra do not support the presence of SH^- , as we discuss later on, we prefer the interpretation in terms of S_2^{2-} groups. All binding energies are given in Table 3.4.

The intensity ratio of the total S 2p and Mo 3d signals in Table 3.4 show a maximum of about 0.4 at sulfidation temperatures of 60 and 100 °C. The maximum value is significantly higher than the S 2p / Mo 3d ratio of 0.33 measured from a completely sulfided catalyst consisting entirely of MoS_2 . In the discussion section we argue that sulfur is concentrated at the outside of the particles.

Static SIMS, although hindered by mass interferences of cluster ions containing O_2 and S (both 32 amu), also reflects the conversion of MoO_3 into MoS_2 . The top of Figure 3.8

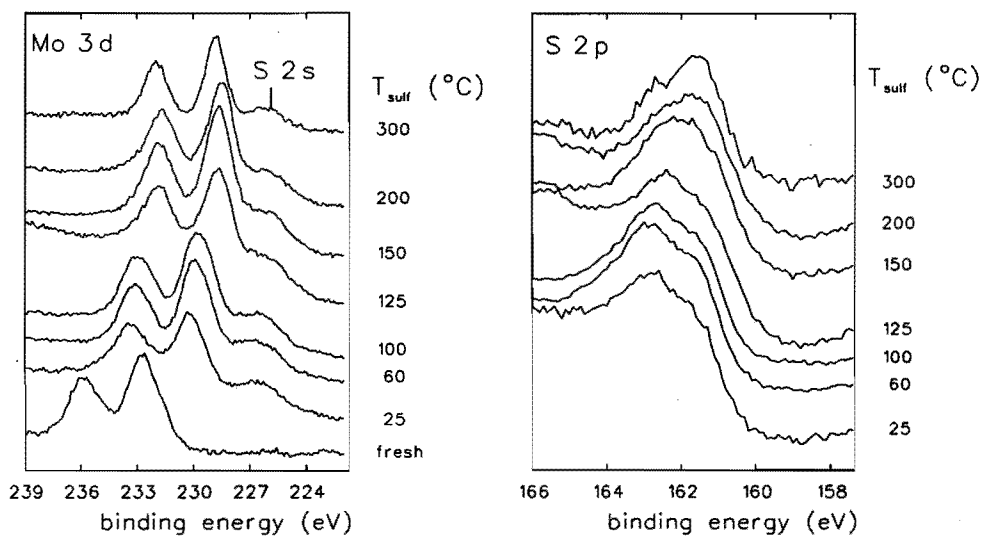


Figure 3.6

XPS spectra of the $\text{MoO}_3/\text{SiO}_2$ model catalysts after sulfidation in $\text{H}_2\text{S}/\text{H}_2$ for 3 hours at the indicated temperatures for the Mo 3d and S 2s region (left) and the S 2p region (right).

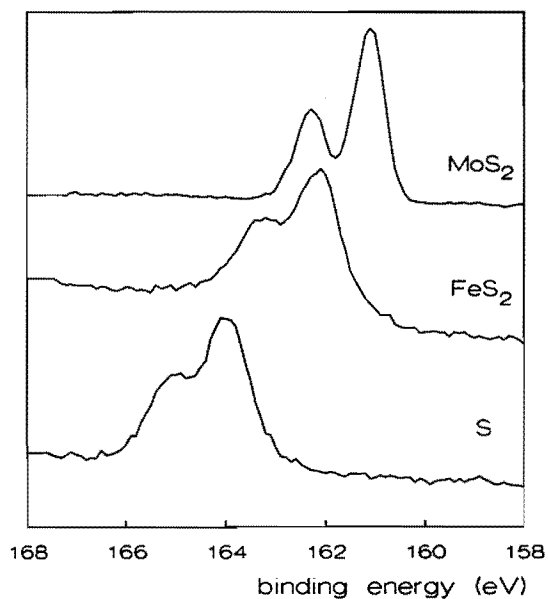


Figure 3.7

XPS S 2p reference spectra of MoS_2 (S^{2-}), FeS_2 (S^-) and elemental sulfur (S^0).

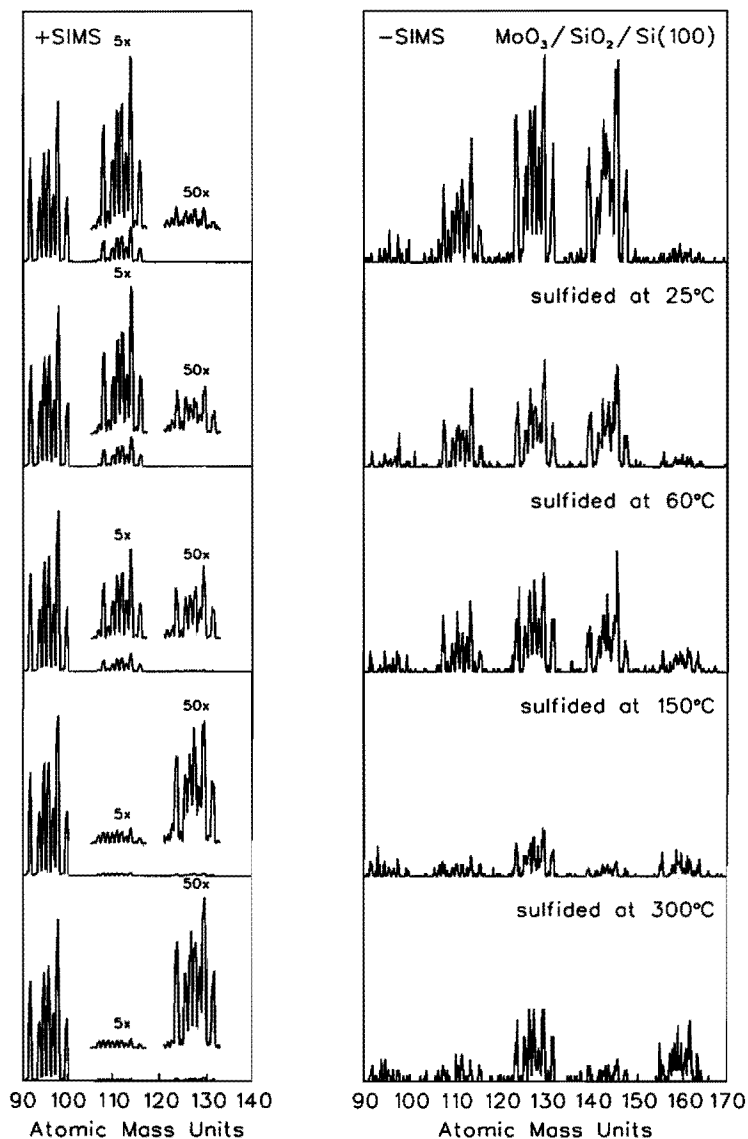


Figure 3.8

Positive (left) and negative (right) static SIMS spectra of the MoO₃/SiO₂/Si(100) model catalysts, after impregnation (top) and after sulfidation at the indicated temperatures, showing the transition from MoO₃ to MoS₂. The patterns are associated with Mo (92-100 amu), MoO (108-116), MoS + MoO₂ (124-132), MoSO + MoO₃ (140-148), and MoS₂ + MoSO₂ + MoO₄ (156-164).

Table 3.4

XPS binding energies, linewidths, intensities, assignments and total S/Mo XPS intensity ratios for the spectra in Figure 3.6.

T _{sulf} (°C)	state	B.E. (eV)	FWHM (eV)	I (kceV/s)	assignment	S/Mo XPS
-	Mo 3d	232.6	2.18	6.4	Mo ⁶⁺ in MoO ₃	-
25	Mo 3d	232.4	2.14	2.5	Mo ⁶⁺	.31
		229.9	2.13	19.7	Mo ⁴⁺	
	S 2p	161.5	1.44	4.3	S ²⁻	
		162.7	1.40	2.6	S ₂ ²⁻ (SH)	
60	Mo 3d	229.6	1.96	31.1	Mo ⁴⁺	.44
	S 2p	161.5	1.48	7.8	S ²⁻	
		162.9	1.59	5.9	S ₂ ²⁻ (SH)	
100	Mo 3d	229.6	2.04	31.0	Mo ⁴⁺	.41
	S 2p	161.5	1.46	7.5	S ²⁻	
		162.8	1.54	5.3	S ₂ ²⁻ (SH)	
125	Mo 3d	230.0	1.70	2.8	Mo ⁴⁺	.34
		228.4	1.73	12.6	Mo ⁴⁺	
	S 2p	161.0	1.37	3.2	S ²⁻	
		162.2	1.44	2.1	S ₂ ²⁻ (SH)	
150	Mo 3d	230.2	1.62	4.4	Mo ⁴⁺	.34
		228.5	1.72	30.9	Mo ⁴⁺	
	S 2p	161.3	1.63	8.8	S ²⁻	
		162.4	1.43	3.1	S ₂ ²⁻ (SH)	
200	Mo 3d	230.1	1.69	3.8	Mo ⁴⁺	.29
	S 2p	228.4	1.64	27.5	Mo ⁴⁺	
		161.4	1.60	9.0	S ²⁻	
300	Mo 3d	228.9	1.46	1.5	Mo ⁴⁺	.33
	S 2p	161.7	1.47	0.5	S ²⁻	

error in I: 1-5%

shows positive and negative static SIMS spectra of the freshly prepared, oxidic catalyst. The most intense isotopic pattern in the positive SIMS spectrum (left) is due to elemental Mo⁺ (92-100 amu). As molecular cluster ions of oxides and sulfides are thought to result from direct emission [25], the higher mass clusters of MoO⁺ (108-116 amu) and MoO₂⁺ (124-132 amu) give information about the coordination of molybdenum. The positive SIMS

spectrum shows no indication for the presence of residual Cl from the MoO_2Cl_2 precursor. The negative SIMS spectrum of the same sample is shown in the top right corner of Figure 3.8. Elemental Mo^- peaks are barely visible, but MoO^- , MoO_2^- , and MoO_3^- patterns are clearly distinguished. Although with lower intensity, even MoO_4^- peaks appear.

The positive SIMS spectra in Figure 3.8 confirm that sulfidation at relatively low temperatures, 25 and 60 °C, already results in significant uptake of sulfur by the catalyst, as evidenced by the increase in the $(\text{Mo} + 32)^+$ signal, associated with both MoO_2^+ and MoS^+ clusters, and the decrease in the $(\text{Mo} + 16)^+$ signal, which is unambiguously assigned to MoO^+ . We note however that the surface region of the catalyst contains both oxygen and sulfur after sulfidation at 25 and 60 °C.

Sulfidation at 150 °C increases the sulfur and decreases the oxygen content further, while the pattern measured after sulfidation at 300 °C resembles that of a MoS_2 reference compound, indicating that sulfidation is complete. The low residual MoO intensity is probably due to the intimate contact of the MoS_2 particles with the oxidic support.

The negative SIMS spectra also show the conversion of MoO_3 to MoS_2 , but in a more indirect way. Here a clear SIMS sensitivity effect is apparent: MoS_x^- clusters have much lower intensities than MoO_x^- clusters [26]. Nevertheless, the relative intensities of the MoO_x^- clusters decrease clearly with increasing sulfidation temperature, indicating that the original oxygen coordination of Mo is disrupted by the sulfidation. Direct evidence for Mo-S contact is given by the relative increase in the intensities of the $(\text{Mo} + 32)^-$ and $(\text{Mo} + 64)^-$ clusters.

Negative SIMS spectra of the low mass range (not shown) revealed the sulfur isotopes at 32 and 34 amu, while peaks due to SH^- ions at 33 and 35 amu are not observed. As the work of Karolewski and Cavell [26] demonstrates that the SH^- ion is readily detected by SIMS, we take the absence of SH^- signals in the spectra of the sulfided model catalysts as evidence that SH groups are not present. The spectra also showed a peak at 64 amu, attributed to S_2^- , with increasing intensity along with the sulfidation. However, this peak does not necessarily confirm the earlier invoked S_2^{2-} species, as the S_2^- fragment in SIMS is also obtained from MoS_2 .

3.4 Discussion

The application of RBS, XPS, and SIMS gives absolute Mo and S concentrations along with oxidation states of these elements, as well as information on the anions in the first coordination shell of Mo. Such data provide detailed insight into the Mo and S species present in intermediate sulfidation stages of molybdenum on a flat conducting silica model support. We summarize the most important results of the sulfidation study:

- RBS spectra show that the S:Mo atomic ratio is around 1-1.5 for sulfidation at 25 and

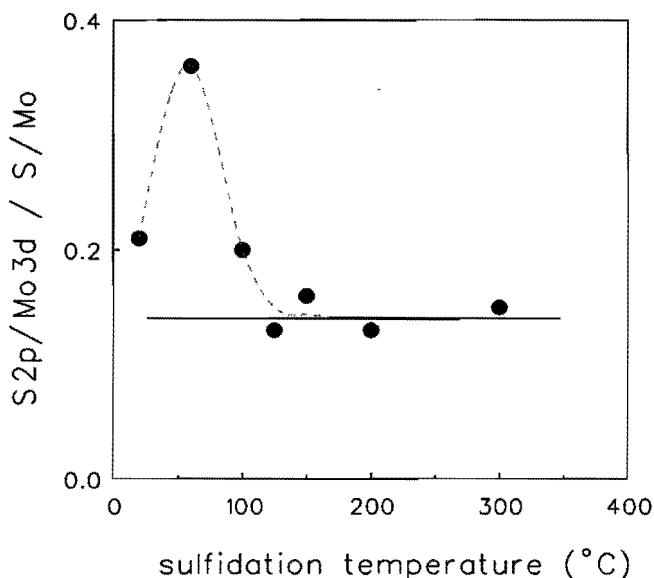


Figure 3.9

The XPS S/Mo intensity ratio divided by the RBS S/Mo atomic ratio, which is a measure for the concentration gradient between sulfur at the outside and in the interior of the particles.

60 °C, while the S:Mo ratio increases to 2-2.5 for sulfidation temperatures of 100 °C and higher.

- XPS S 2p spectra reveal the presence of at least two sulfur species, one is S^{2-} as in MoS_2 , the other has a binding energy consistent with S_2^2 species. The latter disappears from the spectra for sulfidation temperatures between 150 and 200 °C. Evidence for the presence of elemental sulfur has not been found.
- Mo 3d XPS spectra show that the initially present Mo^{6+} converts largely to Mo^{4+} at room temperature. The binding energy of this Mo state that predominates in catalysts sulfided at temperatures up to 100 °C is characteristic of Mo^{4+} in an oxidic environment and is significantly higher than that of MoS_2 . Sulfidation at temperatures above 125 °C leads to formation of MoS_2 .
- The S 2p / Mo 3d XPS intensity ratio is higher after sulfidation at 60 and 100 °C than after high temperature sulfidation.
- The static SIMS spectra, characteristic of the outer surface layers of the particles, show that the surface is incompletely sulfided at 25 and 60 °C, and that Mo atoms can have both O and S neighbours. The spectra contain no evidence for the presence of SH^- groups at any sulfidation temperature.

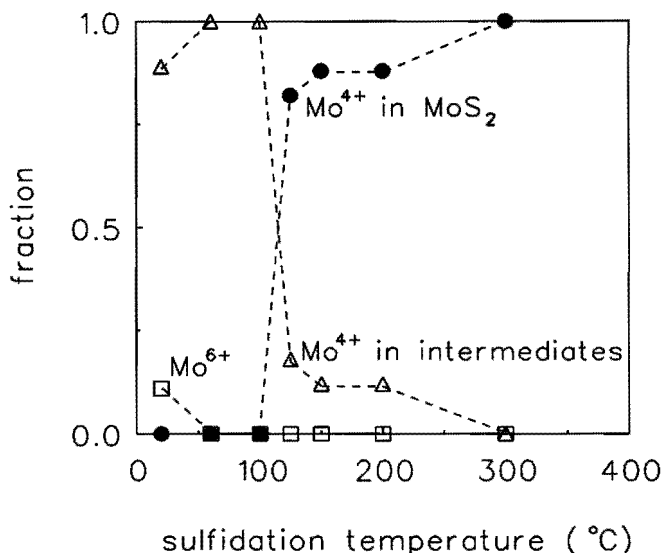


Figure 3.10

Contribution of Mo^{n+} species to the XPS spectra of $\text{MoO}_3/\text{SiO}_2$ model catalysts as a function of sulfidation temperature.

The Mo XPS spectra logically suggest to discuss sulfidation in terms of two temperature ranges: The low regime from 25-100 °C, where MoS_2 is absent, and the temperature regime above 100 °C, where MoS_2 dominates the XPS spectra.

Sulfidation at low temperatures results in an appreciable sulfur concentration gradient between the surface region and the interior of the particles. This is most evident if one plots the S 2p / Mo 3d XPS intensity ratio divided by the true S/Mo atomic ratio determined with RBS, as has been done in Figure 3.9. The thus obtained parameter has a value of about 0.15 for completely sulfided particles, i.e. where S and Mo are homogeneously mixed, but is significantly higher at low sulfidation temperatures. When a surface sensitive technique such as XPS detects a higher S/Mo ratio than a bulk sensitive technique such as RBS does, it implies that the sulfur concentration at the surface is higher than in the interior towards the particle support interface.

As to the state of Mo after low temperature sulfidation, the Mo 3d binding energy is similar to that of MoO_2 and, presumably also to that of MoO_xS_y . The presence of the latter is strongly suggested by the S 2p spectra which clearly show that sulfur is present in anionic form and not as elemental sulfur. Hence, it must be coordinated to the Mo^{4+} cation, but in a form different than in MoS_2 , which is absent at temperatures up to 100 °C. Because the molecular clusters in SIMS clearly show that Mo in the surface of the catalyst can be

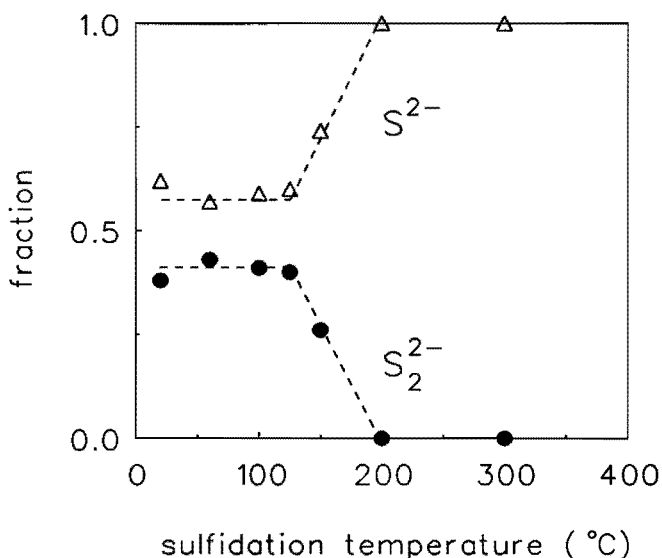


Figure 3.11

Contribution of sulfur species to the XPS spectra of MoO₃/SiO₂ model catalysts as a function of sulfidation temperature.

coordinated by S and by O, we propose that the surface region of catalysts sulfided at low temperatures consists of Mo(IV) oxysulfides, of the general type Mo⁴⁺O_xS_y, where sulfur is present in two states, S²⁻ and S₂²⁻. As to the disulfide, Polz et al. [27] detected S₂²⁻ in sulfided MoO₃/Al₂O₃ catalysts by means of Raman spectroscopy.

Because of the sulfur concentration gradient discussed above, we argue that the catalysts sulfided at temperatures of 100 °C and lower consist of Mo(IV) oxysulfides in the surface region. The fact that the S/Mo atomic ratio corresponds already to 1 for sulfidation at 25 and 60 °C, combined with the result that all sulfur is in anionic form and thus necessarily coordinated to molybdenum, implies that oxysulfide formation cannot be limited to the outer atomic layer, but that appreciable penetration of sulfur to some depth must have occurred.

At higher temperatures, the intermediate Mo(IV) phases convert to MoS₂. The S/Mo atomic ratio is between 2 and 2.5, i.e. somewhat higher than the expected ratio of 2. This has been noted in other studies as well [6,28]. Evidence for the occurrence of zero-valent Mo, as invoked in the sulfidation mechanism of Arnoldy et al. [4] discussed in the introduction (reactions 5 and 6), has not been found, implying that Mo⁰, if involved, appears only as a transient intermediate. Figures 3.10 and 3.11 summarize the type of Mo and S species detected by XPS, as a function of sulfidation temperature.

Figure 3.12 gives the type of sulfur species in terms of the S²⁻/Mo and S₂²⁻/Mo atomic

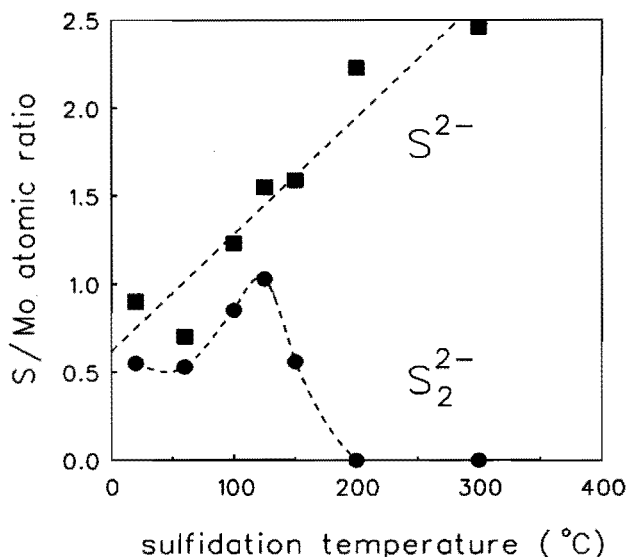


Figure 3.12

Atomic ratios S^{2-}/Mo and S_2^{2-}/Mo calculated by multiplying the S/Mo atomic ratio from RBS by the fractions of S^{2-} and S_2^{2-} as determined from XPS.

ratios. These data were calculated by combining the relative contributions of each type of sulfur from XPS (Figure 3.11) with the total S/Mo atomic ratio from RBS (Figure 3.5). By doing so, we implicitly assume that both types of sulfur species are geometrically similarly distributed through the particles, which does not have to be the case. If, for example, the S_2^{2-} species were preferentially located at the outside of the particles (which is conceivable in view of the high S/Mo ratio observed in XPS at low sulfidation temperatures), then the S_2^{2-}/Mo and S^{2-}/Mo atomic ratio would be over- and underestimated, respectively. Figure 3.12 indicates that sulfide formation increases progressively with increasing sulfidation temperature, whereas the S_2^{2-} species appears only at intermediate sulfidation temperatures and maximizes around 100-125 °C. We suggest that this S_2^{2-} is the species that gives rise to the simultaneous H_2 consumption and H_2S evolution peaks which start around 150 °C in the TPS spectra [4], reflecting its removal through hydrogenation.

It is interesting that exposure of the fresh catalyst to H_2S and H_2 at room temperature is sufficient to reduce the majority of the initially Mo^{6+} ions to the Mo^{4+} state. The experiments on the reduction of $MoO_3/SiO_2/Si(100)$ in H_2 revealed no reduction of Mo^{6+} at temperatures below 300 °C (see section 3.2.2). We attribute the reduction of Mo^{6+} to Mo^{4+} at low temperatures to the presence of molybdenum(oxy)sulfides at the surface, which provides sites where molecular hydrogen adsorbs dissociatively. Moyes and coworkers [29] have shown

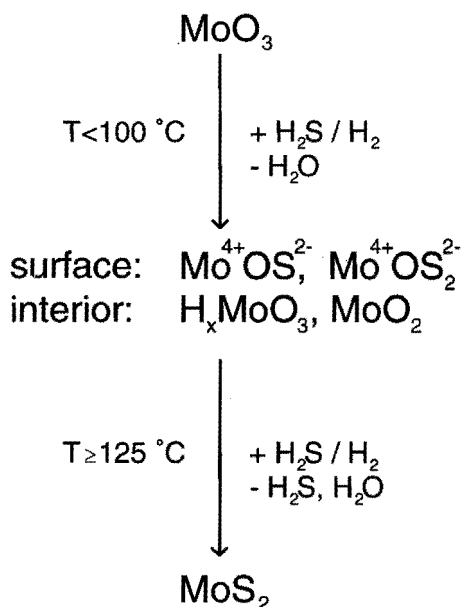


Figure 3.13
Schematic representation of the sulfidation mechanism of MoO₃/SiO₂ model catalysts as based on surface spectroscopic data.

that H-D exchange, indicative of dissociative adsorption, occurs on MoS₂ at a range of temperatures. According to Moyes, dissociative adsorption of hydrogen on molybdenum sulfide is likely to occur at room temperature as well [30]. In this respect it is interesting that Polz et al. [27] suggested that S₂²⁻ in sulfided catalysts play a role in the splitting of hydrogen. As Figure 3.12 shows, these S₂²⁻ species are abundantly present after sulfidation at low temperature. We think that hydrogen atoms thus formed diffuse into the particles and reduce Mo⁶⁺ to Mo⁴⁺.

The phase formed at low temperature in the interior of the particles is probably a hydrogen molybdenum bronze, H_xMoO₃, with x ≤ 2. These phases are known to form when Pt-doped MoO₃ is exposed to H₂, in which platinum provides sites where dissociation of H₂ occurs [31,32]. According to Sotani and Hasegawa [32], a bronze with the nominal composition H_{0.83}MoO₃ is stable at temperatures up to about 120°C, at which it starts to decompose under evolution of water. Hence, we suggest that the Mo(IV) species formed in the interior of the particles after sulfidation at temperatures between 25 and 125 °C are hydrogen molybdenum bronzes.

Summarizing, the spectroscopic results suggest the following mechanism for the sulfidation of MoO₃/SiO₂/Si(100), see Figure 3.13. Again we stress that the mechanism emphasizes the stable phases present under equilibrium as seen by XPS and SIMS, rather than the reactions leading to their formation as detected in TPS.

For sulfidation temperatures below 100 °C there is rapid O-S exchange in the surface

region leading to Mo(IV) oxysulfide formation and accompanied by bulk reduction to molybdenum bronzes or MoO_2 , attributed to the facilitated dissociation of molecular H_2 by the partially sulfided surface. The latter contains two sulfur species: S^{2-} and most probably S_2^{2-} , although SH^- cannot entirely be excluded. Above 125 °C the MoO_xS_y and molybdenum bronzes or MoO_2 phases convert to MoS_2 , while the S_2^{2-} species disappear, most probably because of hydrogenation to H_2S .

With regard to the mechanism of Arnoldy et al. [4] discussed in the introduction, our results support the involvement of oxysulfidic Mo species (although with Mo in the 4+ oxidation state) and Mo(IV) oxides in intermediate sulfidation stages, although we think that hydrogen molybdenum bronzes are more likely to be present than MoO_2 . We exclude the presence of elemental sulfur on the basis of the S 2p XPS spectra. The S_2^{2-} species we propose instead would equally well explain the evolution of H_2S observed in the TPS spectra reported by Arnoldy et al. [4]. We have found no evidence for the occurrence of Mo metal as a stable intermediate to MoS_2 , although we can of course not exclude its involvement as a transient species.

3.5 Final remarks

The results presented here are valid for rather large MoO_3 particles which have little interaction with the underlying SiO_2 support. As such the results provide a reference with which the sulfidation of more dispersed particles can be compared. One of the aims of this work was to explore the merits of the approach of using flat, thin oxide layers as model supports and using surface science techniques for characterization of the model catalysts in the study of the sulfidation mechanism of hydrotreating catalysts. We have shown that this approach works very well and that it yields valuable information about the sulfidation mechanism. We intend to exploit this approach to study the sulfidation of the industrially relevant alumina-supported molybdenum and cobalt-molybdenum catalysts.

Further experiments on the sulfidation of silica-supported molybdenum catalysts [33] have pointed out that the results as presented in this chapter are typical of the sulfidation of a catalyst with a high water content. Arnoldy et al. [4] found that a higher water content of the catalyst facilitates the sulfidation. This was explained by assuming that the O-S exchange was a proton catalyzed reaction. As wet catalysts contain a large amount of Brønsted acid sites, which accelerate the proton transfer, the O-S exchange reaction will be enhanced. Another explanation is that water may alter the structure of the MoO_3 surface [33]. If the formation of Brønsted acid sites is accompanied with the breaking up of bridged oxygen species upon hydrolysis with water, the number of terminal oxygen species is increased. This could also enhance the O-S exchange.

Although no evidence is found for elemental sulfur species, their presence can not entirely

be excluded, since the vapour pressure of sulfur is higher than 1×10^{-9} mbar at room temperature. This means that small amounts of loosely bound elemental sulfur would have been vaporized before they could be measured. However, even if small amounts of elemental sulfur were present, the proposed mechanism remains largely valid.

Recent results of XPS measurements on molybdenum-sulfur complexes [34] confirmed the assignment of the sulfur species with a binding energy of 162.7 eV to a S₂²⁻ species. It appears that this binding energy is typical of a bridged bonded S₂²⁻-group. It was also shown however, that the binding energy of a terminal S₂²⁻-group coincides with that of a S²⁻ species. This means that in the results presented here, the presence of an additional terminal S₂²⁻ species can not entirely be excluded. Such an additional S₂²⁻ species might explain the S/Mo ratio of 2.2 after the high temperature sulfidation.

References

- [1] R. Prins, V.H.J. de Beer and G.A. Somorjai, *Catal. Rev. - Sci. Eng.* **31**, 1 (1989).
- [2] H. Topsøe and B.S. Clausen, *Catal. Rev. - Sci. Eng.* **26**, 395 (1984).
- [3] B. Scheffer, P. Arnoldy and J.A. Moulijn, *J. Catal.* **112**, 516 (1988).
- [4] P. Arnoldy, J.A.M. van den Heijkant, G.D. de Bok and J.A. Moulijn, *J. Catal.* **92**, 35 (1985).
- [5] B. Scheffer, E.M. van Oers, P. Arnoldy, V.H.J. de Beer and J.A. Moulijn, *Appl. Catal.* **25**, 303 (1986).
- [6] P. Mangnus, V.H.J. de Beer and J.A. Moulijn, *Appl. Catal.* **67**, 119 (1990).
- [7] P.A. Spevack and S. McIntyre, *Appl. Catal.* **64**, 191 (1990).
- [8] N.S. McIntyre, T.C. Chan, P.A. Spevack and J.R. Brown, *Appl. Catal.* **63**, 391 (1990).
- [9] A. Jiménez-González and D. Schmeisser, *J. Catal.* **130**, 332 (1991).
- [10] L.M. Eshelman, A.M. de Jong and J.W. Niemantsverdriet, *Catal. Lett.* **10**, 210 (1991).
- [11] H.J. Borg, L.C.A. van den Oetelaar, L.J. van IJzendoorn and J.W. Niemantsverdriet, *J. Vac. Sci. Technol. A* **10**, 2737 (1992).
- [12] A.M. de Jong, L.M. Eshelman, L.J. van IJzendoorn and J.W. Niemantsverdriet, *Surf. Int. Anal.* **18**, 412 (1992).
- [13] P.L.J. Gunter, A.M. de Jong, J.W. Niemantsverdriet and H.J.H. Rheiter, *Surf. Int. Anal.* **19**, 161 (1992).
- [14] E.W. Kuipers, C. Laszlo and W. Wieldraaijer, *Catal. Lett.* **17**, 71 (1993).
- [15] H.L. Hagedoorn, J.W. Broer and F. Schutte, *Nucl. Instr. and Meth.* **86**, 253 (1970).
- [16] T.A. Patterson, J.C. Carver, D.E. Leyden and D.M. Hercules, *J. Phys. Chem.* **80**, 1702 (1976).
- [17] D.S. Zingg, L.E. Makovsky, R.E. Tischer, F.R. Brown and D.M. Hercules, *J. Phys. Chem.* **84**, 2898 (1980).
- [18] A. Cimino and B.A. De Angelis, *J. Catal.* **36**, 11 (1975).
- [19] C.D. Wagner, W.M. Riggs, L.E. Davis, J.F. Moulder and G.E. Muilenberg, *Handbook of XPS*, Perkin Elmer Corporation, Eden Prairie MN, USA, 1978.
- [20] I. Alstrup, I. Chorkendorff, R. Candia, B.S. Clausen and H. Topsøe, *J. Catal.* **77**, 397 (1982).
- [21] J.E. de Vries, H.C. Yao, R.J. Baird and H.S. Gandhi, *J. Catal.* **84**, 8 (1984).
- [22] S. Srivastava, *Appl. Spectr. Rev.* **22**, 401 (1986).
- [23] R. Gubbels, S. Pateras and J.W. Niemantsverdriet, to be published.
- [24] R. Thomas, E.M. van Oers, V.H.J. de Beer and J.A. Moulijn, *J. Catal.* **84**, 275 (1983).
- [25] H. Oechsner in *Secondary Ion Mass Spectrometry SIMS III, Proc. 3rd Int. Conf.*, A. Benninghoven, J. Giber, J. Laszlo, M. Riedel and H.W. Werner, Eds.; Springer, Berlin, p. 106, 1982.
- [26] M.A. Karolewski and R.G. Cavell, *Surf. Sci.* **219**, 261 (1989).

- [27] J. Polz, H. Zeilinger, B. Müller and H. Knözinger, *J. Catal.* **120**, 22 (1989).
- [28] S.M.A.M. Bouwens, R. Prins, V.H.J. de Beer and D.C. Koningsberger, *J. Phys. Chem.* **94**, 3711 (1990).
- [29] R.B. Moyes in *Hydrogen Effects in Catalysis*, P. Paal and G. Menon, Eds.; Dekker, New York, p. 583, 1988.
- [30] R.B. Moyes, personal communication, 1992.
- [31] D. Tinet, P. Canesson, H. Estrade and J.J. Fripiat, *J. Phys. Chem. Solids* **41**, 583 (1979).
- [32] N. Sotani and M. Hasegawa, *Polyhedron* **5**, 71 (1986).
- [33] R.M. van Hardeveld, graduation report (1993).
- [34] T. Weber, J.C. Muijsers and J.W. Niemantsverdriet, to be published.

4 Reflection absorption infrared spectroscopy

4.1 Introduction

The most widely used vibrational spectroscopies in the study of adsorbates on single crystal surfaces are electron energy loss spectroscopy (EELS) and reflection absorption infrared spectroscopy (RAIRS). Both techniques yield information about the adsorbate, present on the surface, and the adsorption sites.

EELS [1] makes use of a monochromatic beam of low energetic electrons, interacting with the adsorbed molecules. The electrons excite the vibrational modes of the molecules and lose a corresponding amount of energy. The intensity of the reflected beam is measured as a function of the energy, yielding a spectrum, in which the peaks correspond to the vibrational modes of the adsorbate. The main advantages of EELS are that a large spectral region can easily be accessed, typically from 5000 to 100 cm^{-1} , and that all vibrations may be excited (not only the dipole active ones). However, the use of electrons implies that EELS can only be performed under high vacuum conditions.

RAIRS is based on the interaction of an infrared beam with the dipole active modes of adsorbed molecules from which only those modes can be observed with a component perpendicular to the surface. This is the so called surface dipole selection rule. Routinely the spectral range from 4000 to 800 cm^{-1} can be accessed. However, with special detectors like liquid helium cooled bolometers, even vibrations down to 50 cm^{-1} can be observed. The main advantages of RAIRS are the high resolution at which spectra can be acquired, about ten times higher than with EELS, and the ability to perform measurements under atmospheric conditions, due to the relatively high permeability of many gases for infrared radiation. The high resolution makes RAIRS a very suitable technique to study interactions between adsorbed molecules and between the adsorbate and the substrate, since these affect the peak shape and position.

In this chapter the principles of RAIRS will be discussed, together with the information that can be obtained from RAIRS spectra. For more detailed discussions on the background and theory of RAIRS we refer to the reviews by Hoffmann [2], Hollins and Pritchard [3] and Chabal [4].

4.2 Theoretical considerations for the RAIRS experiment

The basic rules of the RAIRS experiment were laid down by Greenler [5] in 1966. From this [5] and following papers [6-9] dealing with the theoretical aspects of RAIRS, the

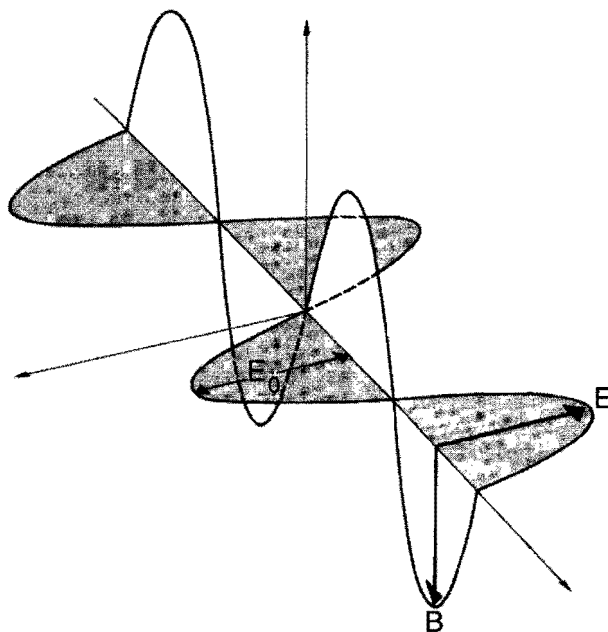


Figure 4.1

Representation of electromagnetic radiation with an oscillating electric (E) and magnetic (B) field.

following considerations proved to be important:

- The metallic surface imposes a strict dipole selection rule; only vibrations with a dipole moment perpendicular to the surface will be excited, demanding that the incident light should have an electric field component in the plane of incidence (p-polarized).
- The incident light should be reflected at the metal surface at near grazing incidence.
- For many metals little advantage is gained by using multiple reflections, which is especially important for single crystal studies, since a single reflection simplifies the experimental setup greatly.

To get insight into the principles of RAIRS, first the basics of the reflection of light from a metal surface will be briefly explained [10,11]. Light can be described as a harmonic wave (Figure 4.1) with an oscillating electric and magnetic field. The electric field of such a harmonic wave is described by:

$$E(\mathbf{r},t) = E_0 e^{i(\mathbf{k}\cdot\mathbf{r} - \omega t)} \quad (4.1)$$

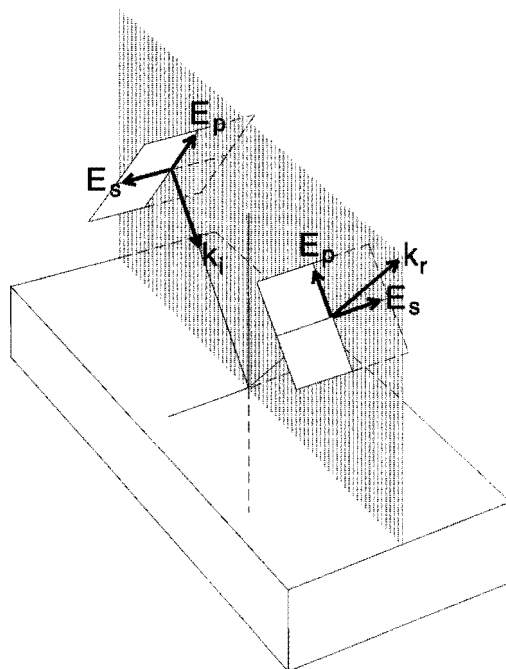


Figure 4.2

Light reflecting from a metal surface. The electric fields of the incident (k_i) and reflected (k_r) beams can be composed of an electric field vector in the plane of incidence (E_p) and one perpendicular to the plane of incidence (E_s).

in which E_0 is the amplitude of the harmonic wave and k is the propagation vector of magnitude $2\pi/\lambda$ where λ is the wavelength. Electromagnetic radiation that falls on a surface will partially be reflected and partially refracted. The electric field of the radiation can be described by two components, one with the electric field vector in the plane of incidence, the other with the electric field perpendicular to the plane of incidence (Figure 4.2). Radiation with the electric field in the plane of incidence E_p is called p-polarized (p standing for *parallel*) and with the electric field perpendicular to the plane of incidence E_s is called s-polarized (s standing for *senkrecht*).

For the RAIRS experiment the reflection of light on metals, and in particular on the vacuum-metal interface is important. Due to the high absorption of metals for electromagnetic radiation, the index of refraction of metals is complex [11], $\tilde{n}=n+ik$, in which n is the normal refractive index and k represents the absorption of the medium, i.e. the extinction coefficient. For an externally incident plane wave (Equation (4.1)), the amplitude of the electric field on the vacuum side of the vacuum-metal interface, follows from the Maxwell equations. For a beam impinging on a surface at an angle of incidence θ

(with respect to the surface normal) the electric field for s-polarized light at the surface, after Chabal [4] is:

$$E_s = E_s(\text{incident}) + E_s(\text{reflected}) = \left[1 - \frac{\sqrt{\tilde{n}^2 - \sin^2 \theta} - \cos \theta}{\sqrt{\tilde{n}^2 - \sin^2 \theta} + \cos \theta} \right] E_0 \quad (4.2)$$

For p-polarization the electric field of the component parallel to the surface is:

$$E_p^{\parallel} = E_p^{\parallel}(\text{incident}) + E_p^{\parallel}(\text{reflected}) = \left[1 - \frac{\tilde{n}^2 \cos \theta - \sqrt{\tilde{n}^2 - \sin^2 \theta}}{\tilde{n}^2 \cos \theta + \sqrt{\tilde{n}^2 - \sin^2 \theta}} \right] \cos \theta E_0 \quad (4.3)$$

and for the component perpendicular to the surface:

$$E_p^{\perp} = E_p^{\perp}(\text{incident}) + E_p^{\perp}(\text{reflected}) = \left[1 + \frac{\tilde{n}^2 \cos \theta - \sqrt{\tilde{n}^2 - \sin^2 \theta}}{\tilde{n}^2 \cos \theta + \sqrt{\tilde{n}^2 - \sin^2 \theta}} \right] \sin \theta E_0 \quad (4.4)$$

The index of refraction for metals is large, implying, as can be seen from Equations (4.2) and (4.3), that the reflected electric field amplitudes, E_s and E_p^{\parallel} , are close in magnitude but opposite in sign to the incident field. The s-polarized light undergoes a phase shift of 180° upon reflection for all angles of incidence. The parallel component of the p-polarized light is phase shifted over 180° for all angles until the nominator of the term between brackets in Equation (4.3) becomes zero. At this angle, the Brewster angle, there is no reflection of p-polarized light. The phase shift of 180° results in a node, set up at the surface due to destructive interference, resulting in a net amplitude of the electric field in the order of E_0/\tilde{n} . The electric field component of the p-polarized light perpendicular to the surface E_p^{\perp} does not suffer from a 180° phase shift, and the reflected field adds constructively to the incident field, thus the electric field perpendicular at the surface is enhanced. It is clear that there is only significant interaction of the reflecting infrared light with molecules which have a changing dipole moment with a component perpendicular to the surface, since there is no essential electric field parallel to the surface. This is one of the reasons for the surface dipole selection rule. The other reason is the interaction of the vibrating dipole with its image in the surface. When a dipole is placed above a metal surface the conducting electrons rearrange themselves to screen the dipole field.

At high angles of incidence, a large resultant field E_p is established on the surface. The

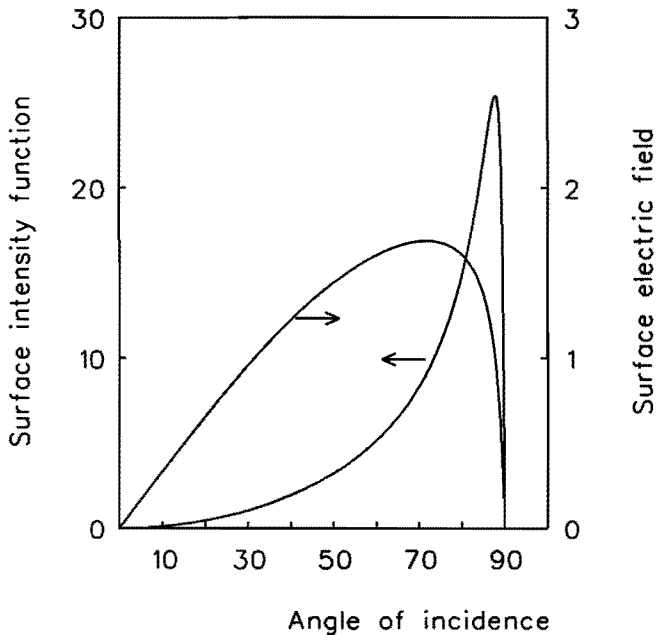


Figure 4.3

Surface electric field and surface intensity function as function of the angle of incidence for p-polarized light reflecting from a metal surface.

intensity of absorption depends on the square of the surface electric field E_p and the number of molecules over which the field is exerted [2]. From this the function for the surface intensity $E_p^2 \sec \theta$ is obtained. Figure 4.3 shows the surface electric field and the surface intensity function as a function of the angle of incidence for p-polarized electromagnetic radiation reflecting from a metal surface. It is clear that reflection absorption experiments need to be performed at high angles of incidence, since the function is sharply peaked close to grazing incidence (between 85° and 90°) [9]. In practice, RAIRS is performed at 80° or 85° , because of geometric constraints like sample size and beam divergence.

The intensity of infrared absorption bands in RAIRS is expressed in the absorption factor or reflectivity change:

$$\frac{\Delta R}{R} \equiv \frac{(R^0 - R)}{R^0} \quad (4.5)$$

This change in reflectivity arises from the presence of an adsorbing surface layer. R and R^0 are the reflectivities of the substrate with and without the surface layer respectively.

Greenler [9] showed that there is an optimum number of reflections, at which an optimal reflectivity change is obtained. However, after Greenler [9] and Hoffmann [2], it appears that for transition metals a single reflection already yields a ΔR that is close (70 to 90 %) to the optimum value, caused by the energy loss accompanying multiple reflections.

Considering the surface dipole selection rule, it is obvious that the s-polarized component of infrared light does not interact with adsorbed molecules at the surface. Therefore, one would expect that it is advantageous to filter out the s-polarized component, since it does not contribute to the RAIRS spectrum. We will deal with this effect in some more detail.

In the case of reflection of unpolarized light, both the reflected s- and p-component enter the detector and contribute to the intensity:

$$I^0 = I_s^0 + I_p^0 \quad (4.6)$$

Here I is the intensity of the reflected light and the superscript 0 denotes the intensity when no absorber is present on the surface. When an adsorbate is present on the surface, absorbing infrared light, the reflected intensity is:

$$I = I_s + I_p \quad (4.7)$$

Since the s-component of the reflecting light does not interact with the adsorbate, we can write Equation (4.7) as:

$$I = I_s^0 + I_p \quad (4.8)$$

Now the reflectivity change is given by:

$$\frac{\Delta R}{R} = \frac{I^0 - I}{I^0} = \frac{I_s^0 + I_p^0 - I_s^0 - I_p}{I_s^0 + I_p^0} = \frac{I_p^0 - I_p}{I_s^0 + I_p^0} \quad (4.9)$$

Considering that the intensities of the reflected s- and p-components are proportional to the squares of the electric fields, we can see from Equations (4.2) to (4.4) that the intensity of the reflected s-light is equal or higher than for p-light. From Equation (4.9) now follows that the reflectivity change increases at least by a factor of two, by filtering out the s-component. This means that the intensity of observed absorption bands, using a polarizer, is at least a factor of two higher.

Since the intensity of the light falling on the detector, using a polarizer, is about half the intensity without a polarizer, the noise level is expected to be twice as high [12]. Thus the signal to noise ratio is not much improved by using only the p-polarized component of the infrared light. However, increasing the intensity of the incident infrared beam in experiments with a polarizer could effectively result in an equal intensity of the detected light as in an experiment without a polarizer. Then the absorption is still enhanced by a factor of two and the noise levels remain the same, resulting in an enhancement of the signal to noise ratio of two. Of course, one could also increase the intensity of the incident beam without a polarizer. However, in practice the total intensity that can be used in an experiment is limited, due to detector saturation. It is thus advantageous to use a polarizer, filtering out the s-polarized component of the infrared light.

Concluding, for the optimal RAIRS experiment on metal single crystal surfaces, the infrared beam reflects from the surface at a high angle of incidence in a single reflection and a polarizer is used, allowing only the p-polarized component to be detected.

4.3 Vibrational frequency of molecules adsorbed on metal surfaces

It is well known [1,13] that the vibrational frequency of the internal stretch mode of a molecule adsorbed on a metal changes with respect to its gas phase value. The frequency of adsorbed molecules depends strongly on the adsorption site and geometry. This was first recognized by Eischens et al. [14] for the adsorption of CO on supported metal particles measured with infrared transmission spectroscopy. These authors interpreted the different CO stretch frequencies as a result of CO species bonded to different sites. The assignment of the different frequencies was based on the analogy of metal carbonyls. In general the vibrational frequency for adsorbed CO is lowered from its gas phase value of 2143 cm^{-1} to values between 2000 and 2100 cm^{-1} in the linear position, 1900 and 2000 cm^{-1} when bridged bonded and below 1900 cm^{-1} for three- or fourfold bonded positions.

The shift of the vibrational frequency from the gas phase value of a single adsorbed molecule can be attributed to several factors. The fact that an adsorbed molecule is attached to a more or less rigid substrate results in a mechanical shift of the internal frequency of the molecule. Hoffmann [2] estimated from a simple model of masses and springs, an increase of about 50 cm^{-1} for an adsorbed CO molecule. Screening of the dipole field by the conducting electrons in the metal results in an image dipole in the metal. After Hoffmann [2] the interaction of the adsorbed dipole and its own image in the metal surface results in a downward shift of about $30\text{-}50\text{ cm}^{-1}$ for the CO stretch frequency. It is clear that these effects alone cannot explain the observed strong frequency shift of adsorbed CO molecules and the site dependence of the frequency. This site dependence of the vibrational frequency is largely a result of a chemical shift, i.e. a change in the electronic structure, as the molecule binds to the surface.

When a CO molecule adsorbs on a transition metal, a chemical bond is made by the interaction of the molecular orbitals of the CO molecule and the d-electrons of the metal [15,16]. The interaction between the CO 5σ and d_{z^2} orbital of the metal results in two new molecular orbitals. The bonding orbital has mainly a 5σ character and is lowered in energy with respect to the 5σ orbital in free CO. The antibonding orbital has a d_{z^2} character and is shifted upwards in energy. Another set of bonding and antibonding orbitals is formed by interaction between the $2\pi^*$ orbital of the CO molecule and the d_{xy} and d_{xz} orbitals of the metal. When this bonding orbital falls below the Fermi level it is filled and contributes to the bonding of the CO molecule to the metal. This molecular orbital has, on the other hand, an antibonding character for the C-O interaction, resulting in a weakening of the C-O bond and consequently a lowering of the CO stretch frequency. For steric reasons, the overlap of the $2\pi^*$ orbital with the metal orbitals is higher, when the CO molecule is bound in a higher coordinated site. This is the reason that the CO stretch frequency is lower for CO molecules bonded in a higher coordinated site.

The vibrational frequency of adsorbed CO molecules tends to increase with increasing coverage, due to intermolecular interactions. These interactions can be distinguished in vibrational coupling (e.g. dipole-dipole coupling) and interactions of a chemical nature (e.g. reduction of the strength of the metal-CO bond or repulsive interactions). The two effects can be separated [17] by using mixtures of different isotopes of the adsorbed molecule.

The most important vibrational interaction is the long range dipole-dipole coupling. It originates from the fact that a vibrating molecule gives rise to a long range oscillating dipole field, which is sensed by the other adsorbed molecules [18]. In the first model to describe these dipole interactions, by Hammaker et al. [17], only the direct interaction between the dipoles was considered. Mahan and Lucas [19] made an improvement by taking into account the contribution from the images and the electronic polarizability of the molecules. Still the observed frequency shifts could not be explained entirely. Persson et al. [20,21] developed a theory, which included the effect of screening of the external field by the electronic polarizability of the adsorbed molecules. With this theory a good description of the observed frequency shifts as a function of the coverage can be obtained. For an extensive discussion on this theory to describe these dipole interactions we refer to the paper by Persson and Ryberg [21].

The chemical interactions can be understood on the basis of the chemical bonding picture given above. With increasing coverage there is a competition for backdonation electrons among the adsorbed molecules [22,23]. Now the $2\pi^*$ orbitals of the CO molecules get less occupied, resulting in an upward shift of the CO stretch vibrational frequency.

Experimentally it is possible to distinguish between the vibrational coupling and chemical frequency shifts by using isotopic mixtures. Hammaker et al. [17] have shown that only molecules with the same vibrational frequency couple strongly. Thus it is possible to attain vibrational decoupling of neighbouring molecules by using isotopic mixtures with sufficiently large difference in vibrational frequency. King and co-workers [24,25] showed, using

isotopic mixtures of ^{12}CO and ^{13}CO , that the frequency shift for the adsorption of CO on Pt(111) is entirely caused by dipole coupling.

The vibrational frequency of adsorbed molecules can also be influenced by other processes, like coupling to thermally low vibrational modes. Since these processes have only minor effects and are not of much importance in catalytically relevant studies, we refer for these processes to the work of Gadzuk and Luntz [26], Ryberg [18] and Tobin [27]. In general the vibrational frequency reveals which molecule is adsorbed on which site in the surface. In combination with the surface dipole selection rule one can then conclude that the observed mode has a changing dipole moment perpendicular to the surface. Frequency shifts as a function of coverage yield information on interactions between adsorbate molecules.

4.4 Intensity and line shape of infrared absorption bands

The intensity of an infrared absorption band is proportional to the dynamic dipole moment [2] of the adsorbed molecule from which the band arises and the number of adsorbed molecules. Therefore, comparing the intensity of the bands of different adsorbates, the intensity can not directly be translated to a relative amount of the adsorbed species. For example, the intensity of an absorption band of a hydrocarbon species is only a few tenths of a percent, whereas the intensity of a CO or NO band at a comparable coverage is typically a few percent. This is due to the small dipole moments of hydrocarbons compared to those of CO and NO. One even has to take into account a difference of the dipole moments, when comparing intensities of the absorption bands of a single adsorbate, present in different sites (see for an example the discussion of the occupation of CO on bridged and linear sites on Rh(100) in Chapter 6).

The infrared absorption band intensity of an adsorbate layer increases with increasing coverage. However, there is no linear relation between this intensity increase and the coverage. At higher coverage this intensity increase is reduced. Persson and Ryberg [21] developed a model, similar to that describing the frequency shift due to dipole interactions, that describes the reduction of the intensity increase very well. For the theory and details behind this model we refer to the paper of Persson and Ryberg [21].

The line shape of an infrared absorption band of an adsorbed species can be affected by several processes [2]. The line width can be homogeneously broadened by damping of the vibration due to interaction of the vibrating molecule with the metal surface such as phonon coupling or electron-hole pair creation. Inhomogeneous broadening arises from an inhomogeneous distribution of individual oscillator frequencies determined by the molecule's adsorption site. Vibrational coupling between molecules and inhomogeneity of the intermolecular distances gives also rise to inhomogeneous broadening of the absorption band. These processes have been described by Gadzuk and Luntz [26], Tobin [27], Hoffmann [2] and Ryberg [18]. For our purposes it is sufficient to realise that a well ordered adsorbate

layer results in a narrow symmetric peak. The observation of broadened and asymmetric peaks is an indication that the adsorbate overlayer is distorted in some way.

References

- [1] H. Ibach and D.L. Mills, *Electron energy loss spectroscopy and surface vibrations*, Academic press inc., New York, 1982.
- [2] F.M. Hoffmann, *Surf. Sci. Rep.* **3**, 107 (1983).
- [3] P. Hollins and J. Pritchard, *Progr. Surf. Sci.* **19**, 275 (1985).
- [4] Y.J. Chabal, *Surf. Sci. Rep.* **8**, 211 (1988).
- [5] R.G. Greenler, *J. Chem. Phys.* **44**, 310 (1966).
- [6] R.G. Greenler, *J. Chem. Phys.* **50**, 1963 (1969).
- [7] J.D.E. McIntyre and D.E. Aspnes, *Surf. Sci.* **24**, 417 (1971).
- [8] R.G. Greenler, R.R. Rahn and J.P. Schwartz, *J. Catal.* **23**, 42 (1971).
- [9] R.G. Greenler, *J. Vac. Sci. Technol.* **12**, 1410 (1975).
- [10] R.W. Ditchburn, *Light* vol. 2, 3rd ed., Academic press, London, 1976.
- [11] E. Hecht and A. Zajac, *Optics*, 4th ed., Addison-Wesley publishing company, Massachusetts, 1979.
- [12] Y.P. Song, M.C. Petty and J. Yarwood, *Vibrational Spectr.* **1**, 305 (1991).
- [13] R.P. Eischens and W.A. Pliskin, *Advan. Catal.* **10**, 1 (1958).
- [14] R.P. Eischens, W.A. Pliskin and S.A. Francis, *J. Chem. Phys.* **22**, 1786 (1954).
- [15] R.A. van Santen, A. de Koster and T. Koerts, *Catal. Lett.* **7**, 1 (1990).
- [16] J.W. Niemantsverdriet, *Spectroscopy in Catalysis*, VCH, Weinheim, 1993.
- [17] R.M. Hammaker, S.A. Francis and R.P. Eischens, *Spectrochim. Acta* **21**, 1295 (1965).
- [18] R. Ryberg in *Advances in chemical physics*, K.P. Lawley, Ed.; John Wiley & Sons Ltd., p. 1, 1989.
- [19] G.D. Mahan and A.A. Lucas, *J. Chem. Phys.* **68**, 1344 (1978).
- [20] B.N.J. Persson and A. Liebsch, *Surf. Sci.* **110**, 356 (1981).
- [21] B.N.J. Persson and R. Ryberg, *Phys. Rev. B* **24**, 6954 (1981).
- [22] G. Blyholder, *J. Phys. Chem.* **68**, 2773 (1964).
- [23] G. Blyholder, *J. Phys. Chem.* **79**, 756 (1975).
- [24] R.A. Shigeishi and D.A. King, *Surf. Sci.* **58**, 379 (1976).
- [25] A. Crossley and D.A. King, *Surf. Sci.* **68**, 528 (1977).
- [26] J.W. Gadzuk and A.C. Luntz, *Surf. Sci.* **144**, 429 (1984).
- [27] R.G. Tobin, *Surf. Sci.* **183**, 226 (1987).

5 Apparatus for reflection absorption infrared spectroscopy on metal single crystals

5.1 Introduction

Studies on metal single crystal surfaces play an important role in understanding fundamental aspects of catalytic reactions. In an ultrahigh vacuum (UHV) environment well defined single crystal surfaces and reaction conditions can be obtained. Numerous spectroscopic techniques are then available to examine the processes developing on the surface. Reflection absorption infrared spectroscopy (RAIRS) is a very suitable technique to study adsorbed molecules on metal surfaces. It reveals information about the adsorption site geometry and adsorbate interactions. The additional advantage of RAIRS is that it is also applicable at higher pressure conditions, in contrast with most other surface spectroscopies. This makes RAIRS a technique which is able to make a link between *surface science* and *catalysis under high pressure conditions*.

In this chapter an apparatus is described to perform RAIRS experiments on well defined single crystal surfaces under UHV and high pressure conditions. The UHV chamber contains additional techniques for sample cleaning and characterization. Auger electron spectroscopy (AES) is used to check the surface cleanliness. With low energy electron diffraction (LEED) the single crystalline nature of the surface can be checked. LEED also provides information about ordered overlayer structures of adsorbates. Thermal desorption spectroscopy (TDS) monitors reaction and desorption products as a function of temperature.

5.2 Techniques

5.2.1 Reflection absorption infrared spectroscopy

The theory, experimental considerations and topics concerning RAIRS have been dealt with in chapter 4. In this section only an outline is given.

RAIRS is performed by reflecting an IR beam on a metal surface at near grazing incidence. Only the p-component of the IR light, i.e. the component with the electric field in the plane of incidence, interacts with an adsorbed molecule. The *surface dipole selection rule* dictates that only a molecule with a dynamic dipole moment having a component perpendicular to the surface can be detected with RAIRS [1,2].

Due to the long travelling path of IR light in gaseous atmospheres, RAIRS can also be

performed under high pressure conditions. This is in contrast with many other surface sensitive techniques, which make use of electrons or ions, requiring high vacuum conditions.

From the frequency of an absorption band the adsorbate and the specific adsorption site can be identified. The molecular symmetry can be determined through the surface dipole selection rule and the number of observed vibrational modes [1]. Frequency shifts with changing coverage probe intermolecular interactions within the adsorbate layer. The halfwidth and intensity of the absorption band give information about the homogeneity of the adsorbate layer, energy transport between the adsorbate and metal substrate, and the dynamic dipole moment of the adsorbate [1].

5.2.2 Low energy electron diffraction

An extensive overview of LEED is given by Van Hove et al. [3], here we will only deal with some of the basics. LEED is used to determine the periodically ordered structure of surfaces and adsorbed overlayers [4]. It is based on the diffraction of low energy electrons. A monoenergetic low energy electron beam, typically between a few to some hundreds eV, impinges on the surface and is scattered back. The mean free path of electrons at such energies in a solid is very small, which makes the technique very surface sensitive. The elastically backscattered electrons show constructive interference in particular directions corresponding to the structure of the surface they were scattered from.

Electrons can be considered as electromagnetic radiation with a wavelength given by the De Broglie relation:

$$\lambda = \frac{h}{p} = \frac{h}{\sqrt{2m_e E_{kin}}} \quad (5.1)$$

in which:

- λ is the wavelength of the electron
- h is Planck's constant (6.63×10^{-34} Js)
- p is the momentum of the electron
- m_e is the mass of the electron (9.11×10^{-31} kg)
- E_{kin} is the kinetic energy of the electron in eV

Now constructive interference of the backscattered electrons occurs in those directions where the difference in the travelled path equals a whole number of wavelengths. These directions are given by the Bragg relation:

$$n \lambda = a (\sin \varphi_r - \sin \varphi_i) \quad (5.2)$$

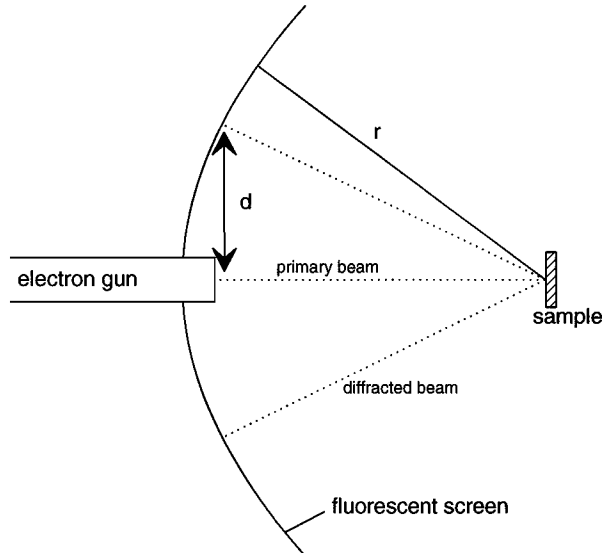


Figure 5.1

Schematic setup for the LEED experiment. A primary electron beam impinges on the surface of the sample, which is in the focus of the hemispherical fluorescent screen at a distance r . The diffracted beams appear as spots on the screen and the distance d is a direct measure for the diffraction angle.

in which:

n is the order of diffraction

λ is the wavelength of the diffracted electron (\AA)

a is the distance between the periodically ordered scatterers; the lattice constant (\AA)

φ_r is the angle between the surface normal and the direction of the diffracted electron; the diffraction angle

φ_i is the angle between the surface normal and the incident primary electron beam

For a primary electron beam at normal incidence and after substitution of the constants in equation (5.1) the diffraction angle is given by:

$$\sin \varphi_r = \frac{n}{a} \sqrt{\frac{150}{E_{kin}}} \quad (5.3)$$

The setup for a LEED experiment is schematically shown in Figure 5.1. A primary electron beam, originating from the electron gun situated in the centre of the LEED optics,

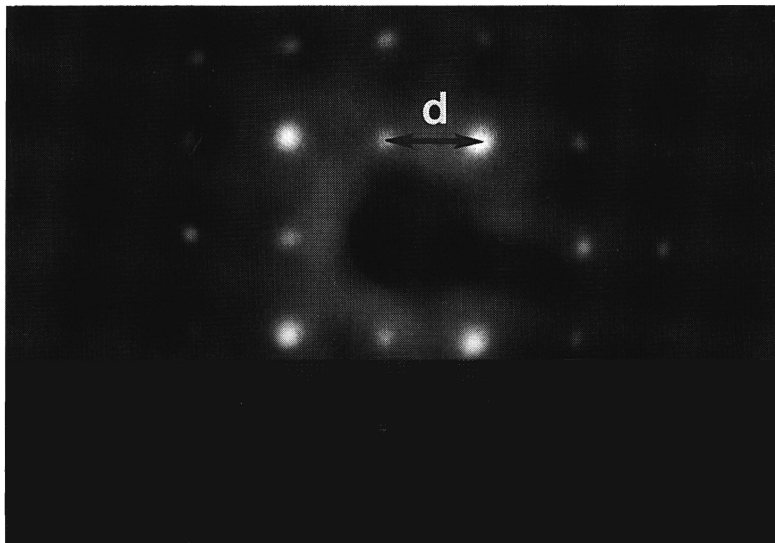


Figure 5.2

LEED pattern of a clean Rh(100) surface. The energy of the primary electron beam was 369.8 eV and the distance d between the diffraction spots on the screen is 14 mm (the photograph is not to scale).

impinges on the sample surface from which it is diffracted. The diffraction directions can be made visible with a fluorescent screen, on which the diffracted electron beams appear as spots. The sample is in the focus of the hemispherical screen, i.e. the distance r from the sample to the screen is always the same. Now the distance d between the spots on the screen of the diffracted and undiffracted electrons is a direct measure for the diffraction angle and thus for the lattice constant. The undiffracted electrons appear as a spot in the centre of the screen, independent of the kinetic energy. This is the so called zeroth order spot.

Figure 5.2 shows a photographic image of a LEED pattern of a clean Rh(100) surface. The energy of the diffracting electrons was 369.8 eV. From the distance d (14 mm) between the diffraction spots and the distance from the sample to the screen (66 mm), $\sin\varphi_r$ is obtained. With Equation (5.3) the lattice constant of 2.7 Å was calculated. This is in good agreement with the interatomic distance of 2.687 Å on a Rh(100) surface. From Equation (5.3) we see that the diffraction angle becomes larger for smaller lattice constants. So a large distance between the diffraction spots corresponds to a small interatomic distance. The LEED pattern corresponds to the so called reciprocal lattice. If a surface lattice is characterized by two base vectors \vec{a} and \vec{b} , the reciprocal lattice is characterized by the base vectors \vec{A} and \vec{B} which satisfy:

$$\vec{a} \cdot \vec{B} = 0 \quad \text{and} \quad \vec{a} \cdot \vec{A} = 1 \quad (5.4)$$

When an adsorbate forms a periodically ordered overlayer, the unit cell of this overlayer follows from the LEED pattern. The overlayer unit cell in reciprocal space can be expressed in terms of the substrate base vectors:

$$\begin{pmatrix} \vec{A}_a \\ \vec{B}_a \end{pmatrix} = \begin{pmatrix} x_1 & y_1 \\ x_2 & y_2 \end{pmatrix} \begin{pmatrix} \vec{A} \\ \vec{B} \end{pmatrix} \quad (5.5)$$

The subscript a denotes the adsorbate overlayer base vectors. Then in real space the overlayer unit cell is expressed by:

$$\begin{pmatrix} \vec{a}_a \\ \vec{b}_a \end{pmatrix} = \frac{1}{x_1 y_2 - x_2 y_1} \begin{pmatrix} y_2 & -x_2 \\ -y_1 & x_1 \end{pmatrix} \begin{pmatrix} \vec{a} \\ \vec{b} \end{pmatrix} \quad (5.6)$$

5.2.3 Auger electron spectroscopy

AES gives qualitative and quantitative information about the composition of the surface region of a material. When a sample is irradiated with an electron beam, secondary electrons arise according to the Auger decay process (Figure 5.3), the so called Auger electrons. The kinetic energy of these electrons is element specific. The number of electrons originating from a particular element is proportional to the concentration of this element in the sample under study.

In AES, atoms in a sample are excited by primary electrons with a kinetic energy typically between 1 and 10 keV. De-excitation occurs by emitting photons or Auger electrons. In Figure 5.3 this process is schematically depicted. First a primary electron removes an electron from a core shell of an atom, with a binding energy E_k . The so formed excited ion relaxes its energy by the Auger de-excitation process. An electron from a higher shell with binding energy E_{l_1} fills the core hole. The energy released in this process is used to emit another electron with binding energy $E_{L_{2,3}}$. The latter is the so called Auger electron. The kinetic energy of this Auger electron is approximately given by:

$$E_{KL_1L_{2,3}} = E_K - E_{L_1} - E_{L_{2,3}} - \delta - \phi \quad (5.7)$$

in which:

$E_{KL_1L_{2,3}}$ is the kinetic energy of the emitted Auger electron

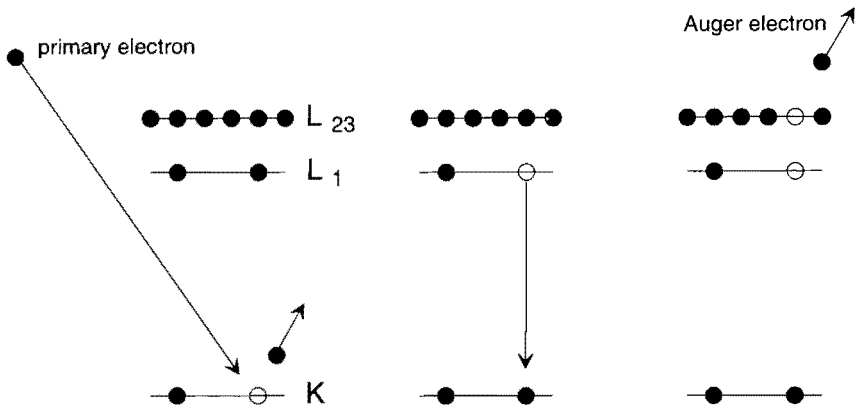


Figure 5.3

Schematic representation of the Auger process. A primary electron removes an electron from a core shell. The formed excited ion relaxes its energy by the Auger decay process. The core hole is filled by an electron from a higher shell and the released energy is used to emit the Auger electron.

- E_K is the binding energy of an electron in the K-shell
- δ is the energy shift caused by relaxation effects, due to the core hole after ionization
- φ is the work function of the sample

As we can see from equation (5.7) the kinetic energy of the Auger electron is independent of the primary electron energy. Thus the kinetic energy is only related to the binding energy of the shells involved in the Auger de-excitation process, which makes it element specific. For the notation of the Auger transitions the X-ray level nomenclature is used. So in this case the KL_1L_{23} transition means that the initial core hole in the K-shell is filled with an electron from the L_1 -shell and the Auger electron is emitted from the L_{23} -shell. When valence levels are involved they are indicated as "V".

The kinetic energy of the Auger electrons is measured and plotted in a spectrum as a function of the intensity. Together with the Auger electrons, many other electrons arise from the sample, caused mainly by inelastic processes of the primary electrons. This produces a large background in the Auger spectrum, on which the Auger signals appear as small peaks. Therefore, Auger spectra are mostly recorded in the derivative mode. It is customary to report energies of Auger transitions as the negative peak of the derivative spectrum.

5.2.4 Thermal desorption spectroscopy

TDS gives information about the kinetics involved in desorption processes and can be used to determine relative coverages of adsorbates. Gases adsorbed on a surface are desorbed by heating the sample with a constant heating rate and detected with a mass spectrometer. The intensity of the specific mass is then plotted as a function of temperature in a TDS spectrum. If readsorption can be neglected, i.e. the pumping speed in the vacuum system is high enough, then the mass spectrometer signal is proportional to the desorption rate. From the TDS spectrum now kinetic parameters, concerning the desorption process, can be determined.

If readsorption does not occur, the rate of desorption is given by:

$$r = \frac{-d\theta}{dt} = k_{des} \theta^n = \nu(\theta) \theta^n e^{-E_d(\theta)/RT} \quad (5.8)$$

in which:

- r is the rate of desorption
- θ is the adsorbate coverage
- t is the time
- k_{des} is the rate constant for desorption
- n is the order of desorption
- ν is the preexponential factor of desorption (s^{-1})
- E_d is the activation energy of desorption (kJ/mol)
- R is the gas constant (8.314×10^{-3} kJ.K/mol)
- T is the temperature (K)

Interactions between adsorbed molecules make ν and E_d coverage dependent. Several procedures to extract these desorption parameters and the desorption order from TDS spectra have been reported in literature [5-10].

The area of the TDS peak is proportional to the amount of desorbed gas and thus to the initial coverage as the desorption experiment started. From a series of TDS spectra taken at different exposures, the coverage as function of the exposure can be obtained. This does not only yield information about the adsorption mechanism involved, but also allows one to calculate the coverage during LEED or RAIRS experiments, if one does not want to desorb the adsorbate overlayer to determine the coverage.

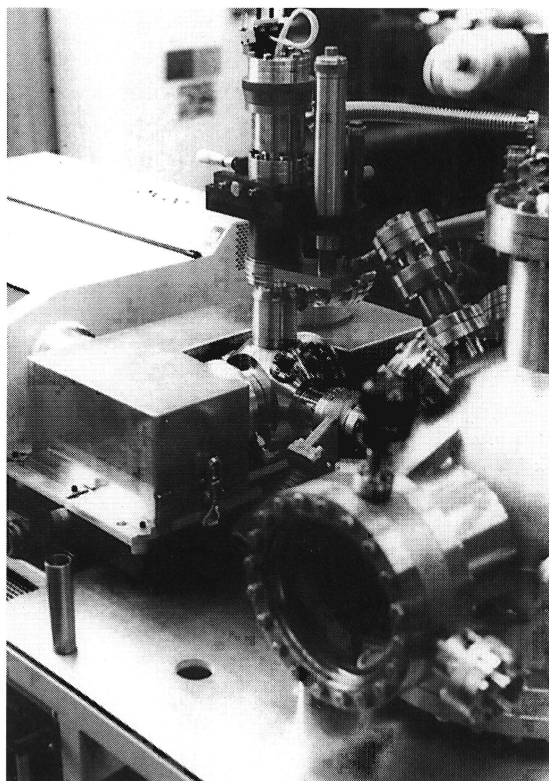


Figure 5.4
Photograph of the apparatus, showing the UHV chamber (right) with the LEED/AES optics (front), the RAIRS cell (centre) and the infrared spectrometer (left).

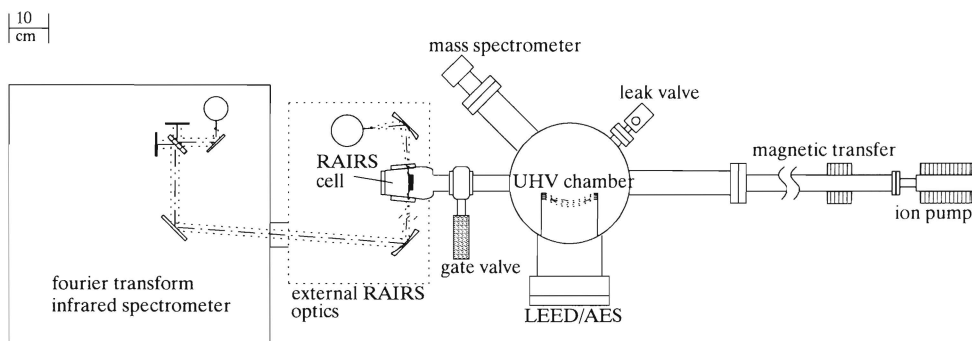


Figure 5.5
Top view of the RAIRS apparatus, showing the UHV chamber and RAIRS cell. The sample is transferred between the two by a magnetically driven transfer rod, which is pumped by an ion pump. The UHV chamber is equipped with LEED/AES optics, a mass spectrometer, a leak valve and a sputter gun (not shown). The RAIRS cell is optically interfaced with a fourier transform infrared spectrometer, and can be separated from the UHV by a gate valve.

5.3 Instrumentation

5.3.1 UHV system

The apparatus (Figure 5.4 and Figure 5.5) consists of an UHV chamber and a separate cell to perform RAIRS, which can be isolated from the main chamber by a gate valve (VAT) to allow high pressure (up to 1 bar) experiments. In the main chamber the single crystal sample can be characterized by LEED, AES and TDS. Both the UHV chamber and the RAIRS cell are fitted with vertically mounted $xyz\theta$ manipulators. The sample is transferred between the two by a magnetically driven transfer rod. The sample manipulation system is based on that published by Raval et al. [11] and will be described in further detail in section 5.3.5.

The pumping organization is schematically depicted in Figure 5.6. The main chamber is pumped by a 360 l/s turbomolecular pump and a water-cooled titanium sublimation pump (Leybold), with a pumping speed of 600 l/s. The backing pump of the turbomolecular pump is a 16 m³/h dual-stage rotary pump, with a base pressure below 1×10^{-4} mbar. The backing pressure is measured with a pirani gauge. The tube housing of the magnetic transfer rod is additionally pumped with a 8 l/s ion pump (Varian). The rotary feedthroughs on both the manipulators and the flanges holding the windows of the RAIRS cell are differentially pumped by a dual-stage rotary pump ($<1 \times 10^{-2}$ mbar). The pressure of the UHV chamber, is monitored by a Bayard-Alpart nude ionization gauge (IG-3, Inficon), situated in the port at the bottom of the chamber leading to the pumps. The advantage of this position is that stray electrons originating from the ionization gauge do not reach the sample, and since the gauge, which has a nonbakeable connector cable, is below the bench pressure monitoring during bakeout is possible. The base pressure after bakeout is typically 2×10^{-10} mbar.

The RAIRS cell can be isolated from the main chamber by a gate valve, to allow high pressure experiments. After such experiments the cell can be separately pumped by a 150 l/s turbomolecular pump, to prevent high gas loadings of the main chamber, and to maintain the UHV-conditions. For this purpose the turbomolecular pump can be bypassed, so that the cell can be roughed out with the rotary pump, till a reasonable vacuum has been achieved, after which the turbomolecular pump can take over. This is especially important in the case of experiments with corrosive gases, which would otherwise wear out the turbo pump very rapidly. When the RAIRS cell is sealed from the main chamber, the pressure in the cell can be monitored with a Penning gauge, allowing pressure measurements from 1×10^{-6} to 1×10^{-2} mbar.

The backing pumps of the turbomolecular pumps are equipped with Al₂O₃ sorption traps, to prevent oil from the rotary pumps to reach the forevacuum of the turbo pumps. After shutdown the system can be vented with dry N₂ gas, that is purified over a zeolite and a CuO trap. Venting valves are situated on both turbomolecular pumps, allowing the UHV chamber and the RAIRS cell or gas system to be vented separately, if necessary.

Gas exposures to the crystal are made with a leak valve situated on the main chamber.

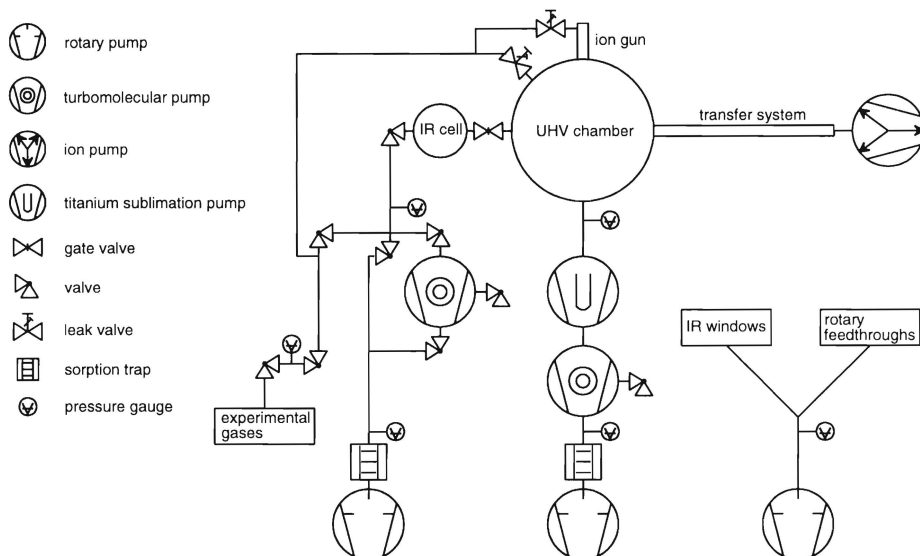


Figure 5.6

Pumping organization of the RAIRS apparatus. The UHV chamber is pumped by a titanium sublimation and a turbomolecular pump, which is backed by a dual stage rotary pump. The transfer system is additionally pumped by an ion pump. The RAIRS cell can be separately pumped by a second turbomolecular pump, when the cell is sealed from the UHV by the gate valve. This turbomolecular pump is also used to pump out the gas manifold. The rotary feedthroughs and the flanges supporting the IR windows are differentially pumped by a separate rotary pump.

The leak valve is connected to a gas manifold system, which can entirely be pumped with a turbomolecular pump, to allow for high purity exposures. The gas manifold consists of copper tubes for the normal gases and a part is fitted with stainless steel pipes, to work with corrosive gases like NO. Both parts are separated by a one-way valve, to prevent the corrosive gases to damage the copper pipes. The gas handling system is also equipped with a valve connected to a glass container, that can be filled with liquids, which makes experiments possible with all kinds of vapours.

Sputter cleaning of the sample is carried out with an argon ion gun (AS-10, VSW). The ion source is equipped with two cathode filaments, the advantage being that, when a filament burns out, the system does not have to be shut down for filament replacement. Typically sputtering is performed with Ar^+ ions with an energy of 500 eV at a beam current of $7 \mu\text{A}/\text{cm}^2$. Assuming a sputter yield of 1, every 30 seconds a monolayer is removed at this beam current.

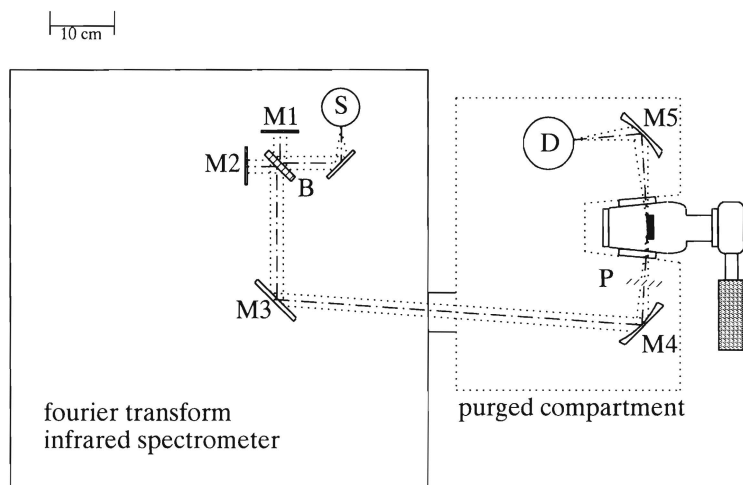


Figure 5.7

The optics concerning the RAIRS experiment. The infrared beam originating from the infrared source (S) is directed into the Michelson interferometer, consisting of a beamsplitter (B) and a fixed (M1) and moving cube corner mirror (M2). The beam is then directed out of the spectrometer by a parallel mirror (M3) into the compartment containing the RAIRS optics. The infrared beam is focused on to the sample at near grazing incidence by a parabolic mirror (M4). After reflection the beam is directly focused on the MCT detector (D) by a second parabolic mirror (M5). In the beam focusing on the sample a polarizer (P) is placed, allowing only the p-polarized component of the infrared light to be detected.

5.3.2 RAIRS instrumentation

The RAIRS experiments are performed in a separate cell, connected to the UHV chamber, allowing for both UHV and high pressure experiments. The RAIRS cell is optically interfaced (Figure 5.7) with a fourier transform infrared spectrometer (Galaxy 4020, Mattson). A flat mirror directs the infrared beam from the spectrometer, in the compartment containing the RAIRS optics. Both the spectrometer and optics compartment are separately flushed with dry nitrogen to reduce fluctuations in the spectra by absorption bands of atmospheric CO_2 and H_2O . The whole can be moved to and from the cell, for bakeout and maintenance purposes, on a high precision rail driven with compressed air. When the spectrometer is in the measuring position it is fixed by the compressed air, pressing the bench with the spectrometer and optics against two positioning buffers. In this position the box containing the optics makes a seal with the RAIRS cell with two O-rings on the differentially pumped flanges, supporting the KBr windows of the cell (Figure 5.8 and Figure 5.9). After cleaning the crystal in the main chamber, it is transported to the IR cell (Figure 5.9),

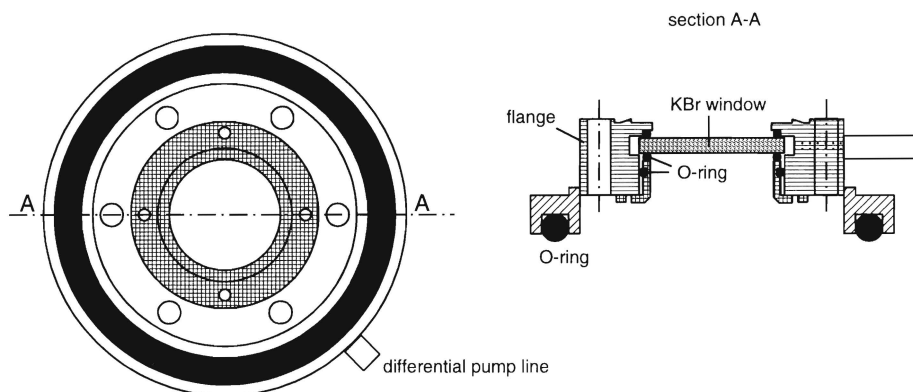


Figure 5.8

Flange supporting the infrared window. On the flange a ring is welded which supports the O-ring, providing the seal with the optics compartment. The KBr window is pressed into the UHV-flange between viton O-rings by a ring bolted on the UHV-flange. The flange is differentially pumped between the O-rings.

equipped with additional viewports to facilitate the sample transfer. Another advantage now is that the purge of the optics around the cell can be maintained during transfer, which allows for fast acquisition after cleaning. The cell (Figure 5.9) was constructed at the University workshop (CTD) from a massive steel block to be able to get a maximum inner space for optimal sample manipulation, and yet keep the outside dimensions as small as possible to minimize the optical path.

The infrared beam is generated by a high-intensity air cooled ICE source and focused to the KBr beamsplitter of the Michelson interferometer (Figure 5.7). The interferometer uses a fixed and a moving cube corner mirror, having the advantage that the beam reflected by the mirror is always parallel to the incoming beam. This enhances the stability of the instrument and eliminates spectral artifacts due to mirror tilt. A flat mirror directs the collimated beam of the interferometer on a parabolic mirror, which focuses the beam on the sample at a near grazing angle (85°) incidence, required for the RAIRS experiment [12]. The reflected beam is collected by a second parabolic mirror, that focuses the beam directly on the detector. We used a liquid nitrogen cooled narrow band mercury cadmium telluride (MCT) detector which allows the spectral range from 4000 to 800 cm^{-1} to be accessed. This detector was chosen, because it covers the spectral range in which most adsorbate molecules have their vibrational modes. In spite of the rather high cut-off frequency of 800 cm^{-1} , we chose for a narrow band MCT detector, because of its intrinsic high sensitivity with respect to the broad band MCT detector. The head of the detector goes through a seal in the top of

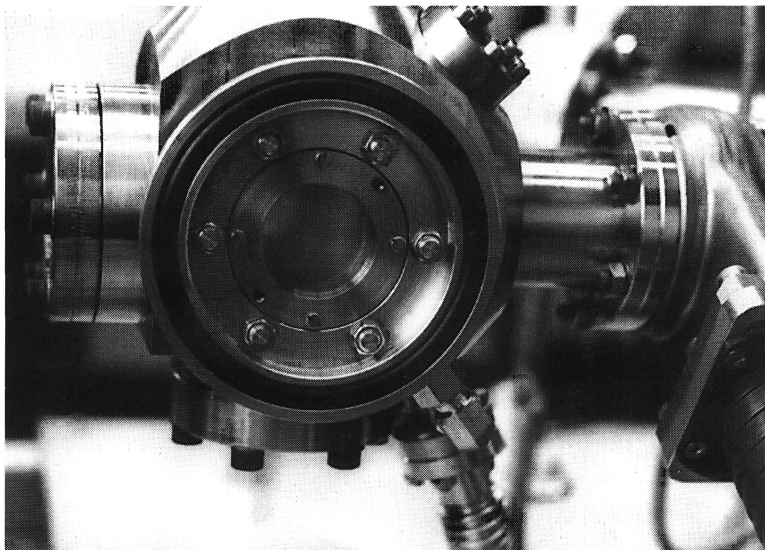


Figure 5.9
Photograph of the RAIRS cell.

the box providing the purge, to make filling of the detector with liquid nitrogen possible during acquisition, without the need to break the purge. In order to retain the optimum focusing characteristics of the mirrors around the RAIRS cell, the angle between the incoming and outgoing beam on the mirrors is kept at 90° . This is done by making an angle of 5° between the collimated beam, coming out of the spectrometer, and the long axis of the IR cell (Figure 5.7).

In the beam focusing on the sample, a KRS-5 wire grid polarizer is placed, allowing only the p -polarized component to be detected. The surface selection rule dictates that only the p -polarized component carries valuable information about the adsorbed layer. Filtering out the s -polarized component of the IR light enhances the signal to noise ratio and the intensity of the absorption bands [13].

The best resolution the spectrometer can achieve is 1 cm^{-1} , however, for RAIRS experiments this is satisfactory, since the intrinsic band width of adsorbed molecules is in the order of 5 cm^{-1} or higher.

5.3.3 LEED/AES optics

LEED and AES experiments are performed with a reverse view four grid AES/LEED optics (Spectaleed, Omicron Vakuumphysik GmbH). The optics are retractable, using an in vacuum gearing mechanism, allowing easy access to the sample for manipulation purposes.

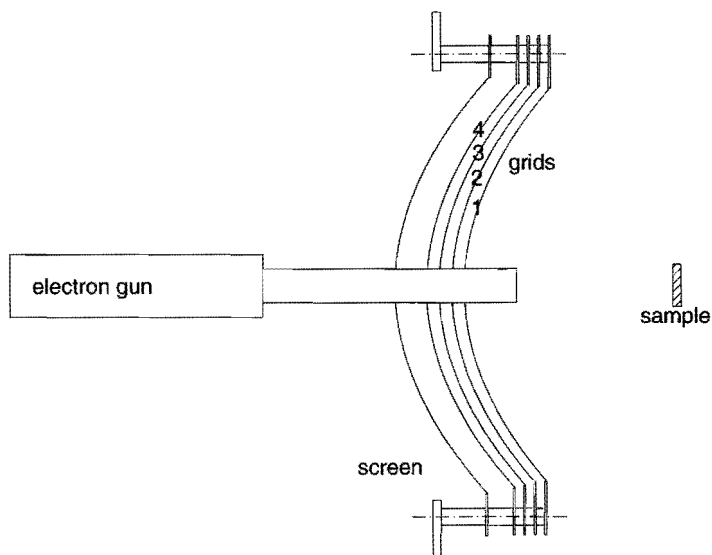


Figure 5.10

Drawing of the AES/LEED optics, showing the electron gun and the configuration of the grids with respect to the sample.

The advantage of the rear view LEED is that the screen is not obscured by the sample manipulator. The integral electron gun in the optics can be used for both LEED and AES measurements, which makes that there is no additional electron gun needed for AES. The electron gun makes use of a lanthanum-hexaboride filament, which provides a stable electron emission current.

In the LEED experiment the sample is positioned in the centre of the set of concentric grids of the optics. The grid nearest to the sample (grid 1 in Figure 5.10) is set at the same potential (ground) as the sample, to ensure that electrons reflecting from the sample travel in a field free space to the grids and so maintain their radial geometry. The next grids (grid 2 and 3 in Figure 5.10) are then set at a potential (suppressor potential) slightly less than that of the electron gun filament, to allow only the elastically scattered electrons to be accelerated to the fluorescent screen. The inelastic scattered electrons are retarded by the grids and do not pass to the screen. The fourth grid is grounded, reducing field penetration of the suppressor grids by the screen voltage.

For an AES experiment the potential of the retarding grids (grid 2 and 3) is scanned over the spectral range of interest. The grid nearest to the sample is again grounded and the fluorescent screen is in this case used as a current collector. Now all electrons, coming from the sample, with a kinetic energy higher than the energy corresponding to the potential of the retarding grids, will reach the screen and contribute to the measured current. Thus if the energy distribution of the electrons coming from the sample is $N(E)$, the retarding potential

is V_r , corresponding to a minimum pass energy of $E_p = eV_r$, and the energy of the primary electron beam is E_b , then the current measured with the collector is:

$$\int_{E_p}^{E_b} N(E) dE \quad (5.9)$$

Differentiating this current will result in a signal with the desired energy distribution $N(E)$. This can be achieved by modulating [14] the retarding voltage with a signal $V_m \sin \omega t$. Now the current arriving at the collector can, by a Taylor series expansion, be expressed as a sum of harmonics. The amplitude of the fundamental is:

$$A_1 = V_m N(E_p) + \frac{V_m^3}{8} N''(E_p) + \dots \quad (5.10)$$

The amplitude of the second harmonic is:

$$A_2 = \frac{V_m^2}{4} N'(E_p) + \frac{V_m^4}{48} N'''(E_p) + \dots \quad (5.11)$$

Here $N'(E)$, $N''(E)$ and $N'''(E)$ are the first, second and third order differential of the energy distribution. Provided that the modulation amplitude V_m is small, the higher order terms can be neglected, and the amplitude of the first harmonic is proportional to $V_m N(E_p)$. Thus measuring the current with this signal modulation gives the desired signal $N(E)$. Since the signal of interest in $N(E)$ is often weak due to a large background, in practice the differential of the energy distribution $N'(E)$ is measured. Differentiation removes the constant background and allows increased amplification of the signal. The differential signal $N'(E)$ is obtained by measuring the second harmonic as a function of the retardation voltage. The amplitudes of the harmonics can be measured with a phase sensitive detector, like a lock-in amplifier. To obtain the second harmonic, the signal channel of the lock-in amplifier (Stanford Research Inc.) is tuned to a frequency, double that of the modulation signal applied to the retarding grids. This double frequency is also applied to the reference channel of the lock-in amplifier.

Since the retarding grids and the collector form a hemispherical capacitor, there is substantial capacitive coupling between them. The fourth grounded grid, between the retarding grids and the collector, reduces this effect. Further, the capacitive cross-talk is compensated by a link between the modulator circuit and the preamplifier processing the measured collector signal.

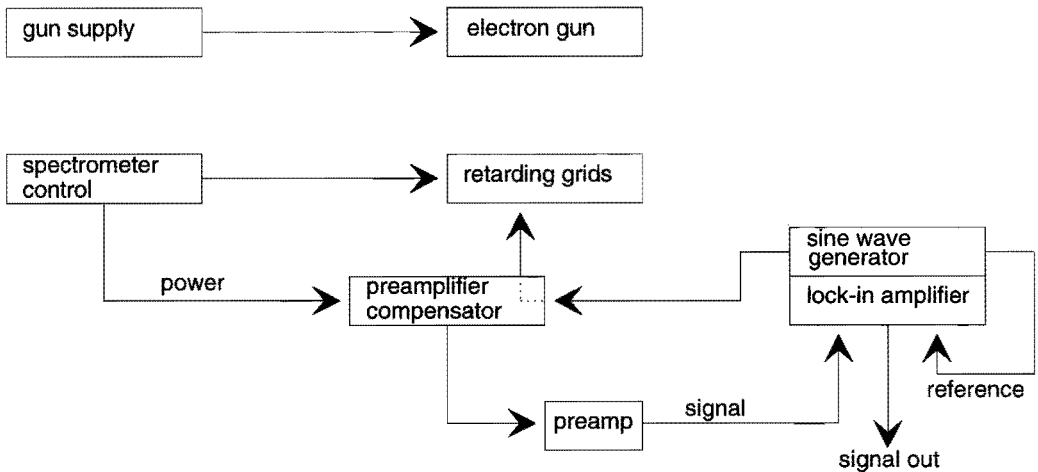


Figure 5.11

Diagram of the signal channels needed for the AES experiment.

A diagram of the AES setup is shown in Figure 5.11. The gun supply controls the energy and current of the primary electron beam, with a maximum beam energy of 3.5 keV. The spectrometer control unit applies the retardation voltage to the grids and supplies the power for the matching unit, containing the preamplifier and compensator circuitry. In the sine wave generator of the lock-in amplifier, the modulation signal is produced, which is applied to the retarding grids and the reference channel of the lock-in amplifier. The compensated and preamplified signal is connected to the input channel of the lock-in amplifier, in which the second harmonic of the signal is detected. The lock-in amplifier output can be accessed by a pen-recorder or a PC. With a specially developed computer program the lock-in amplifier can be completely controlled from the computer. In such a way AES data can be stored and processed afterwards. The retardation voltage and scan rate can also be controlled by the computer.

5.3.4 Mass spectrometer

The mass spectrometer (Quadrupac Q100, Leybold-Heraeus GmbH) used for residual gas and TDS analysis is a quadrupole mass spectrometer with a mass range of 100 mass units

and a multiplier sensing head, able to detect partial pressures of 1×10^{-13} mbar. The ionization head is positioned close (± 15 mm) to the sample, and the latter can be moved with the surface normal directed to the mass spectrometer, for accurate TDS measurements. The mass spectrometer can be controlled by a PC, using a specially developed computer program and a communication board (Labtender). This configuration allows for easy acquisition of mass and TDS spectra, which can be stored for further data processing. In the TDS mode, eight different masses can be accessed simultaneously, together with the temperature of the sample.

In order to perform accurate and reproducible gas exposures, the pressure gauge can be read by the program as well. The background pressure is determined and subtracted from the dosing pressure, which is measured as a function of time. From the integrated pressure-time function the actual exposure is calculated.

5.3.5 Sample manipulation

In order to perform experiments in two different chambers, a sample transfer mechanism is needed, allowing sample transportation without breaking the vacuum. Since the RAIRS cell and UHV chamber are situated next to each other, a horizontal transportation is required. We have chosen for a configuration with two manipulators and a separate transfer rod, instead of one horizontal manipulator, which would not have enough stability over the required length.

The criteria for the sample transfer mechanism are the following:

- The crystal has to be heated and cooled, implying that a good thermal contact with the manipulator is necessary and that electrical contacts for heating purposes have to be able to be made and broken in a reliable way.
- The sample temperature has to be monitored by a thermocouple, which has a good thermal contact with the sample.
- The sample holder has to be designed in such a way that it is able to travel through a 38 mm tube, and that the sample can be mounted proud of the holder so that the infrared beam is unobstructed.
- The sample has to be insulated from ground to be able to measure ion and electron beam currents.
- The transfer has to be smooth without significant rise of the pressure.

The transfer and sample holder design described here is based on the system reported by Raval et al. [11], in which the sample is mounted on a stainless steel ring, which is composed of four electrically insulated ring segments. Two of those segments are used for sample heating and the other two for temperature measurement. The sample ring is supported by a ring holder mounted on the manipulator, containing spring contacts to provide the connections to the heating and thermocouple segments. The ring holder is mounted on a copper block, clamped around the cold finger of the manipulator. This system, however, still

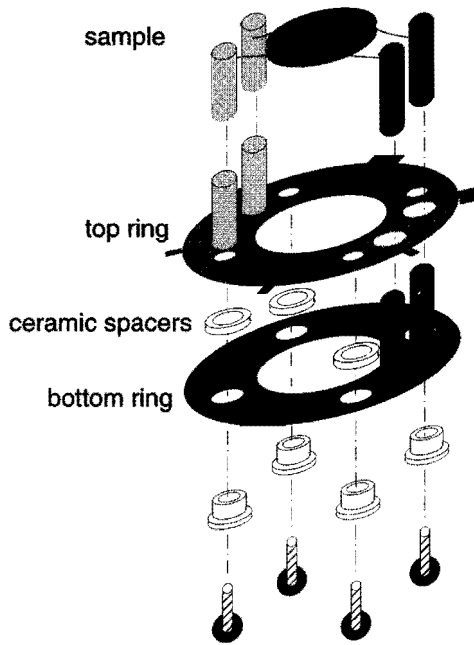


Figure 5.12

Drawing of the segments of the sample holder. The crystal is clamped between tantalum wires that are attached to supporting posts, two on each ring. The rings are electrically insulated from each other.

has some serious limitations. Firstly, the electrical contacts to be made by the springs on the ring holder, proved to be not very reliable, since the springs lose their elasticity during use. Secondly, the thermal contact to the cold finger was not sufficient. Although the system was designed to achieve temperatures of 100 K, the ultimate temperature did not go below 170 K. Thirdly, the temperature measurement appeared to be not very accurate, caused by the contacts that had to be made by the springs. Since these contacts formed a junction in the thermocouple circuit, the measured temperature would only be reliable if those junctions have exactly the same temperature, which is very hard to achieve.

Considering the above a new sample holder ring, together with a new ring holder was designed and constructed at the University workshop (CTD). This sample ring holder consists (Figure 5.12) of two tantalum rings, separated by ceramic spacers, each fitted with two posts to support the heating wires. The single crystal is resistively heated by two tantalum support wires of 0.25 mm diameter. The crystal is clamped between the tantalum supports, that are pressed in spark eroded slots at the sides of the crystal. This provides a rigid fixation of the crystal and good thermal contact. The top ring of the sample holder provides one electrical contact for heating, directly to the sample ring holder mounted on the manipulator. The bottom ring makes contact with four U-shaped springs, mounted electrically insulated on the ring holder on the manipulator, providing the other electrical contact. These springs consist of an inconel foil, providing a good and stable contact, since inconel is a very elastic material, even at high temperatures. This setup is very reliable, because the contact is made

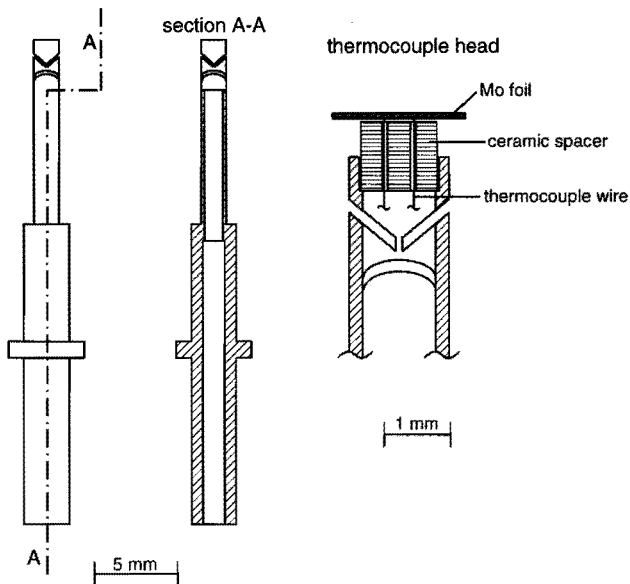


Figure 5.13

The thermocouple is supported by a thin steel tube with a flexible head, that is pressed at the back of the crystal by a spring.

with four springs, meaning that there is always electrical contact, even if some springs malfunction. Another advantage is that the thermal contact is improved in this way, temperatures of 140 K can now be achieved.

The temperature is monitored by a chromel-alumel thermocouple. The thermocouple is pressed at the back of the crystal by a spring assembly, mounted at the centre of the sample ring holder. A drawing of this thermocouple system is shown in Figure 5.13. The thermocouple junction is spot welded on a thin molybdenum foil of 2 mm^2 and $200 \mu\text{m}$ thick, that ensures a good thermal contact with the back of the crystal. The foil and thermocouple wires are supported by a ceramic spacer, fitted on the steel thermocouple housing. This ceramic spacer ensures a good electric and thermal insulation from the steel house. In the house the thermocouple wires are insulated by a glass thimble. The head of the thermocouple support is provided with spark eroded slots, which make the head flexible. Now the head will align itself with the foil flat against the crystal during sample handling. Another advantage is that the thermal conductivity from the head of the thermocouple support to the rest of the manipulator is minimal. This is also provided by the use of very thin ($50 \mu\text{m}$) thermocouple wires. This is important for a correct measurement of the temperature, since when the thermocouple would be cooled strongly the measured temperature would be too low. The steel house supporting the thermocouple is fitted on the

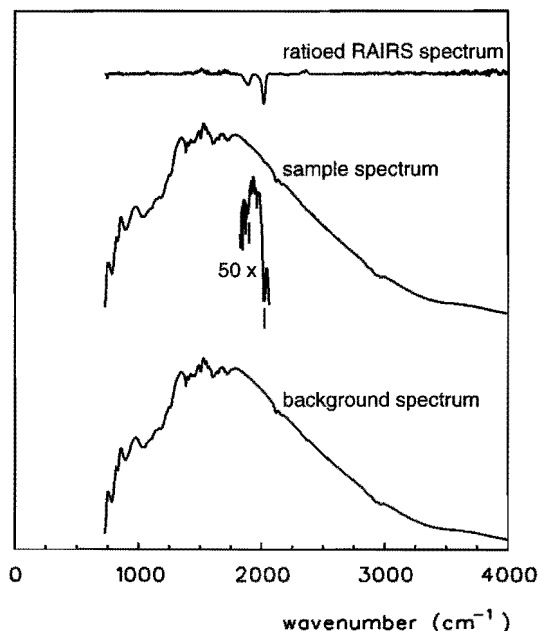


Figure 5.14

In a typical RAIRS experiment first a background spectrum is taken of the clean sample. The sample spectrum is then ratioed to the background spectrum and the actual RAIRS spectrum is obtained. Since the signals of an adsorbate are very small, they can only clearly be distinguished after ratioing the spectra. The lines denote the peak positions in the sample spectrum, revealing that the peaks are hardly visible even after a 50 times magnification.

manipulator and as a whole pressed against the sample by an inconel spring. The advantage of this configuration is that no junctions in the thermocouple wires have to be made and broken, which can cause erroneous temperature readouts.

5.4 RAIRS on miscellaneous adsorbate systems

In this section we will briefly discuss some adsorbate systems studied with RAIRS. These studies were carried out in order to investigate the abilities of the instrument and are only meant to be illustrative for the performance of the apparatus.

A RAIRS spectrum is measured as follows. First a background spectrum is measured from a clean sample, then a sample spectrum is recorded of an adsorbed species on the sample. Afterwards the sample spectrum is ratioed to the background spectrum and the actual RAIRS spectrum is obtained. This is because the signals of an adsorbed monolayer or less in the

infrared spectrum are very small. Figure 5.14 shows a background and a sample spectrum typically obtained in a RAIRS experiment. The difference between the two is very small, even magnifying the sample spectrum 50 times hardly reveals any signal of the adsorbed species. However, when the spectra are ratioed to each other a RAIRS spectrum is obtained with very distinct absorption bands.

5.4.1 Adsorption of CO on Rh(100) at high pressure

Since infrared radiation has a long travelling path in gaseous atmospheres, RAIRS can be applied at relatively high pressures, compared to those required for most other surface sensitive spectroscopies. Although most gases are strong absorbers of infrared light, giving rise to intense absorption bands in the RAIRS spectrum, we will show that spectra taken at high ambient gas pressures yield valuable information about the adsorbate.

Figure 5.15 shows the RAIRS spectra of CO adsorbed on Rh(100) at 300 K, obtained at several CO pressures. The spectra were taken at an instrumental resolution of 4 cm^{-1} . First a background spectrum was measured of the clean Rh(100) surface by adding 1000 scans. The sample spectra were obtained by adding 400 scans and ratioing to the background spectrum.

The spectrum obtained at 1×10^{-6} mbar CO (Figure 5.15) is typical for 0.75 monolayer of CO adsorbed on Rh(100) at 300 K (see Chapter 6 for further detail). The two peaks at 1937 and 2067 cm^{-1} can be assigned to bridged and linear bonded CO respectively. Exposing the crystal to 5×10^{-3} mbar CO causes the linear CO band to increase and shift to higher frequency, resulting in a sharp intense band at 2083 cm^{-1} . Concomitantly the bridged CO band has almost disappeared, only a broad weak feature around 1900 cm^{-1} remains. In this spectrum (Figure 5.15) the P and Q-branch of the CO gas phase spectrum are clearly visible between 2000 and 2250 cm^{-1} . The band of the adsorbed CO species is still large compared to the gas phase spectrum. The band of the linear adsorbed CO appears as a large peak on the P-branch of the CO gas phase spectrum. At a CO pressure of 150 mbar the spectrum (Figure 5.15) is dominated by an intense absorption band of gaseous CO. Absorption bands due to the adsorbed CO species are visible as small shoulders on the low frequency side of the P-branch of the gaseous CO spectrum. The linear peak as observed at 5×10^{-3} mbar can still clearly be distinguished at 2085 cm^{-1} . Additionally two other absorption bands are observed at 2035 and 2067 cm^{-1} , which become more clear in the deconvoluted spectrum (the dashed spectrum in Figure 5.15). These absorption bands can be assigned to a rhodium dicarbonyl species, as was also observed by Corey et al. [15] with infrared measurements on a $\text{Rh}_6(\text{CO})_{16}$ compound. Corey et al. found two absorption bands for the $\text{Rh}(\text{CO})_2$ fragment at 2073 and 2026 cm^{-1} , which were respectively assigned to the symmetric and antisymmetric mode.

Figure 5.15 shows that RAIRS spectra can be readily obtained at relative high ambient

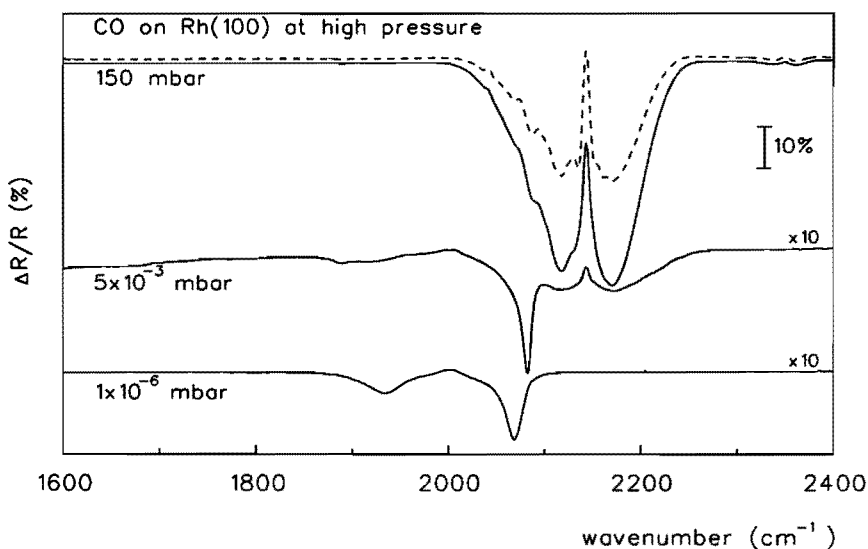


Figure 5.15

RAIRS spectra of CO adsorbed on Rh(100) at 300 K, for several CO pressures. The spectrum obtained at 150 mbar is plotted together with the deconvoluted spectrum (dashed), showing more clearly the peaks of the adsorbate species on the large gas phase background. The spectra obtained at 1×10^{-6} and 5×10^{-3} mbar have been magnified by a factor of 10 relative to the spectrum obtained at 150 mbar.

gas pressures. Although the spectra show a large contribution of gas phase absorption bands, absorption bands originating from adsorbed species can still clearly be distinguished.

5.4.2 Adsorption and desorption of NO on Rh(100) with coadsorbed CO

The frequency of infrared absorption bands in RAIRS yields information about the adsorbed species, the adsorption site and interactions between adsorbates. Here we will demonstrate this for the coadsorption of NO and CO on Rh(100) at 300 K.

Figure 5.16 shows the RAIRS spectra obtained after exposing the clean Rh(100) surface to various amounts of NO at 300 K. The spectra were taken at an instrumental resolution of 4 cm^{-1} and by adding 400 scans and then ratioing to a previously stored background spectrum. Together with the NO some CO was admitted in the vacuum chamber, the ratio of NO to CO was approximately 2:1. Figure 5.16 also shows some RAIRS spectra obtained during desorption of the NO saturated surface. These spectra were taken by adding 10 sample scans in an acquisition time of about 2 seconds per spectrum.

After low exposures the spectra reveal two infrared absorption bands at 1890 and

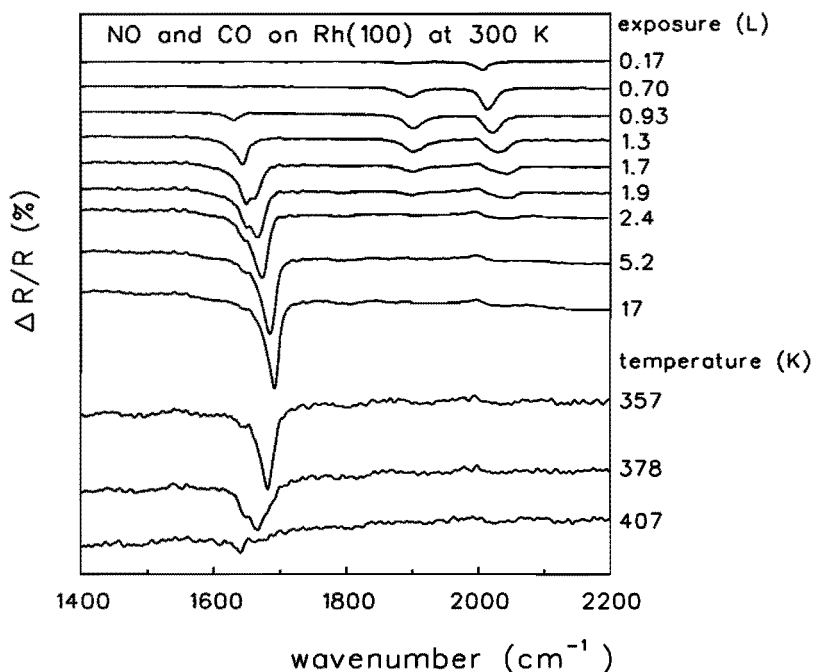


Figure 5.16

RAIRS spectra of the coadsorption of NO and CO on Rh(100) at 300 K.

2010 cm^{-1} , indicating a bridged and linear bonded CO molecule (see Chapter 6). Absorption bands attributed to adsorbed NO are not observed at these low exposures due to dissociation of the NO molecules. As the surface gets increasingly occupied with N and O-adatoms, sites needed for dissociation are blocked and at an exposure of 0.93 L ($1 \text{ L} = 1 \times 10^{-6} \text{ Torr.s}$) an NO absorption band appears at 1630 cm^{-1} . With increasing exposure this band shifts up in frequency to 1649 cm^{-1} and the peaks assigned to adsorbed CO decrease in intensity, indicating that CO is displaced from the surface by NO. According to Root et al. [16] and Villarrubia et al. [17], the NO species at this frequency can be assigned to twofold bridge bonded NO.

At 1.7 L exposure a shoulder appears on the high frequency side of the NO peak, which gains in intensity with increasing exposure. This second peak shifts up in frequency from 1659 to 1692 cm^{-1} as the intensity increases, meanwhile the low frequency peak loses intensity. This shift in frequency can be attributed to dipole coupling interactions of the adsorbed NO molecules.

Upon desorption the high frequency peak decreases in intensity and shifts to lower frequency. At 378 K there is a clear shoulder at 1649 cm^{-1} , which increasingly dominates the

spectrum as desorption proceeds. At 407 K this band has become a small peak at 1640 cm^{-1} .

A possible explanation for the observation of two types of NO might be the formation of islands of adsorbed NO molecules. At low coverage we might speak of more or less isolated adsorbed NO molecules, resulting in the low frequency peak. As the coverage increases and islands are formed, two types of NO molecules exist on the surface; molecules on the edge of the islands and molecules in the islands. The latter will exhibit a higher vibrational frequency due to stronger dipole interactions than the molecules at the edge of the islands. Another explanation could be that the NO molecules first occupy sites near defects in the surface, resulting in a slightly modified NO stretching frequency [18]. This would, however, imply a rather high density of defects, which is not very likely.

The experiments discussed illustrate that RAIRS yields information about the type of adsorbate present on the surface and the geometry in which the molecules are adsorbed. The spectra also reveal information about the vicinity (e.g. islands or defects) of the adsorption site.

5.4.3 Adsorption of ethylene and acetonitrile on Rh(100)

In order to be able to measure RAIRS spectra of weak infrared absorbers, like hydrocarbons, a low noise level in the RAIRS spectra is required. Spectra of adsorbed ethylene and acetonitrile show that the apparatus performs very well.

Figure 5.17 shows the RAIRS spectra of ethylene and acetonitrile adsorbed on Rh(100) at 200 K. First a background spectrum of 1000 scans at an instrumental resolution of 4 cm^{-1} was recorded. The sample spectra were taken by adding 1000 scans (5 minutes) for the ethylene and 400 scans (2 minutes) for the acetonitrile spectra and then ratioing to the previously recorded background spectrum. Whereas in the case of CO and NO absorption bands of a few percent were observed, now the absorption bands are only a few hundredths of a percent. Thus the signals are almost two orders of magnitude lower in intensity. The noise level of the acetonitrile spectrum is about 0.015 %, allowing peaks of 0.03 % absorption intensity to be detected.

The RAIRS spectrum of the adsorbed ethylene shows three absorption bands (1343 , 2882 and 2924 cm^{-1}) that can be assigned to adsorbed ethylene. The spectral features in the range from 1400 to 1700 cm^{-1} are due to fluctuations in the water content of the purged optics compartment. During cooling and exposure to ethylene some CO coadsorbed on the surface, resulting in the peaks at 1848 and 2006 cm^{-1} . The peak at 2006 cm^{-1} points in the opposite direction of the other peaks for the following reason. When the background spectrum was recorded some CO was already present on the surface. Adsorption of ethylene causes the CO to shift from linear to bridged bonded, with the result that the sample spectrum as shown in Figure 5.17 contains less linear bonded CO than the background spectrum, resulting in the upwards absorption peak. The peak at 1848 cm^{-1} is assigned to bridged bonded CO. The

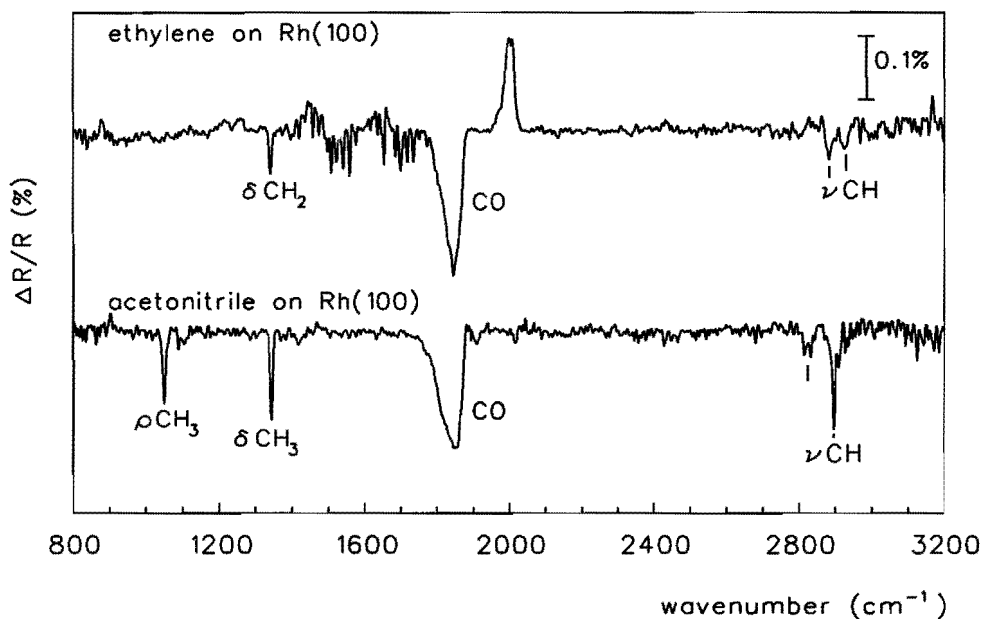


Figure 5.17
RAIRS spectra of ethylene (top) and acetonitrile (bottom) adsorbed on Rh(100) at 200 K.

absorption bands originating from the ethylene can be assigned to a CH_2 deformation mode (1343 cm^{-1}) and CH stretch vibrations (2882 and 2924 cm^{-1}), suggesting that the ethylene molecule is bonded to the surface with the $C=C$ double bond. In this case the $C=C$ bond is parallel to the surface and no absorption band is observed in RAIRS due to the dipole selection rule.

Adsorption of acetonitrile yields the lower spectrum of Figure 5.17. Again an absorption band due to bridged bonded CO is observed, caused by the coadsorption of CO during the exposure to acetonitrile. The peaks of the adsorbed acetonitrile can be assigned to a CH_3 rocking (1049 cm^{-1}) and deformation (1345 cm^{-1}) mode and to CH stretch vibrations (2825 and 2897 cm^{-1}), as was also observed by Erley [19] for the adsorption of acetonitrile on Cu(111). However, on the rhodium surface no CN stretching modes are observed. This suggests that the molecule is bound with the CN bond parallel to the surface.

5.5 Conclusions

A new instrument to perform RAIRS on metal single crystals has been developed and built. RAIRS can be performed under UHV and under atmospheric conditions. The apparatus

contains also LEED, AES and TDS facilities as supporting techniques.

Preliminary experiments on the adsorption of CO, NO, C₂H₄ and CH₃CN have shown that the apparatus performs very well. The CO adsorption experiments at high pressure showed that at high ambient gas pressures meaningful spectra can be measured. From the adsorption and desorption experiments of NO appeared that the resolution is excellent, species close in frequency can readily be distinguished, and that relatively fast processes like desorption can be followed. The apparatus is also very sensitive as was shown by the spectra of ethylene and acetonitrile, of which good spectra could be recorded in a reasonable acquisition time.

References

- [1] F.M. Hoffmann, Surf. Sci. Rep. **3**, 107 (1983).
- [2] Y.J. Chabal, Surf. Sci. Rep. **8**, 211 (1988).
- [3] M.A. van Hove, W.H. Weinberg and C.-M. Chan, *Low-Energy Electron Diffraction*, Springer series in surface science, G. Ertl and R. Gomer, series Eds.; Springer-Verlag, Berlin, 1986.
- [4] G. Ertl and J. Küppers, *Low energy electrons and surface chemistry*, 2nd ed., VCH, Weinheim, 1985.
- [5] P.A. Redhead, Vacuum **12**, 203 (1962).
- [6] D.A. King, Surf. Sci. **47**, 384 (1975).
- [7] J.L. Falconer and R.J. Madix, J. Catal. **48**, 262 (1977).
- [8] E. Habenschaden and J. Küppers, Surf. Sci. **138**, L147 (1984).
- [9] C.-M. Chan, R. Aris and W.H. Weinberg, Appl. Surf. Sci. **1**, 360 (1978).
- [10] A.M. de Jong and J.W. Niemantsverdriet, Surf. Sci. **233**, 355 (1990).
- [11] R. Raval, M.A. Harrison and D.A. King, J. Vac. Sci. Technol. A **9**, 345 (1991).
- [12] R.G. Greenler, J. Chem. Phys. **44**, 310 (1966).
- [13] Y.P. Song, M.C. Petty and J. Yarwood, Vibrational Spectr. **1**, 305 (1991).
- [14] N.J. Taylor, Rev. Sci. Instr. **40**, 792 (1969).
- [15] E.R. Corey, L.F. Dahl and W. Beck, J. Am. Chem. Soc. **85**, 1202 (1963).
- [16] T.W. Root, G.B. Fisher and L.D. Schmidt, J. Phys. Chem. **85**, 4679 (1986).
- [17] J.S. Villarrubia and W. Ho, J. Phys. Chem. **87**, 750 (1987).
- [18] W. Erley, Surf. Sci. **205**, L771 (1988).
- [19] W. Erley, J. Elec. Spectr. Rel. Fenom. **44**, 65 (1987).

6 Adsorption of CO on Rh(100) studied with reflection absorption infrared spectroscopy*

Abstract

The interaction of CO with a Rh(100) surface has been investigated as a function of temperature and CO pressure, with reflection absorption infrared spectroscopy (RAIRS), low energy electron diffraction (LEED) and thermal desorption spectroscopy (TDS). At low coverages CO adsorbs predominantly in a linear adsorption geometry, up to 0.5 monolayers (ML), where a $c(2 \times 2)$ LEED pattern is observed. At 300 K, a saturation coverage of 0.75 ML is reached. At this stage a $p(4\sqrt{2} \times \sqrt{2})R45^\circ$ LEED pattern is observed, and in combination with RAIRS data it appears that the number of CO molecules adsorbed in linear sites is about equal to the number of CO in bridged sites. At temperatures well below 300 K and relatively high CO exposures at pressures of 5×10^{-7} mbar and higher, CO is compressed into a dense hexagonal overlayer structure with a $c(6 \times 2)$ LEED pattern. In this overlayer CO occupies mainly linear adsorption sites. The results presented in this chapter are compared with previously reported results in the literature, which showed some serious inconsistencies.

6.1 Introduction

Reflection absorption infrared spectroscopy (RAIRS) is a very suitable technique to study adsorption and interactions of adsorbed species on metal surfaces. The frequency, intensity and line shape, of the vibrational bands of adsorbates, provide information about the adsorption states, lateral interactions and ordering of the adlayer, as function of the coverage. Moreover, RAIRS is applicable under ultrahigh vacuum as well as under higher pressure conditions (up to 1 atmosphere in our apparatus), which in principle makes it possible to relate surface science studies to catalytic processes at atmospheric conditions.

In the literature several reports have appeared on the adsorption of CO on a rhodium (100) surface. However, there is still some disagreement about the site occupation and surface structure of the adsorbed CO. In this chapter we present results from RAIRS, LEED and TDS experiments over a wide range of exposures, and we will compare these with the results in the literature. We propose a picture for the adsorption of CO, which explains most of the previously reported results.

* The content of this chapter is submitted for publication to the Journal of Chemical Physics.

In 1966 C.W. Tucker [1] reported the first LEED study on the adsorption of CO on Rh(100). CO was adsorbed at room temperature at a pressure of about 2×10^{-6} Torr. With hindsight, the observed diffraction pattern corresponds to a $p(4\sqrt{2} \times \sqrt{2})R45^\circ$ LEED structure, as proposed later by Gurney et al. [2]. Tucker [1] proposed a coincidence lattice model corresponding to a coverage of 0.75 ML (1 ML = 1 adsorbate atom or molecule per surface rhodium atom, i.e. $1 \text{ ML} = 1.39 \times 10^{15} \text{ atoms/cm}^2$). Tucker [1] also observed that part of the CO was removed by heating the crystal to 333 K.

Castner et al. [3] showed that upon CO adsorption first a $c(2 \times 2)$ structure is formed up to coverages of 0.5 ML. At higher CO exposures the $c(2 \times 2)$ structure compresses into a hexagonal overlayer to give a "split" (2×1) pattern with a coverage of 0.83 ML. The compressed overlayer structures could only be observed at temperatures well below room temperature and at high CO partial pressures of 1×10^{-6} Torr.

Kim et al. [4] adsorbed CO on Rh(100) at 100 K. LEED experiments showed that CO first adsorbs in a $c(2 \times 2)$ structure at 0.5 ML coverage. At higher exposures a pattern similar to the coincidence lattice pattern reported by Tucker [1] was observed. TDS results showed a single CO desorption peak at low coverages, while at higher coverages a shoulder develops at the low temperature side. The growth of this shoulder is consistent with the development of the compression state observed with LEED. Based on the LEED patterns, the authors estimated an exposure at which the $c(2 \times 2)$ pattern was completed. From this calibration a saturation coverage of 0.6 ML was calculated.

Richter et al. [5] and Gurney et al. [2] reported results of the adsorption of CO on Rh(100) at 100 K, obtained with TDS, LEED and electron energy loss spectroscopy (EELS). TDS spectra of a saturated surface showed three desorption states. These authors determined that the saturation coverage is equivalent to 0.75 ML, according to a calibration based on LEED and TDS results from CO and H_2 coadsorption experiments. At 0.5 ML coverage, CO is predominantly linear bonded to the rhodium atoms and a $c(2 \times 2)$ LEED pattern is observed. At higher coverages bridge sites are increasingly occupied, until at saturation coverage a $p(4\sqrt{2} \times \sqrt{2})R45^\circ$ LEED pattern is observed.

A RAIRS study of the CO adsorption on Rh(100) at 90 and 300 K was reported by Leung et al. [6]. This work disagrees with the previous EELS studies [2,5], in that at all coverages CO is seen to adsorb in linear and a considerable amount of bridge sites, for both adsorption temperatures. For adsorption at 300 K, the authors reported the formation of an ordered CO overlayer at 0.4 ML coverage. A saturation coverage of 0.6 ML was estimated from TDS experiments. For adsorption at 90 K a highly ordered CO adlayer was found at 0.5 ML, corresponding to a $c(2 \times 2)$ LEED pattern. RAIRS data indicated that the CO adlayer undergoes a phase transition with increasing coverage from 0.5 ML to 0.75 ML at saturation coverage, where a $p(4\sqrt{2} \times \sqrt{2})R45^\circ$ LEED pattern is observed.

Comparison between the studies is difficult, because of the different conditions used. Our results, obtained at a range of temperatures and exposures, reconcile the work of Tucker [1], Castner et al. [3], Kim et al. [4] and Ho and coworkers [2,5], but do not confirm all the

results reported by Leung et al. [6], which, as we discuss later on, suffer from the presence of impurities on the Rh(100) surface.

6.2 Experimental

6.2.1 Apparatus

The apparatus used for the experiments reported here, has been described in detail in Chapter 5. Here we summarize the most important aspects. Figure 6.1 shows a schematic drawing of the system. It consists of an ultrahigh vacuum (UHV) chamber and a separate cell to perform RAIRS. The sample is transferred between the two by a magnetically driven transfer rod. In the main chamber the single crystal sample can be cleaned and characterized by LEED, Auger electron spectroscopy (AES) and TDS. LEED and AES experiments are performed with a reverse view, four grid AES/LEED optics (Spectaleed, Omicron Vakuumphysik GmbH). The mass spectrometer (Quadrupac Q100, Leybold-Heraeus GmbH) used for TDS analysis is a quadrupole mass spectrometer with a mass range of 100 mass units and a multiplier sensing head. An argon ion gun (AS-10, VSW) is used for sputter cleaning. The system is pumped by a 360 l/s turbomolecular pump and a water-cooled titanium sublimation pump (Leybold). The pressure is monitored by a Bayard-Alpert nude ionization gauge (IG-3, Inficon). The base pressure after bakeout is typically 2×10^{-10} mbar.

The RAIRS cell has two KBr windows mounted in differentially pumped holders. The cell can be isolated from the main chamber by a gate valve (VAT) to allow high pressure experiments (up to 1 bar) and can be separately pumped by a 150 l/s turbo molecular pump. Both the UHV chamber and the RAIRS cell are fitted with vertically mounted $xyz\theta$ manipulators with differentially pumped rotary feedthroughs and liquid nitrogen cold fingers. The sample manipulation system is based on that published by Raval et al. [7]. The single crystal is resistively heated by two tantalum support wires of 0.25 mm diameter, pressed in slots at the sides of the crystal. The temperature is monitored with a chromel-alumel thermocouple. This configuration allows cooling to 140 K and heating to 1300 K.

The RAIRS cell is optically interfaced (Figure 6.1) with a fourier-transform infrared spectrometer (Galaxy 4020, Mattson) such, that the infrared beam undergoes a single reflection from the crystal surface at near grazing incidence (85°), required for the RAIRS experiment [8]. A KRS-5 wire grid polarizer (P) is placed in the beam, focused on the sample by a parabolic mirror (M1), and allows only the p -polarized component to be detected. The surface dipole selection rule dictates that only the p -polarized component carries valuable information about the adsorbed layer. Filtering out the s -polarized component of the IR light thus enhances the signal to noise ratio. The reflected beam is collected by a second parabolic mirror (M2), that focuses the beam directly on to the detector (D). We use a liquid nitrogen cooled narrow band mercury cadmium telluride (MCT)

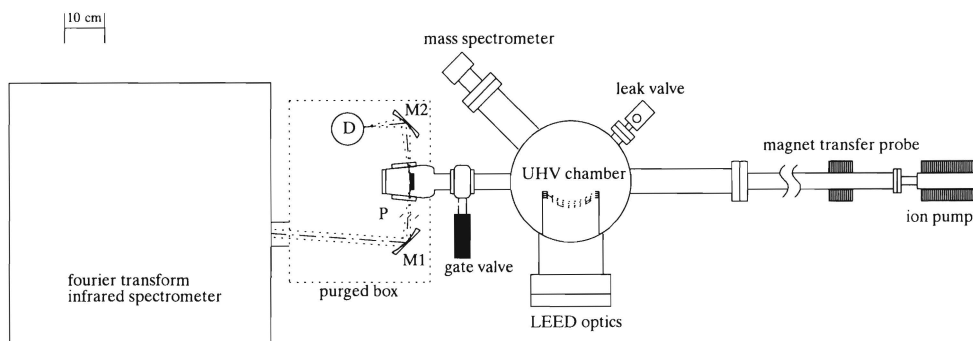


Figure 6.1

Schematic drawing of the RAIRS apparatus, showing the UHV chamber and the RAIRS cell and optics. The parabolic mirror M1 focuses the infrared beam on the sample, through a KRS-5 wire grid polarizer (P). The reflected beam is collected by a parabolic mirror M2, which focuses the beam directly on the MCT detector (D).

detector, which allows the spectral range from 4000 to 800 cm^{-1} to be accessed. The entire optical path outside the UHV is flushed with dry nitrogen to reduce fluctuations in the spectra by absorption bands of atmospheric CO_2 and H_2O .

6.2.2 Sample preparation and experimental conditions

The crystal was initially cleaned by extensive heating in 2×10^{-7} mbar oxygen at 870 K to remove carbon contaminations. Phosphor, sulfur, boron and chlorine contaminations were eliminated by sputter/anneal cycles till these contaminants depleted from the surface region. Sputtering was done with 500 eV Ar^+ ions. Routinely the crystal was cleaned by two cycles of sputtering for 20 minutes, followed by flashing to 1100 K . Then the sample was heated at 870 K in 2×10^{-7} mbar oxygen for 20 minutes and flashed to 1200 K . After this cleaning procedure, Auger spectra did not show any contamination. The surface structure was checked with LEED, which showed a sharp $p(1 \times 1)$ pattern. The shape and position of CO desorption peaks were also used to check the surface cleanliness, since CO desorption is more sensitive to low concentrations of surface contaminants than AES (see below).

Auger spectra were taken with a four grid retarding field analyzer (RFA), coupled to a lock-in amplifier (SR-510, Stanford Research Inc.). The primary electron beam had an energy of 3 keV and a beam current of $15\text{ }\mu\text{A}$. The signal was modulated at 2 kHz with an amplitude of 1 V .

LEED data were obtained with an electron beam current between 10 and $20\text{ }\mu\text{A}$. Photographs were made with a 3200 ASA film and $1/8$ or $1/15$ second exposure time. After

each high pressure exposure the gas phase was pumped off before the LEED experiments were carried out.

Thermal desorption spectra were recorded by linearly ramping the crystal temperature at a rate of 3.5 K/s. The normal of the crystal surface was directed to the mass spectrometer during the TDS experiments. Gas exposures were made by backfilling the chamber with a leakvalve up to pressures of 1×10^{-8} mbar, unless indicated otherwise. For the CO adsorption experiments, we used 99.997 vol.% pure carbon monoxide (CO4.7, Messer Griesheim).

The RAIRS spectra were recorded at an instrumental resolution of 4 cm^{-1} , and by adding 400 interferometer scans. Such a spectrum was recorded in about 100 seconds. The spectra were ratioed to an initially recorded background spectrum of 400 scans of the clean sample.

6.3 Results

6.3.1 LEED

First we give a qualitative overview of the LEED patterns that arise at the various CO coverages. Figure 6.2 shows the observed LEED patterns. Adsorbing CO at 300 K results in a $c(2 \times 2)$ pattern (Figure 6.2a) at exposures between 1 and 1.5 L ($1 \text{ L} = 1 \times 10^{-6} \text{ Torr.s}$). At higher exposures the $c(2 \times 2)$ pattern changes into a $p(4\sqrt{2} \times \sqrt{2})R45^\circ$ structure (Figure 6.2b), as was also reported by others [1,2,4,5]. The assignment of the LEED structures will be explained in further detail in the discussion. The open squares in Figure 6.2b denote spots that could only be observed with non-normal incidence of the primary electron beam. This structure persists even at high exposures, i.e. 100 s at 1×10^{-6} mbar. Upon heating the crystal, the $p(4\sqrt{2} \times \sqrt{2})R45^\circ$ reverts to the $c(2 \times 2)$ pattern at about 340 K. Above 400 K the $c(2 \times 2)$ structure becomes faint and disappears till at 500 K only the $p(1 \times 1)$ pattern of the rhodium substrate remains. Adsorbing CO at 370 K results in a $c(2 \times 2)$ pattern, which persists up to saturation.

High exposures of 1×10^{-6} mbar CO for 100 s at 220 K results in the pattern shown in Figure 6.2c. Castner et al. [3] designated this LEED pattern as a "split" (2×1) structure. However, these authors did not observe the low intensity spots, denoted in Figure 6.2c by the small squares. Taking these additional spots into account, we assign this LEED pattern to a $c(6 \times 2)$ structure (see discussion for further detail). Castner et al. [3] also did not observe the $p(4\sqrt{2} \times \sqrt{2})R45^\circ$ structure, however, they report that some complex streaking was observed as the CO overlayer was compressing from the $c(2 \times 2)$ structure into the "split" (2×1) .

Upon heating, a mixture of the $c(6 \times 2)$ and the $p(4\sqrt{2} \times \sqrt{2})R45^\circ$ patterns (Figure 6.2d) appears between 250 and 280 K. At 300 K only the $p(4\sqrt{2} \times \sqrt{2})R45^\circ$ pattern remains. This process is reversible, upon cooling the crystal again and exposing it to 1×10^{-6} mbar CO, a mixture of the two patterns appears at about 280 K, till at 220 K only the $c(6 \times 2)$ pattern is

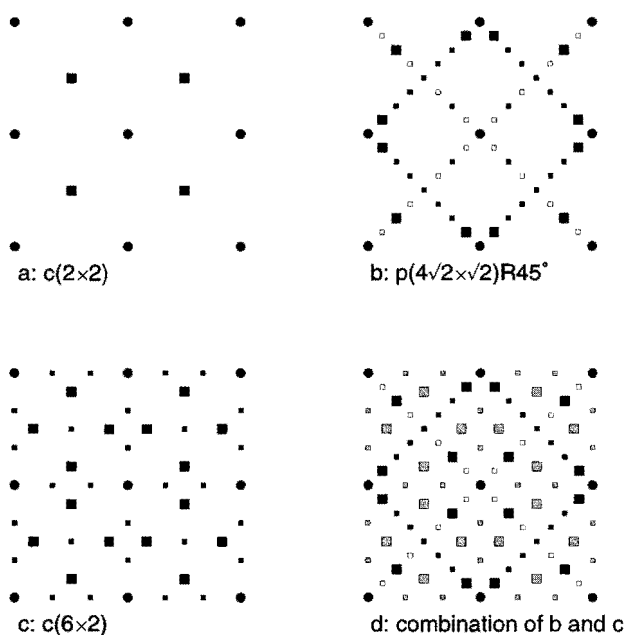


Figure 6.2

LEED patterns observed at different exposures and temperatures. The Rh substrate spots are denoted by the solid circles (●). The large solid squares (■) represent intense overlayer spots, the small solid squares (▣) weak overlayer spots, and the open squares (□) missing spots, only observed at off-normal incidence. a: $c(2 \times 2)$ pattern at 0.5 ML coverage; b: $p(4\sqrt{2} \times \sqrt{2})R45^\circ$ pattern at 0.75 ML coverage; c: $c(6 \times 2)$ pattern, observed after exposure to 1×10^6 mbar CO at 220 K; d: domains of the $p(4\sqrt{2} \times \sqrt{2})R45^\circ$ and $c(6 \times 2)$ structures coexist between 250 and 280 K (the grey squares represent the $c(6 \times 2)$ pattern).

present. Adsorbing 1×10^6 mbar CO for 100 s at 260 K resulted again in a $c(6 \times 2)$ pattern, which gradually transformed to the $p(4\sqrt{2} \times \sqrt{2})R45^\circ$ pattern during the LEED experiment, as the CO gas was pumped out.

6.3.2 TDS

TDS studies were made in an attempt to determine the CO desorption kinetics and the absolute surface coverage. Figure 6.3 shows the TDS spectra of CO adsorbed at 300 K for a number of exposures. At 0.3 L exposure a single peak is observed at 486 K. This peak shifts to lower temperatures with increasing exposures, indicating repulsive interactions between the adsorbed CO molecules. At 0.8 L the desorption peak becomes asymmetric, it

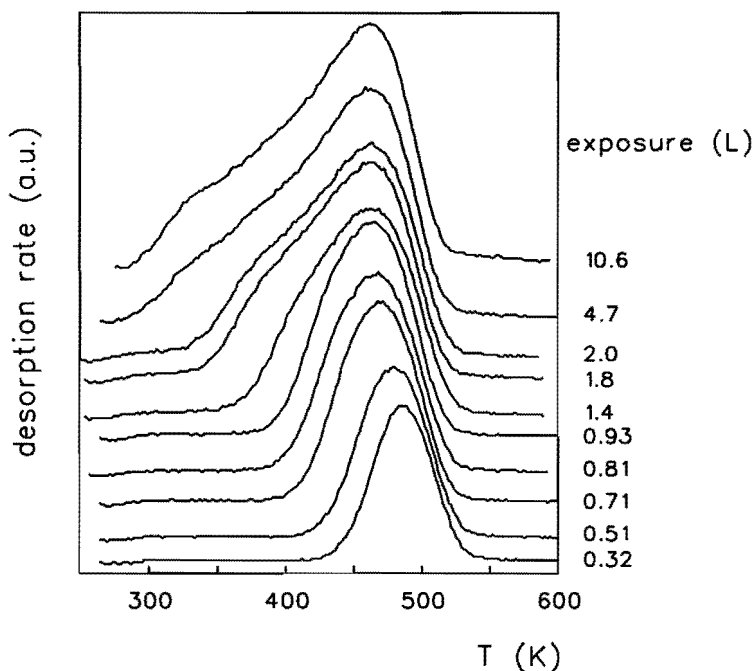


Figure 6.3

TDS spectra of CO adsorbed at 300 K for several exposures. The heating rate is 3.5 K/s.

broadens on the low temperature side, while above 1.2 L a distinct shoulder develops at about 430 K. This second desorption state gains intensity up to exposures of 2 L. At higher exposures a third desorption state appears as a shoulder around 350 K. The observation of the first two desorption peaks is consistent with the data reported by Kim et al. [4]; however, they did not observe the third low temperature peak. Other CO desorption spectra of clean Rh(100) surfaces, reported in coadsorption studies [5,9] with hydrogen and hydrazine, are similar to our results.

The saturation coverage for CO adsorption at 300 K was taken at 0.75 ML as proposed by Tucker [1] and by Richter et al. [5] and as follows from the LEED results (see discussion). Figure 6.4 shows the coverage versus exposure behaviour for the adsorption of CO for two series of desorption experiments. The adsorption process of CO can be described with precursor kinetics as was observed for a wide range of transition metals [10] and for CO on Rh(100) by Kim et al. [4]. In this mechanism, trapping can take place into a precursor state at a filled chemisorption site, with subsequent diffusion to an empty site. The initial sticking coefficient in this case is almost independent of coverage. The sticking coefficient is then described, after Kisliuk [11], as:

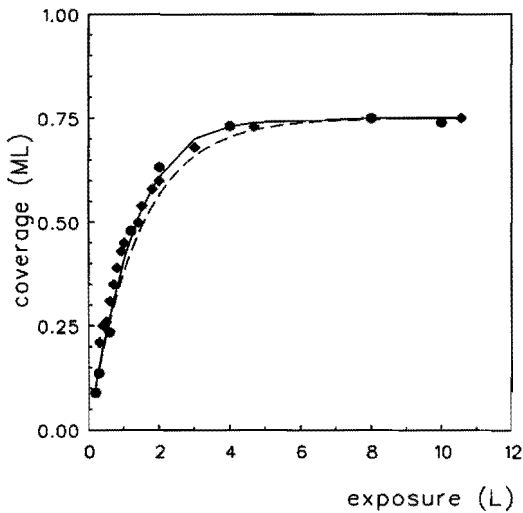


Figure 6.4

Coverage as function of the CO exposure, obtained from two series of TDS spectra of CO adsorbed at 300 K, represented by the diamonds and circles. The solid line shows the uptake-curve, derived from the model after Kisliuk [11], describing precursor kinetics, with $\alpha S_0=0.75$ and $K=0.7$. The dashed line represents the uptake following Langmuir adsorption.

$$S(\theta) = S_0 \frac{1-\theta}{1+(K-1)\theta} \quad (6.1)$$

in which:

- $S(\theta)$ is the sticking coefficient as a function of the coverage
- S_0 is the initial sticking coefficient
- θ is the adsorbate coverage, relative to a monolayer
- K is the so called "precursor state parameter"

From Equation (6.1) it is clear that for $K=1$, the sticking has a Langmuirian dependence on coverage. The CO uptake can be described by:

$$\frac{d\theta}{dt} = \alpha p S(\theta) \quad (6.2)$$

From Equation (6.2) the coverage after a certain exposure time t , at a pressure p can be calculated numerically. The factor α corrects for the number of molecules impinging on the surface as a function of the pressure, and takes into account the ion gauge sensitivity. In Figure 6.4 the solid line shows the uptake curve obtained with an initial sticking coefficient of 0.75 (provided that $\alpha=1$) and $K=0.7$. This value for K of less than unity implies

significant mobility on the surface. On most transition metals, an initial sticking coefficient between 0.2 and 1 was reported for the adsorption of CO [10,12].

Adsorbing CO at different temperatures with a 4 L exposure showed that at 370 K the saturation coverage is 0.5 ML and that only one desorption peak occurs. Between 360 K and 340 K the saturation coverage increases to 0.75 ML. Accompanied with this increase of the surface coverage, a shoulder develops on the low temperature side of the desorption peak.

The application of a simple Redhead analysis [13] to the low coverage desorption peaks, assuming a preexponential factor of $1.0 \times 10^{13} \text{ s}^{-1}$ and a first order desorption process, yields an activation energy for desorption ranging from 124 to 127 kJ/mole. Extrapolation to zero coverage results in an activation energy of $130.5 \pm 0.5 \text{ kJ/mole}$. A method proposed by Chan et al. [14], based on the peak maximum temperature and peak width, was also used to determine the desorption energy and the preexponential factor. This method only yields relevant information for the zero coverage limit [15]. Analysis of the spectra at low coverage, i.e. lower than those at which the shoulder develops, and extrapolating to zero coverage yields a desorption energy of $131 \pm 4 \text{ kJ/mole}$ and a preexponential of $4 \pm 3 \times 10^{16} \text{ s}^{-1}$. This value of the preexponential factor corresponds well to a mobile precursor state for the adsorption-desorption process. The values for the desorption energies are in good agreement with the results of Kim et al. [4]. These authors, however, obtained a preexponential factor of $8.4 \times 10^{12} \text{ s}^{-1}$. Since they also refer to Chan's method and found the same activation energy for desorption, we can not explain this low value of the preexponential factor. Using the data mentioned in their paper, we calculate a prefactor of $3 \times 10^{16} \text{ s}^{-1}$, which would be in good agreement with our results.

6.3.3 RAIRS

CO adsorption at 300 and 270 K

Figure 6.5 shows the RAIRS spectra of CO adsorbed on Rh(100) at 300 K as a function of the CO coverage. Each spectrum was obtained after exposing the crystal to a certain amount of CO at 300 K, at pressures between 5×10^{-9} and 1×10^{-8} mbar. After each recorded spectrum the crystal was flashed and a TDS spectrum was taken. From the TDS data the actual coverage for each RAIRS spectrum was determined.

As Figure 6.5 shows, identical to results reported in a HREELS study [2], two adsorption bands are observed over the whole coverage range. The band in the region 2004 to 2054 cm^{-1} is assigned to CO bonded in an on top position and the band in the region 1871 to 1944 cm^{-1} to twofold bridge bonded CO. At coverages up to 0.5 ML the linear CO species predominates in the spectrum. Above 0.5 ML coverage the intensity of the linear CO band decreases and the intensity of the bridged CO band increases. At saturation a shoulder appears on the low frequency side of the linear peak at 2031 cm^{-1} . With increasing coverage the peaks shift to higher frequency, mainly caused by dipole interactions. At 0.5 ML

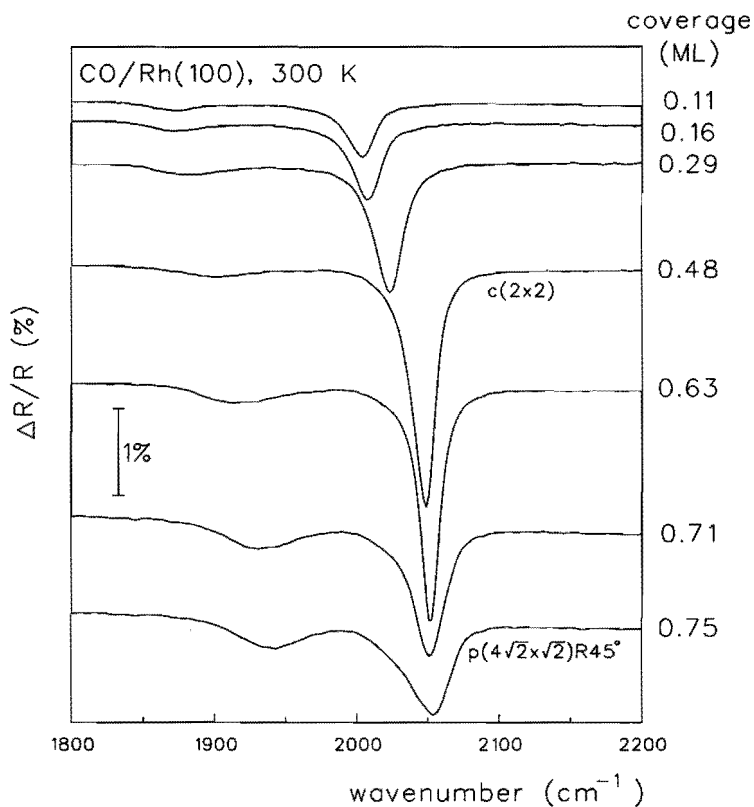


Figure 6.5

RAIRS spectra of CO adsorbed on Rh(100) at 300 K, for different CO coverages.

coverage the linear CO peak is highly symmetric and narrow, indicating a well ordered surface structure [16].

Figure 6.6 shows the RAIRS spectra of CO adsorbed at 270 K as a function of the CO coverage, and for higher pressure CO exposures. The coverages have been obtained from the coverage-exposure curve, as determined from several TDS experiments (Figure 6.4). The spectra were taken after successively exposing the crystal to CO, and under an ambient pressure of CO. The adsorption behaviour is the same as observed at 300 K, except for the additional linear CO peak at 2031 cm^{-1} , which grows in at coverages above 0.7 ML. This peak is more pronounced at 270 K. Spectra taken at higher CO pressures show that the linear peak at 2060 cm^{-1} gains intensity and shifts to higher frequency. At 5×10^{-7} mbar ambient CO pressure and higher, a sharp, highly intense peak of linear CO is observed at 2074 cm^{-1} and the low frequency linear peak and the bridged CO peak have almost disappeared. Heating to 300 K causes this peak to shift back to 2070 cm^{-1} and to decrease in intensity, while

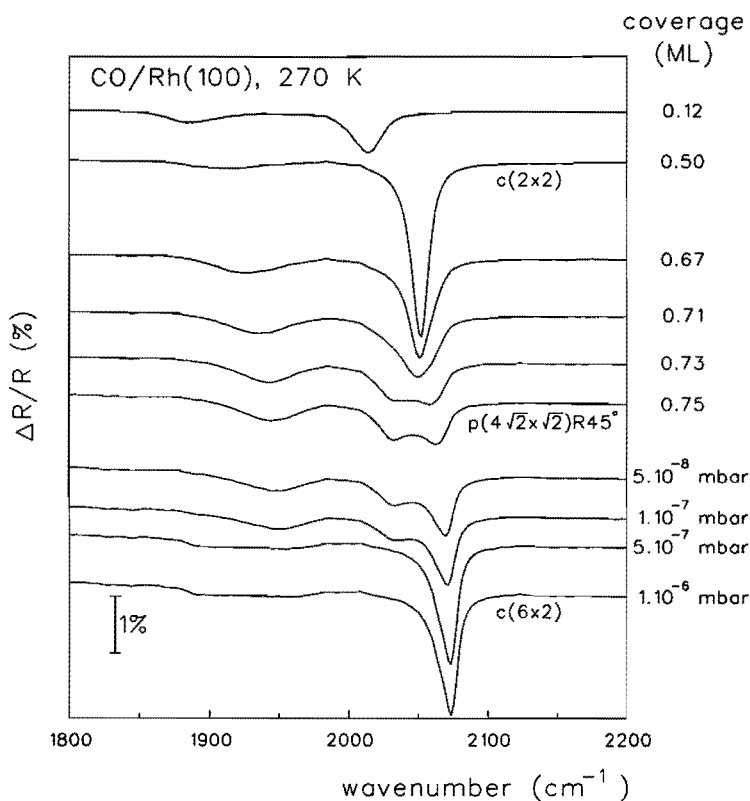


Figure 6.6

RAIRS spectra of CO adsorbed on Rh(100) at 270 K, for different CO coverages up to 0.75 ML, and at higher CO pressures.

concomitantly the second linear peak (2031 cm^{-1}) and the bridged CO peak reappear (not shown). Recooling results again in the intense linear peak at 2074 cm^{-1} . This behaviour indicates that there is a change in the structure of the CO overlayer between 270 and 300 K.

Figure 6.7 shows the frequencies of the observed peaks of the spectra in Figure 6.5 and Figure 6.6 as a function of coverage. We observe an almost monotonic increase of the vibrational frequency of both infrared absorption bands up to 0.5 ML coverage. This can be attributed to dipole-dipole coupling. Above 0.5 ML, the frequency of the bridged CO peak increases strongly till approximately 0.7 ML coverage, whereas the linear CO peak does not change in frequency between 0.5 ML and 0.7 ML. Around 0.7 ML, the shoulder develops on the linear peak. The latter shifts up in frequency until saturation coverage, while on the other hand the just developed second linear peak (or shoulder) shifts to lower frequency. Exposure to 1×10^{-6} mbar CO at 270 K causes the high frequency linear peak to shift up to

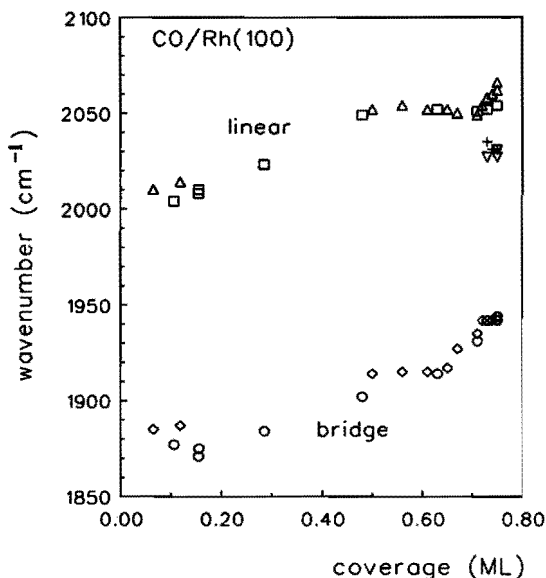


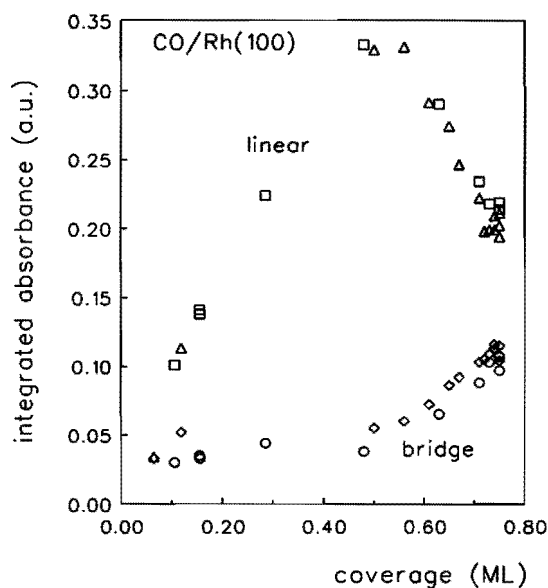
Figure 6.7

The CO stretch frequencies as a function of the coverage of CO adsorbed on Rh(100) at 270 K (Δ : linear, \diamond : bridge, +: low frequency linear peak) and 300 K (\square : linear, \circ : bridge, ∇ : low frequency linear peak) in the coverage range up to 0.75 ML.

2074 cm^{-1} , while the other peaks disappear.

Figure 6.8 displays the integrated absorption intensities as a function of coverage of the linear and bridged CO bands for the adsorption of CO at 270 and 300 K. The absorption intensity of the linear CO band increases strongly with increasing CO coverage, then it levels off a little, till 0.5 ML coverage is reached. Concomitantly the linear CO peak narrows with increasing coverage till at 0.5 ML the band is highly symmetric and narrow. This indicates that at 0.5 ML coverage, where LEED experiments show a sharp $c(2 \times 2)$ pattern, a highly ordered overlayer structure is formed [2]. This characteristic intensity increase of the linear CO up to 0.5 ML coverage can again be attributed to dipole-dipole coupling interactions (see discussion for further detail). The integrated absorption intensity of the bridged CO band is low and at about a constant level up to 0.5 ML coverage. From 0.5 ML to saturation coverage the intensity of the bridged CO band increases concomitant with a strong decrease of the linear CO band intensity. This suggests a site change of CO from linear to bridge bonded. This was also observed with HREELS [2], RAIRS [6] and more indirectly concluded from work function measurements [17]. The integrated absorption intensity of the linear CO band at nearly saturation coverage reflects the total intensity of both linear IR bands. From Figure 6.8 it is clear that, at saturation coverage, the absorption intensity of the linear CO is about twice as high as the intensity of the bridged CO. Thus, we find at a saturation coverage of 0.75 ML two types of linear bonded CO and a bridged bonded CO species; at this stage we observed a $p(4\sqrt{2} \times \sqrt{2})R45^\circ$ overlayer structure with LEED.

Although 0.75 ML represents the saturation coverage under UHV conditions, higher coverages are possible if a background pressure of CO is applied. An exposure to

**Figure 6.8**

Integrated absorption intensities of the CO bands as a function of coverage, for CO adsorbed on Rh(100) at 270 K (Δ: linear, ◇: bridge) and 300 K (□: linear, ○: bridge) in the coverage range up to 0.75 ML. The intensity of the linear peak represents the total intensity of both linear species.

1×10^{-6} mbar CO at 270 K causes a large increase in the absorption intensity of the linear CO band concomitant with a strong decrease of the bridged CO band intensity. The presence of this sharp intense linear CO band suggests a highly ordered CO overlayer structure. With LEED experiments we observed at this temperature a mixture of the $p(4\sqrt{2} \times \sqrt{2})R45^\circ$ and the $c(6 \times 2)$ structures, however after pumping to UHV. We believe that under 1×10^{-6} mbar CO the $c(6 \times 2)$ structure persists. The occurrence of the mixture of the two structures is probably caused by partial desorption of the CO adlayer, as we were not able to perform LEED experiments at such high ambient pressures. However exposing at 1×10^{-6} mbar CO at 220 K, showed a sharp $c(6 \times 2)$ LEED pattern after pumping away the CO. Apparently at this temperature the desorption of CO from the dense overlayer was very slow. RAIRS experiments showed that after high exposures of CO at 270 K and pumping away the CO the intense linear CO band remained, although it lost some intensity. This indicates that some CO desorbs but the system does not go back to 0.75 ML coverage.

CO adsorption as a function of temperature at 1×10^{-7} mbar CO

The adsorption of CO in equilibrium at different temperatures, gives insight into the saturation coverage as a function of temperature. In Figure 6.9 RAIRS spectra are shown of a CO saturated surface in a cooling-heating cycle from 373 K to 282 K and back to 473 K. The spectra were taken under an ambient CO pressure of 1×10^{-7} mbar by adding 10 sample scans and ratioing to a previously stored background spectrum. The cooling rate was between 0.5 and 1 K/s and the heating rate between 1 and 2 K/s. Each RAIRS spectrum was recorded in about 2 seconds.

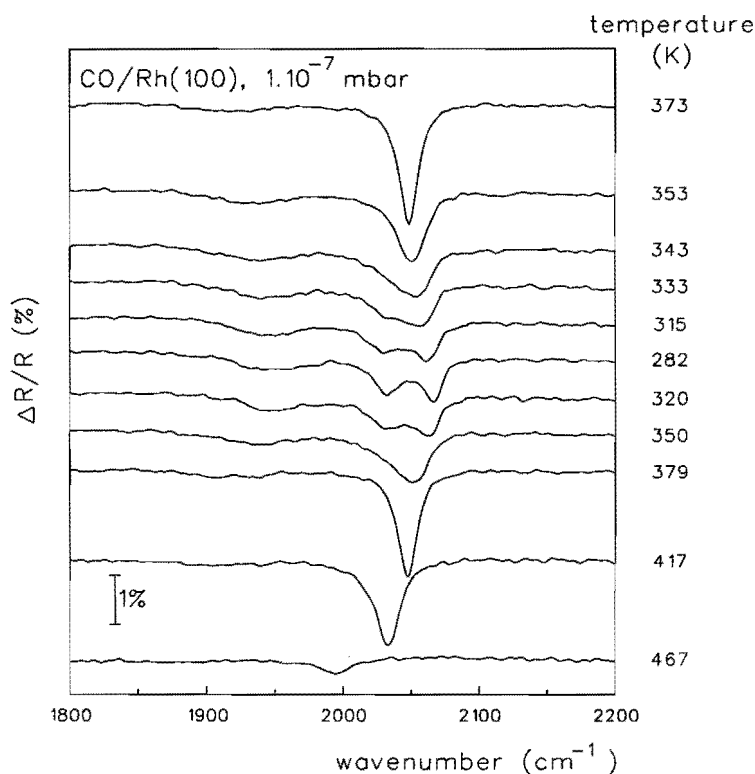


Figure 6.9

RAIRS spectra of CO adsorbed on Rh(100) under 1×10^{-7} mbar ambient CO pressure. During adsorption the crystal temperature was ramped from 373 to 282 K and back to 473 K.

Starting at 373 K, the RAIRS spectrum shows a symmetric intense band of linear bonded CO at 2049 cm^{-1} and a small peak of bridge bonded CO at 1915 cm^{-1} . This spectrum is characteristic of a coverage of 0.5 ML of CO. Additional RAIRS experiments showed that exposing the crystal to different amounts of CO at 370 K results in spectra in which the linear CO band is dominant. At saturation coverage the same spectrum is observed as in Figure 6.9 for 373 K. TDS experiments showed that an at 370 K saturated surface gives a single desorption peak. With LEED a $c(2 \times 2)$ pattern was observed after saturating the surface at 373 K. From this we conclude that the saturation coverage of CO at 370 K is 0.5 ML. The CO molecules are adsorbed in a highly ordered $c(2 \times 2)$ structure with CO mainly in a linear bonded adsorption site, reflected by the highly symmetric intense linear CO band. The high temperature desorption peak in the TDS spectra of Figure 6.3 is attributed to the desorption of this type of CO.

When the temperature decreases the linear CO band broadens, decreases in intensity and

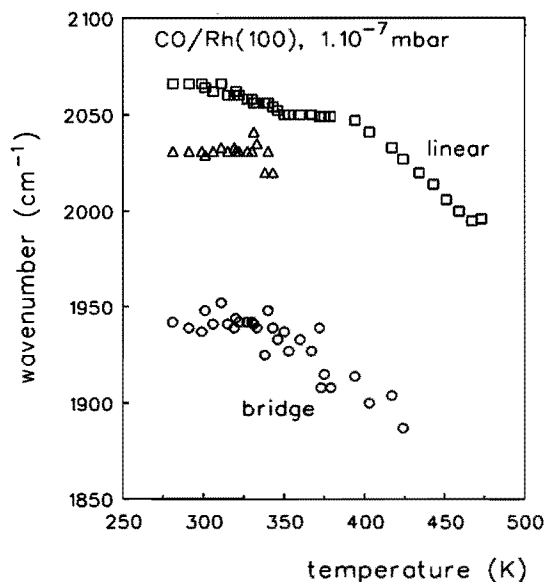


Figure 6.10

Frequency of the CO bands (\square : linear, \circ : bridge, \triangle : second linear peak), of CO adsorbed on Rh(100) at 1×10^{-7} mbar ambient CO pressure, as a function of temperature.

shifts to higher frequency, while the bridged CO band gains in intensity and shifts up in frequency. At 343 K a shoulder develops on the low frequency side of the linear CO band. At lower temperatures the shoulder becomes a resolvable peak at 2031 cm^{-1} , as the other linear CO band shifts to higher frequency. The spectrum at 282 K is very similar to the spectrum obtained at 270 K under 1×10^{-7} CO, as pictured in Figure 6.6. When the temperature is increased again, the process is reversed till at 379 K again the intense linear CO band, characteristic of the $c(2 \times 2)$ structure, is observed. Further increase of the temperature diminishes the peak intensity, while it shifts to lower frequency as CO desorption proceeds. Since at higher temperatures no bridged CO species are detected, it is concluded that at low coverages CO desorbs from an on-top adsorption site. At 473 K almost all CO has desorbed and a small linear CO band is detected at 1995 cm^{-1} (not shown).

Figure 6.10 and Figure 6.11 show the observed frequencies and the integrated absorption intensities respectively of the CO bands of the cooling-heating series as a function of temperature. As data obtained during cooling and heating coincide, it is clear that the adsorption-desorption process is completely reversible. We can roughly distinguish three different regions, as was also observed in the isothermal adsorption experiments. At low temperatures, where the surface is saturated with 0.75 ML CO, there are three different types of CO. Between 310 and 350 K some CO desorbs from this structure, as reflected by the decrease in the CO stretch frequency of the high frequency linear bonded CO. This corresponds to the low temperature desorption peak observed in the TDS experiments (Figure 6.3). From 350 to 380 K the amount of bridge bonded CO decreases, concluded from the decrease in both the integrated absorption intensity and frequency. In this region only one

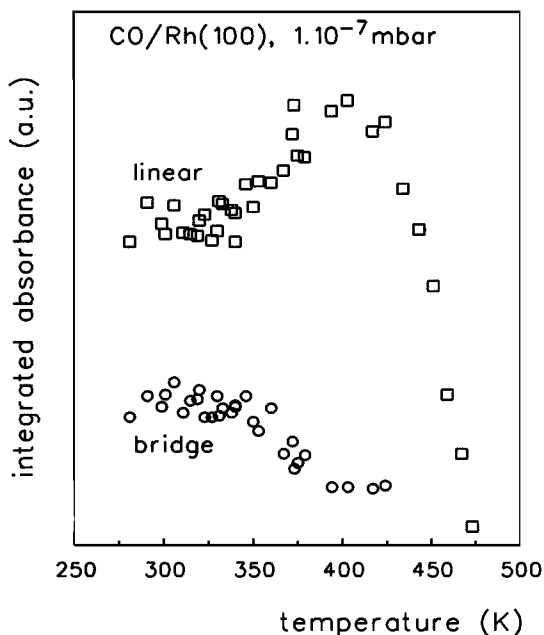


Figure 6.11

Integrated absorption intensity of the CO bands (\square : linear, \circ : bridge), of CO adsorbed on Rh(100) at 1×10^{-7} mbar CO pressure, as a function of temperature.

type of linear bonded CO is observed, which increases in absorption intensity as the amount of bridged CO decreases, indicating that the bridged bonded CO species goes over to a linear adsorption site as part of the CO desorbs. This region corresponds to the second desorption peak in the TDS spectra (Figure 6.3). The constant CO stretch frequency of the linear CO between 350 and 380 K, can be explained as follows. The increasing amount of linear CO would cause an upward shift resulting from dipole-dipole coupling. The decrease of the total CO coverage, however, enhances the metal-CO bond, which results in a weakening of the C-O bond. This yields a decrease in the CO frequency. Above 380 K the rest of the CO-adlayer desorbs, reflected by the decrease in frequency and absorption intensity of both the linear and bridged CO peaks. It is clear that bridge bonded CO disappears first and forms the weakest bond with the surface.

6.4 Discussion

The combination of LEED, TDS and RAIRS applied at different temperatures and pressures gives detailed insight into the adsorption of CO on Rh(100). There are four different coverage regions distinguishable, which we will briefly summarize.

$0 < \theta < 0.5$: CO adsorbs mainly in linear adsorption sites, till at 0.5 ML a $c(2 \times 2)$ LEED pattern is formed. In TDS a single CO desorption state is observed.

- $0.5 < \theta < 0.7$: CO occupies increasingly twofold bridge sites and a second desorption state appears.
- $0.7 < \theta < 0.75$: A second linear CO species appears and a $p(4\sqrt{2} \times \sqrt{2})R45^\circ$ LEED pattern is formed. At this stage a third TDS desorption peak occurs at a desorption temperature of around 340 K.
- $\theta > 0.75$: At temperatures well below room temperature and high CO pressures, i.e. above 5×10^{-7} mbar, CO adsorbs in a structure corresponding to a $c(6 \times 2)$ LEED pattern, in which CO occupies largely linear adsorption sites.

For the low coverage region there seems to be general agreement concerning the CO adsorbate structure. At 0.5 ML coverage several authors find a $c(2 \times 2)$ LEED pattern [2-4,6] as well as a single CO desorption peak [4]. We find that up to coverages of 0.5 ML, CO adsorbs in essence on linear adsorption sites, as was also reported by Gurney et al. [2] and Kao et al. [18]. Linear CO adsorption for low CO coverages has also been observed on Rh(111) [19-21] and Ni(100) [22]. The RAIRS results reported by Leung et al. [6] are contradictory to this. The infrared spectra reported by these authors [6] of CO adsorption on Rh(100) at 300 K show a high content of bridged CO species (about half as much as linear). It is likely that these results suffer from a small surface contamination. We have also measured spectra similar to those reported by Leung et al. [6], but then several facts indicated the presence of a surface (or near-surface) contamination, although no other elements than rhodium were detected with AES. At first, the IR absorption peaks showed some asymmetry and were slightly broadened, indicating that the CO adlayer was distorted in some way. Secondly, the intensity of the absorption band was lower and TDS showed that saturation coverage could not be reached entirely. A possible explanation is that part of the adsorption sites was blocked. Further, the desorption peak temperature was lower, suggesting a weaker bonded CO species. Since the detection limit of AES is not lower than a few percent of a monolayer and is even worse for sub-surface species, TDS and RAIRS of adsorbed CO are much more sensitive to contaminations. Therefore we think that the CO desorption temperature and the RAIRS absorption band shapes are a better indication for a clean surface than an AES spectrum that shows no presence of contaminants. The RAIRS results of CO adsorption at 300 K reported by Leung et al. [6] contradict also with their own results obtained at 90 K. The latter do not show large amounts of bridged CO at coverages below 0.5 ML and are in good agreement with the HREELS results of Gurney et al. [2] and our RAIRS results, that is, in this coverage region. Since they claim in the same paper that linear adsorption sites get increasingly occupied with increasing temperature, the higher content of bridged CO at 300 K can not be explained. Moreover, they report a saturation coverage at 300 K of 0.6 ML, which is too low because CO desorbs only above 300 K, as we observed [4,5].

The shift in frequency and the integrated absorption intensity of the CO absorption band with increasing coverage, as shown in Figure 6.7 and Figure 6.8, are due to dipole-dipole interactions. Screening, due to the electronic polarizability of the adsorbed molecules, reduces

both the frequency shift and the absorption intensity, as was demonstrated by Persson and Ryberg [23]. We will illustrate for the linear CO band, since it largely dominates the spectra up to 0.5 ML, that the frequency shift can be described entirely by dipole coupling. The centre frequency and adsorption band area as a function of coverage can, after Persson and Ryberg [23], be described as:

$$\left(\frac{\omega}{\omega_0}\right)^2 = 1 + \frac{\theta\alpha_v U}{1 + \theta\alpha_e U} \quad (6.3)$$

$$\int \frac{\Delta R}{R} d\nu = \frac{\theta\alpha_v U}{[1 + \theta\alpha_e U]^2} \quad (6.4)$$

in which:

- ω is the vibrational frequency of the observed infrared band
- ω_0 is the vibrational frequency at low coverage ($\omega_0=1995 \text{ cm}^{-1}$)
- $\Delta R/R$ is the reflectivity change
- ν is the frequency of the infrared light
- θ is the adsorbate coverage
- α_v is the vibrational polarizability of the adsorbed molecule
- α_e is the electronic polarizability of the adsorbed molecule
- U is the summation term of the dipoles over a $c(2 \times 2)$ overlayer structure, taking into account the image dipoles of the adsorbed molecules ($U=0.3 \text{ \AA}^{-3}$)

In Figure 6.12 the area and frequency of the linear CO peak are plotted against the coverage. The dashed lines represent the fits of the peak area and the frequency as function of the coverage, according to the model of Persson and Ryberg [23]. The data were fitted by varying α_v and α_e till the best fit was obtained. For the fits we used:

$$\alpha_v=0.48 \text{ \AA}^3, \quad \alpha_e=1.8 \text{ \AA}^3$$

The model is valid until 0.5 ML, because above this coverage the structure of the adsorbate overlayer changes. From Figure 6.12 it is clear that the effect of dielectric screening with increasing coverages describes the non-linear relation of the frequency shift and the band intensity with the coverage very well. Thus the frequency shift and band intensity as function of the coverage can be assigned to dipole coupling, provided that dielectric screening is taken into account.

Gurney et al. [2] determined the ratio of the dynamic dipole moments of the linear and bridged CO band by fitting a weighted sum through the TDS uptake curve. This can not be

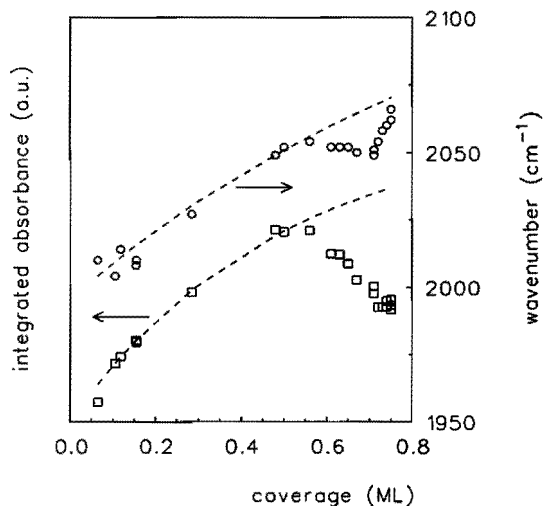


Figure 6.12

Integrated absorption intensity (□) and frequency (○) of the linear CO band as function of the coverage. The dashed lines represent the fits after the model of Persson and Ryberg [23].

correct, since, considering the effect of dielectric screening [23], the band intensity does not entirely follow the TDS uptake curve. The method may only be applied if there is a linear relation between the band intensity and the coverage. Gurney et al. [2] also determined the ratio of the dynamic dipole moments of linear and bridged CO from reversible temperature ramps at a fixed coverage of 0.5 ML. From this they obtained that the dynamic dipole moment of linear CO was about twice that of bridged CO. Since the IR absorption band intensity is proportional to the square of the dynamic dipole moments, this means that at 0.5 ML coverage the amount of bridged CO should be multiplied by 2 relative to the linear CO. Assuming that this ratio of the dipole moments does not change from 0.5 to 0.75 ML coverage, these authors [2] found that at saturation coverage an equal number of linear and bridged sites is occupied.

Not all authors seem to agree on the saturation coverage of CO and the adsorbate overlayer structure above 0.5 ML coverage. Peebles et al. [17] observed a step in the work function change with increasing CO coverage at 0.4 ML, which was attributed to a change from linear to bridged bonding. The CO coverage was calibrated [4] by assigning 0.5 ML coverage to a dose of 1.65 L, as at this exposure the authors chose the $c(2 \times 2)$ LEED pattern to be complete. Since at this coverage the CO uptake curve is still very steep, which means that the coverage changes relatively much with the exposure, this determination of the absolute coverages can not be very accurate. This might also explain the low value of the saturation coverage of 0.6 ML. If we now assign the saturation coverage to 0.75 ML, then the site change occurs at 0.5 ML instead of 0.4 ML coverage.

Leung et al. [6] observed with RAIRS at 0.5 ML coverage a reduction of the linear CO band and an increase of the bridged CO band, till the bands had about equal intensity at

0.6 ML. As the coverage was increased further the linear band gained again intensity and the bridged band lost intensity, till at 0.7 ML the linear to bridge intensity ratio was about 2. The latter is in agreement with our results. For the anomalous behaviour at 0.6 ML these authors have no explanation.

HREELS results [2] at CO coverages of 0.75 ML showed about an equal intensity of the linear and bridged CO peaks. This is in disagreement with the RAIRS results, but may be due to the intrinsically lower resolution of the EELS spectra. Moreover, the shoulder on the low frequency side of the linear peak as observed in our results (Figure 6.5 and Figure 6.6), might erroneously be assigned to an increase of the bridged band in an EELS experiment. Based on these EELS results, Gurney et al. [2] proposed a model for the adsorbate overlayer structure corresponding to the $p(4\sqrt{2} \times \sqrt{2})R45^\circ$ LEED pattern at 0.75 ML coverage, in which CO occupies twice as many bridge sites as top sites.

The compression of the CO overlayer with increasing coverage in structures like the $p(4\sqrt{2} \times \sqrt{2})R45^\circ$ pattern has been observed for many other metals with a (100) surface orientation, like Ni, Cu, Pd and Pt [24,25]. According to Biberian and Van Hove [24], the $p(4\sqrt{2} \times \sqrt{2})R45^\circ$ LEED pattern can be interpreted in two different ways. In the first approach it is assumed that the observed LEED patterns are composed of diffraction spots originating from either the substrate or the adsorbate, or from double diffraction between the substrate and the overlayer. Normally, only intense spots are taken into account, other spots are composed of linear combinations of the reciprocal lattice vectors of the substrate and the adsorbate with small (h,k) indices. This interpretation leads to a compact model for the adsorbed CO overlayer, which forms a pseudo hexagonal overlayer on the surface. The second approach assumes that there is a coincidence unit cell between the substrate and the overlayer, giving rise to a superstructure. All the spots, not originating from the substrate, are then due to the existence of the coincidence unit cell.

In Figure 6.13a the $p(4\sqrt{2} \times \sqrt{2})R45^\circ$ LEED pattern is shown with the reciprocal lattice unit cells, according to the two approaches. The solid line denotes the reciprocal lattice unit cell, according to the compact model. From this cell the real space unit cell as depicted in Figure 6.13b is derived. Expressing this unit cell in the base vectors of the substrate lattice, we get:

$$\begin{pmatrix} \vec{A} \\ \vec{B} \end{pmatrix} = \begin{pmatrix} \frac{1}{6} & 1 \\ \frac{7}{6} & -1 \end{pmatrix} \begin{pmatrix} \vec{a} \\ \vec{b} \end{pmatrix}$$

The area of this unit cell is 8/6, this means that six CO molecules cover eight Rh atoms. From this follows that the coverage is 0.75 ML. The dashed line in Figure 6.13a denotes the coincidence lattice unit cell, resulting in the $p(4\sqrt{2} \times \sqrt{2})R45^\circ$ structure (Figure 6.13b). It

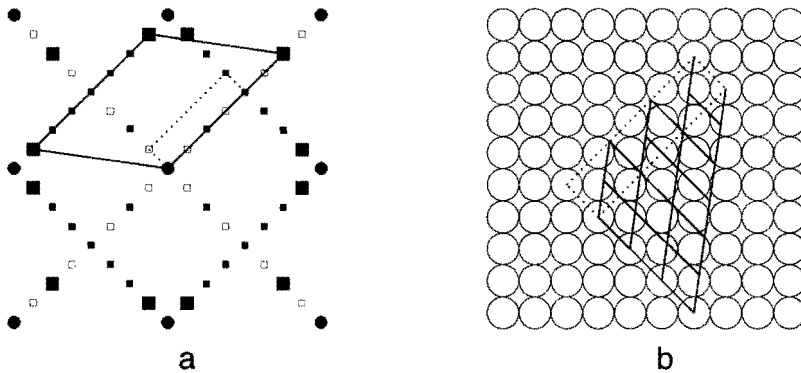


Figure 6.13

LEED pattern (a) with the reciprocal unit cells, and the corresponding real space (b) unit cells, of 0.75 ML CO adsorbed on Rh(100). The solid lines represent the unit cell according to the compact model, the dashed lines according to the coincidence lattice $p(4\sqrt{2}\times\sqrt{2})R45^\circ$ structure. The Rh substrate spots are denoted by the solid circles (●). The large solid squares (■) represent intense overlayer spots, the small solid squares (■) weak overlayer spots, and the open squares (□) missing spots, only observed at off-normal incidence.

is clear that both methods lead to the same result.

At normal incidence there are systematic extinctions in the $p(4\sqrt{2}\times\sqrt{2})R45^\circ$ structure, indicating a symmetry of the adlayer, involving glide planes in the long direction of the unit cell, as was proposed by Gurney et al. [2]. Since there are two domains of the $p(4\sqrt{2}\times\sqrt{2})R45^\circ$ structure possible, rotated by 90° , a glide plane in the other direction can not be detected. Considering the fact that per unit cell of eight Rh atoms, there are six CO molecules, and both linear and bridged sites are occupied, there are only two possible models for this adsorbate structure, which explain this LEED pattern. Either in each unit cell there are four linear and two bridge bonded CO molecules, or vice versa. The infrared experiments revealed a linear to bridge ratio of 1.8, provided that the absorption probability for both molecules is equal. The ratio of the square of the dynamic dipole moments has been determined as 2.0 ± 0.3 by Gurney et al. [2] and 4.0 ± 0.5 by Leung et al. [6], corresponding to a bridge over linear ratio between 1.1 ± 0.2 and 2.2 ± 0.3 for our results. This ratio of bridge over linear is also supported by the intensity decrease of the linear CO band in the infrared spectra exceeding 0.5 ML coverage. This intensity decrease can not be explained by the effect of electronic depolarization alone, but is clearly due to a reduction of the linear bonded CO species. Since the coverage of the linear CO species is significantly less than a 0.5 ML equivalent, the coverage of 0.75 ML can only be explained by assuming that CO occupies either an equal number or twice as much bridged as linear sites.

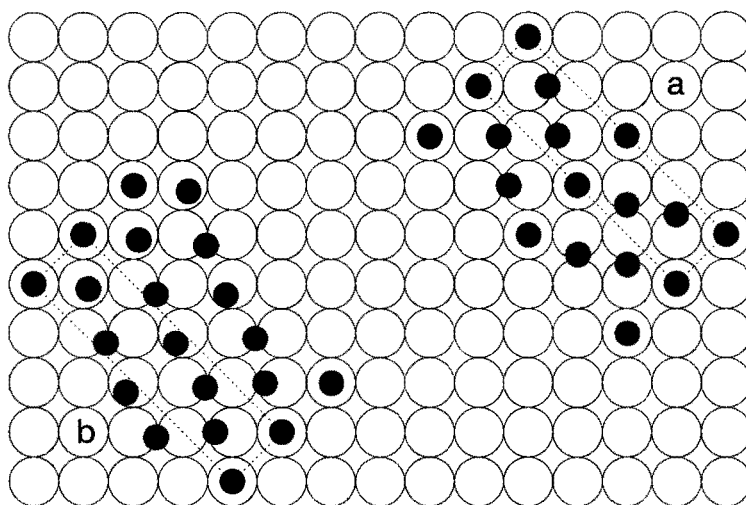


Figure 6.14

Models for the CO overlayer structure at 0.75 ML coverage, for a linear:bridge ratio of 1:2 (a) and for linear and bridged sites equally occupied (b). The dashed lines denote the unit cells.

The ratio of bridged over linear bonded CO has to be 2, to explain the LEED pattern described above. This leads to the model depicted in Figure 6.14a for the CO adsorbate overlayer structure, which is similar to the model proposed by Gurney et al. [2]. Although this model does explain the LEED results very well, it does not account for the two different linear CO species observed with RAIRS. Further the model implies that a rather high ratio of 3.6 for the squares of the dynamic dipole moments is obtained.

Assuming that CO is adsorbed in an equal number of linear and bridged sites, the model shown in Figure 6.14b is derived. The ratio of the squares of the dipole moments in this case is 1.8, which is significantly less than the ratio of 3.6 in the former model. This value of 1.8 seems to be more realistic, since calculations of CO on platinum clusters pointed out that the dynamic dipole moment is rather insensitive to the adsorption site [26]. However, the model now lacks the involvement of glide lines in the overlayer structure. A possible explanation might be that the missing spots at normal incidence are just very faint and obscured by the more intense spots. Further, most sites in the unit cell can still be transposed into each other by a glide line symmetry operation, which might still cause a significant extinction of some spots. In this model there are two different types of linear sites in each unit cell, a site with only bridged sites as neighbours and two sites with both bridged and linear sites as neighbours. The tilt of the CO molecules on the former is higher, resulting in more overlap of the $2\pi^*$ orbitals of the CO molecule with the orbitals of the metal substrate, which causes the CO stretch frequency to be lower. This corresponds well to the infrared spectra, which

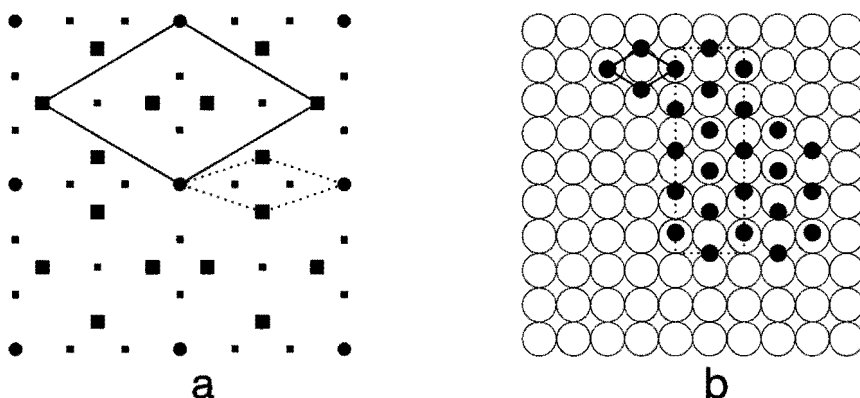


Figure 6.15

LEED pattern (a) with the reciprocal unit cells, and the corresponding real space (b) unit cells, of 0.83 ML CO adsorbed on Rh(100). The solid lines represent the unit cell according to the compact model, the dashed lines according to the coincidence lattice $c(6 \times 2)$ structure. The Rh substrate spots are denoted by the solid circles (●). The large solid squares (■) represent intense overlayer spots and the small solid squares (■) weak overlayer spots. From the real space representation it is clear that both models yield the same overlayer structure.

show a higher intensity (about twice as high) of the high frequency linear CO bands.

Exposing the Rh(100) surface to ambient CO pressures of more than 5×10^{-7} mbar, causes a compression of the CO adsorbate structure into a more densely packed overlayer. A similar behaviour was observed for the adsorption of CO on the unreconstructed Pt(100) surface, after high pressure CO exposures by Bonzel and coworkers [27]. This compression only occurs at temperatures well below room temperature, as pointed out in connection with the RAIRS and LEED experiments. We propose that this is determined by a competition between the adsorption and desorption rate. At room temperature the desorption rate is probably still much higher than the adsorption rate, which causes that the dense overlayer structure is not formed. At 220 K, the structure is stable, even when the CO gas phase has been pumped away, implying that at this temperature the desorption rate has become very slow.

The $c(6 \times 2)$ LEED pattern can again be interpreted in two different ways. In Figure 6.15a the $c(6 \times 2)$ LEED pattern is shown with the reciprocal lattice unit cells, according to the compact model and the coincidence lattice model. The solid line denotes the reciprocal lattice unit cell, according to the compact model. From this cell the real space unit cell as depicted in Figure 6.15b is derived. Expressing this unit cell in the base vectors of the substrate lattice, we get:

$$\begin{pmatrix} \vec{A} \\ \vec{B} \end{pmatrix} = \begin{pmatrix} 1 & \frac{3}{5} \\ 1 & -\frac{3}{5} \end{pmatrix} \begin{pmatrix} \vec{a} \\ \vec{b} \end{pmatrix}$$

The area of this unit cell is $6/5$, from which follows that the coverage is 0.83 ML, as was also proposed by Castner et al. [3]. The dashed line in Figure 6.15a denotes the coincidence lattice unit cell, resulting in the $c(6 \times 2)$ structure (Figure 6.15b). Since both methods lead to the same result, we conclude that the surface overlayer structure should be denoted as a $c(6 \times 2)$ instead of a "split" (2×1) structure.

The model of the adsorbate structure is depicted in Figure 6.15b, each unit cell containing two CO molecules in a bridged and eight CO molecules in a linear configuration. It is proposed that the CO molecules occupying linear sites are tilted, to obtain equal distances between the CO molecules in the long direction of the unit cell. The distance between the CO molecules in this overlayer structure is about 3.2 \AA . Small intermolecular distances of compressed CO overlayers have been reported earlier for several transition metals [19,24]. The relative intensity observed with RAIRS for the linear and bridged bonded CO is about 7. Since CO occupies four times as many linear than bridged sites, this again yields a ratio of the square of the dynamic dipole moments of 1.8.

LEED experiments showed that, when the crystal was heated, the $c(6 \times 2)$ pattern transforms into a mixture of a $c(6 \times 2)$ and $p(4\sqrt{2} \times \sqrt{2})R45^\circ$ pattern, in the temperature range from 250 to 280 K. We believe that at this stage, domains of the $c(6 \times 2)$ and the $p(4\sqrt{2} \times \sqrt{2})R45^\circ$ structure coexist. Similar effects were observed at 260 K, where initially a $c(6 \times 2)$ pattern was observed, which slowly turned into the $p(4\sqrt{2} \times \sqrt{2})R45^\circ$ pattern. It is clear that the ability to form the compressed $c(6 \times 2)$ overlayer depends strongly on the adsorption-desorption equilibrium.

6.5 Conclusions

The population of CO in different adsorption sites on Rh(100) was studied, as a function of coverage, temperature and CO pressure. The results are briefly summarized in Table 6.1. On adsorption CO initially occupies linear adsorption sites, till 0.5 ML coverage, where a $c(2 \times 2)$ structure is formed. With increasing coverage the $c(2 \times 2)$ structure transforms into a $p(4\sqrt{2} \times \sqrt{2})R45^\circ$ structure, in which CO occupies equal numbers of linear and bridged adsorption sites. The CO coverage, when this structure occurs, is 0.75 ML. Applying high CO pressures, the overlayer is further compressed into a highly symmetric $c(6 \times 2)$ structure, with CO occupying four times as much linear as bridged adsorption sites and a coverage of 0.83 ML. This compressed structure is not formed at CO pressures lower than 5×10^{-7} mbar,

Table 6.1*Adsorption of CO on Rh(100).*

coverage (ML)	adsorption state	frequency (cm ⁻¹)	structure	remarks
$\theta=0$	linear	1995	-	$E_{\text{des}} \approx 131$ kJ/mole $\nu_{\text{des}} \approx 4 \times 10^{16}$ s ⁻¹
$\theta=0.5$	linear	2052	c(2×2)	saturation coverage at 370 K
$\theta=0.75$	linear	2054 2031	p(4√2×√2)R45°	saturation coverage at 300 K
	bridge	1944		
$\theta=0.83$	linear	2074	c(6×2)	saturation coverage below 280 K at CO pressures above 5×10 ⁻⁷ mbar

even at low temperatures.

Upon desorption the overlayer with the c(6×2) pattern goes over in an overlayer were domains of the c(6×2) and p(4√2×√2)R45° structures coexist. Around 280 K an overlayer structure is left, in which only domains of the p(4√2×√2)R45° structure are present. At about 340 K some CO desorbs from this overlayer structure and the low frequency linear species disappears. Between 350 and 380 K bridged bonded CO desorbs and a c(2×2) structure is formed. Above 370 K, CO mainly occupies linear adsorption sites, from which it desorbs as the temperature is further increased.

It appears that in the adsorption mechanism of CO, a mobile precursor state is involved. The activation energy for desorption at low coverages is about 131 kJ/mole, and the preexponential factor for desorption is in the range of 4×10¹⁶ s⁻¹.

References

- [1] C.W. Tucker, *J. Appl. Phys* **37**, 3013 (1966).
- [2] B.A. Gurney, L.J. Richter, J.S. Villarrubia and W. Ho, *J. Chem. Phys.* **87**, 6710 (1987).
- [3] D.G. Castner, B.A. Sexton, G.A. Somorjai, *Surf. Sci.* **71**, 519 (1978).
- [4] Y. Kim, H.C. Peebles and J.M. White, *Surf. Sci.* **114**, 363 (1982).
- [5] L.J. Richter, B.A. Gurney and W. Ho, *J. Chem. Phys* **86**, 477 (1987).

- [6] L.-W.H. Leung, J.-W. He and D.W. Goodman, *J. Chem. Phys.* **93**, 8328 (1990).
- [7] R. Raval, M.A. Harrison and D.A. King, *J. Vac. Sci. Technol. A* **9**, 345 (1991).
- [8] R.G. Greenler, *J. Chem. Phys.* **44**, 310 (1966).
- [9] W.M. Daniel and J.M. White, *Surf. Sci.* **171**, 289 (1986).
- [10] For a comparative analysis see: M.A. Morris, M. Bowker and D.A. King in *Comprehensive chemical kinetics*, vol. **19**; C.H. Bamford, C.F.H. Tipper and R.G. Compton, Eds.; Elsevier, Amsterdam, p. 41-56, 1984.
- [11] P. Kisliuk, *J. Phys. Chem. Solids* **3**, 95 (1957).
- [12] M. Bowker, Q Guo and R. Joyner, *Surf. Sci.* **253**, 33 (1991).
- [13] P.A. Redhead, *Vacuum* **12**, 203 (1962).
- [14] C.-M. Chan, R. Aris and W.H. Weinberg, *Appl. Surf. Sci.* **1**, 360 (1978).
- [15] A.M. de Jong and J.W. Niemantsverdriet, *Surf. Sci.* **223**, 355 (1990).
- [16] F.M. Hoffmann, *Surf. Sci. Rep.* **3**, 107 (1983).
- [17] D.E. Peebles, H.C. Peebles and J.M. White, *Surf. Sci.* **136**, 463 (1984).
- [18] C.-T. Kao, C.M. Mate, G.S. Blackman, B.E. Bent, M.A. van Hove and G.A. Somorjai, *J. Vac. Sci. Technol. A* **6**, 786 (1988).
- [19] M.A. Van Hove, R.J. Koestner, J.C. Frost and G.A. Somorjai, *Surf. Sci.* **129**, 482 (1983).
- [20] L.H. Dubois and G.A. Somorjai, *Surf. Sci.* **91**, 514 (1980).
- [21] T.W. Root, G.B. Fisher and L.D. Schmidt, *J. Chem. Phys.* **85**, 4687 (1986).
- [22] S. Andersson, *Solid State Comm.* **21**, 75 (1977).
- [23] B.N.J. Persson and R. Ryberg, *Phys. Rev. B* **24**, 6954 (1981).
- [24] J.P. Biberian and M.A. van Hove, *Surf. Sci.* **118**, 443 (1982).
- [25] S. Andersson, *Surf. Sci.* **202**, 167 (1988).
- [26] J.E. Müller in *The chemical physics of solid surfaces*, vol. **6**; D.A. King and D.P. Woodruff, Eds.; Elsevier, Amsterdam, p. 33-36, 1993.
- [27] G. Brodén, G. Pirug and H.P. Bonzel, *Surf. Sci.* **72**, 45 (1978).

7 Summary and conclusions

In heterogeneous catalysis the properties of a catalyst are largely determined by the atomic composition and structure of the surface. Therefore, surface sensitive spectroscopies like X-ray photoelectron spectroscopy (XPS), secondary ion mass spectrometry (SIMS) and Auger electron spectroscopy (AES) yield relevant information on the performance of the catalyst. However, since most catalysts are complex systems, it is often difficult to apply these surface spectroscopies to their full potential. Model systems, then, provide a good means to study catalytic properties on a microscopic scale.

Catalyst characterization with surface sensitive spectroscopies yields information on the performance of a catalyst and on factors in catalyst preparation that influence the surface structure of the eventual catalyst. Most supported catalysts are porous and insulating materials, which limits the possibilities of those surface sensitive spectroscopies, that use charged particles, i.e. electrons or ions. Inhomogeneous charging of the catalysts then causes shifted and broadened peaks in XPS and AES spectra and makes the detection of secondary ions in SIMS difficult. Since catalysts are porous materials, a great deal of the surface is not accessible to surface spectroscopies and only the region near the outside of the particles can be studied. Sample charging can be avoided by using model supports, consisting of a flat conducting substrate with a thin oxide layer of a few nanometres thick on top of it. The active catalytic phase is applied on these model supports by the commonly used wet chemical techniques. Hence, these model catalysts are prepared in an as realistic as possible way, making that the separate preparation steps can be studied in detail. Since these model catalysts are flat, an additional advantage is that depth sensitive information can be obtained from angle-dependent XPS measurements and AES depth profiling.

In order to explore the possibilities of such model catalysts in catalyst characterization, the preparation of a silica supported zirconia catalyst has been studied with surface spectroscopies on a porous silica support as well as on a flat silica model support and the results obtained on both systems are compared. Two different preparation methods are studied; incipient wetness impregnation with an aqueous zirconium nitrate solution and a reaction of zirconium ethoxide, dissolved in ethanol, with the hydroxyl groups of the silica support. XPS measurements on the porous systems show that the latter method results in a well dispersed catalyst with a satisfactory thermal stability. Preparation by incipient wetness impregnation results in a much lower dispersed and less thermally stable catalyst. The results obtained with the porous support are in good agreement with those obtained with the model support. Angle-dependent XPS and AES depth profiling on the model catalysts confirm that the catalysts prepared from zirconium ethoxide contains a highly dispersed zirconium phase. It is demonstrated that model catalysts can be prepared by the same wet chemical procedures

as used in the preparation of real catalysts and that the results yielded from these model catalysts are in good agreement with those from real catalysts, however, the obtained information shows more detail. As such, these model catalysts are fulfilling systems to study catalyst preparation.

The approach of using model catalysts has also been adopted to study the sulfurization of silica supported molybdenum oxide catalysts. Sulfurization of molybdenum oxide to molybdenum sulfide is an essential step in the activation of hydrodesulfurization catalysts, used for the removal of sulfur and nitrogen from heavy oil fractions.¹ This sulfurization mechanism is studied on a silica supported molybdenum oxide model catalyst with atomic force microscopy (AFM), Rutherford backscattering spectrometry (RBS), XPS and SIMS. The molybdenum was applied on the model support by spincoating a molybdenum oxychloride solution. AFM showed that this results in disk-shaped molybdenum oxide particles of 5-10 nm thick. The sulfurization of these model catalysts in a mixture of 10% H₂S in H₂ at atmospheric pressure has been studied as a function of temperature. We note that the presented results are typical for the sulfurization of catalysts with a high water content. XPS and SIMS indicate the formation of Mo(IV) oxysulfides at the surface and Mo(IV) oxides in the interior of the particles at temperatures between 20 and 100 °C, whereas molybdenum sulfide forms at 125 °C and higher. Sulfur is present in two forms, as S²⁻ and S₂²⁻. The latter disappears between 150 and 200 °C. RBS analysis indicates S:Mo atomic ratios of 1 to 1.5 at sulfurization below 100 °C and of 2 to 2.5 above 100 °C. It is concluded that the sulfurization of MoO₃ to MoS₂ proceeds through a Mo(IV) oxysulfide, formed initially at the outside of the particles, and Mo(IV) oxide in the interior of the particles. Sulfidic species are believed to facilitate the reduction of MoO₃ to Mo(IV) species at low temperatures. Due to the high resolution that among all is obtained with XPS on these model catalysts the sulfurization could be studied in such a great detail, which was, until now, not possible on the industrial catalysts.

Single crystal surfaces can be used as a model for a catalytically active surface in a catalyst. Since the structure and composition of the surface are usually known on the atomic scale, single crystals are suitable to study adsorption, desorption and reaction processes in detail. Infrared spectroscopy is an attractive technique to study the state of adsorbed molecules. To be able to measure adsorbates on metal surfaces, infrared spectroscopy has to be performed in reflection. This technique is called reflection absorption infrared spectroscopy (RAIRS). An apparatus to perform RAIRS on adsorbates on metal single crystal surfaces under ultra high vacuum (UHV) and higher pressure (to 1 bar) conditions has been developed and built. The apparatus consists of an UHV chamber and a separate cell for the RAIRS experiments. In the UHV chamber the sample can be cleaned and characterized by low energy electron diffraction (LEED), AES and thermal desorption spectroscopy (TDS).

The interaction of carbon monoxide on rhodium with a (100) surface orientation has been studied as a function of temperature and CO pressure with RAIRS, LEED and TDS. At low coverages CO adsorbs predominantly in linear adsorption sites, till 0.5 monolayer (ML)

coverage, where a $c(2 \times 2)$ LEED pattern is observed. With increasing coverage bridged sites get increasingly occupied and at 300 K the surface is saturated at 0.75 ML coverage. At this coverage a $p(4\sqrt{2} \times \sqrt{2})R45^\circ$ LEED pattern is formed and CO occupies equal numbers of linear and bridged adsorption sites. Applying higher CO pressures at temperatures well below room temperature, the overlayer is further compressed into a $c(6 \times 2)$ structure with a coverage of 0.83 ML. This compressed structure is not formed at CO pressures below 5×10^{-7} mbar. Upon desorption the overlayer with the $c(6 \times 2)$ structure goes over in a state where domains with a $c(6 \times 2)$ and a $p(4\sqrt{2} \times \sqrt{2})R45^\circ$ LEED pattern coexist. Around 280 K an overlayer structure is left which exhibits only a $p(4\sqrt{2} \times \sqrt{2})R45^\circ$ LEED pattern. Between 350 and 380 K bridge bonded CO desorbs and a $c(2 \times 2)$ structure is formed. Above 370 K, CO mainly occupies linear adsorption sites, from which it desorbs as the temperature increases further. From TDS experiments appears that a mobile precursor state is involved in the adsorption mechanism of CO. The activation energy for desorption at low coverages is about 131 kJ/mole and the preexponential factor for desorption is in the range of $4 \times 10^{16} \text{ s}^{-1}$. The work illustrates that RAIRS, LEED and TDS form a powerful combination to study adsorbates on catalytic surfaces.

Samenvatting

In de heterogene katalyse worden de eigenschappen van een katalysator hoofdzakelijk bepaald door de atomaire samenstelling en structuur van het oppervlak. Oppervlakte-gevoelige spectroscopiën zoals röntgen foto-elektron spectroscopie (XPS), secundaire ionen massaspectrometrie (SIMS) en Auger elektronen spectroscopie (AES) geven daarom belangrijke informatie over de werking van de katalysator. De meeste katalysatoren zijn echter complexe systemen, waardoor het vaak moeilijk is deze oppervlakte-spectroscopiën optimaal toe te passen. Modelsystemen voorzien in een goede manier om katalytische eigenschappen op microscopische schaal te bestuderen.

De karakterisering van katalysatoren met oppervlakte-gevoelige spectroscopiën levert informatie op over het gedrag van de katalysator en over factoren in de katalysator-bereiding die van invloed zijn op de oppervlaktestructuur van de uiteindelijke katalysator. De meeste gedragen katalysatoren zijn poreuze niet geleidende materialen waardoor de mogelijkheden van die oppervlakte-gevoelige spectroscopiën die gebruik maken van geladen deeltjes (elektronen of ionen) beperkt zijn. Inhomogene oplading van de katalysator veroorzaakt verschoven en verbrede pieken in XPS en AES spectra en maakt de detectie van secundaire ionen met SIMS moeilijk. Omdat katalysatoren poreuze materialen zijn, is een groot deel van het oppervlak niet toegankelijk voor oppervlakte-spectroscopiën en kan alleen het buitenste gedeelte van de katalysatordeeltjes bestudeerd worden. Oplading van het monster kan voorkomen worden door gebruik te maken van modeldragers, die bestaan uit een vlak geleidend substraat met daar bovenop een dun oxydelagje van een paar nanometers dik. De katalytisch actieve fase wordt op deze modeldragers aangebracht d.m.v. de standaard nat-chemische methoden. Deze modelkatalysatoren worden dus op een zo realistisch mogelijke manier gemaakt, zodat de verschillende stappen in de bereiding in detail bestudeerd kunnen worden. Omdat deze modelkatalysatoren vlak zijn, is een bijkomend voordeel dat met hoekafhankelijke XPS en AES diepteprofileringen diepte gevoelige informatie verkregen kan worden.

Om de mogelijkheden van zulke modelsystemen bij de karakterisering van katalysatoren uit te zoeken, hebben we de bereiding van een silica-gedragen zirconia-katalysator bestudeerd met oppervlakte-spectroscopiën. We hebben dit zowel met een poreuze silica-drager als met een vlakke silica-modeldrager gedaan en de resultaten die op beide systemen verkregen werden met elkaar vergeleken. Er zijn twee verschillende bereidingsmethoden bestudeerd; porievolume impregnatie met een waterige zirkoonnitraat oplossing en een reactie van zirkoon-ethoxide, opgelost in ethanol, met de hydroxyl groepen van de silica-drager. XPS metingen aan de poreuze drager laten zien dat de laatste methode resulteert in een goed gedispergeerde katalysator met voldoende thermische stabiliteit. De bereiding via de

porievolume impregnatie levert een veel minder disperse en minder thermisch stabiele katalysator op. De resultaten verkregen met de poreuze drager komen goed overeen met die van de modeldrager. Hoek-afhankelijke XPS en AES diepte profilering aan de modelkatalysatoren bevestigen dat de katalysatoren bereid uit zirkoon-ethoxide een hoog disperse zirkoonfase bevatten. Het blijkt dat modelkatalysatoren gemaakt kunnen worden met dezelfde nat-chemische methoden die voor de bereiding van echte katalysatoren worden gebruikt en dat de resultaten die op deze modelkatalysatoren behaald worden goed overeenkomen met de resultaten van echte katalysatoren, terwijl met de modelsystemen meer gedetailleerde informatie verkregen wordt. Als zodanig zijn deze modelkatalysatoren dus zeer geschikt om de bereiding van katalysatoren te bestuderen.

De aanpak om modelkatalysatoren te gebruiken is ook toegepast om de inzwaveling van silica-gedragen molybdeenoxide-katalysatoren te bestuderen. Het inzwavelen van molybdeenoxide tot molybdeensulfide is een belangrijke stap in de activering van ontzwavelingskatalysatoren, die gebruikt worden voor het verwijderen van zwavel en stikstof uit zware aardolie-fracties. Dit inzwavelingsmechanisme is bestudeerd op silica-gedragen molybdeenoxide-modelkatalysatoren met atoom kracht microscopie (AFM), Rutherford terugverstrooiing spectrometrie (RBS), XPS en SIMS. Het molybdeen werd op de modeldrager aangebracht door een molybdeenoxychloride oplossing te spincoaten. AFM metingen lieten zien dat dit resulteert in schijfvormige molybdeenoxide-deeltjes van 5 tot 10 nm dik. Het inzwavelen van deze modelkatalysatoren in een 10% H₂S in H₂ mengsel bij atmosferische druk werd gevolgd als functie van de temperatuur. We merken hierbij op dat de gepresenteerde resultaten kenmerkend zijn voor de inzwaveling van katalysatoren met een hoog watergehalte. XPS en SIMS metingen duiden op de vorming van Mo(IV) oxysulfides aan het oppervlak en Mo(IV) oxydes binnenin de deeltjes bij temperaturen tussen de 20 en 100 °C, terwijl bij 125 °C en hoger molybdeensulfide wordt gevormd. Zwavel is in twee vormen aanwezig, S²⁻ en S₂²⁻, welke laatste verdwijnt tussen 150 en 200 °C. RBS laat zien dat de atomaire verhouding van S:Mo tussen 1 en 1.5 ligt bij inzwaveling beneden 100 °C en tussen 2 en 2.5 boven 100 °C. We concluderen dat de inzwaveling van MoO₃ naar MoS₂ via een Mo(IV) oxysulfide verloopt, dat aanvankelijk aan de buitenkant van de deeltjes gevormd wordt, en een Mo(IV) oxyde binnenin de deeltjes. Sulfides worden geacht de reductie van MoO₃ tot Mo(IV) bij lage temperaturen te bevorderen. Onder andere door de hoge resolutie die met XPS behaald werd op deze modelkatalysatoren, kon de inzwaveling gedetailleerd bestudeerd worden, wat tot nog toe op de industriële katalysatoren niet mogelijk was.

Eenkristal-oppervlakken kunnen gebruikt worden als model voor een katalytisch actief oppervlak in een katalysator. Omdat de structuur en samenstelling meestal op atomaire schaal bekend zijn, zijn eenkristallen zeer geschikt voor gedetailleerde studies aan adsorptie, desorptie en reactie processen. Infrarood spectroscopie is een aantrekkelijke techniek om de toestand van geadsorbeerde moleculen te onderzoeken. Om te kunnen meten aan adsorbaten op metaaloppervlakken, moet infrarood spectroscopie in reflectie uitgevoerd worden. Deze

techniek wordt reflectie absorptie infrarood spectroscopie (RAIRS) genoemd. Een apparaat om RAIRS experimenten aan adsorbaten op metaal eenkristal-oppervlakken onder ultra-hoog vacuüm (UHV) condities en bij hogere drukken (tot 1 bar) te kunnen uitvoeren is ontwikkeld en gebouwd. Het apparaat bestaat uit een UHV-kamer en een aparte cel voor de RAIRS experimenten. In de UHV kamer kan het monster worden schoongemaakt en gekarakteriseerd met lage energie elektronen diffractie (LEED), AES en thermische desorptie spectroscopie (TDS).

De interactie van koolmonoxyde met rhodium met een (100) georiënteerd oppervlak is bestudeerd als functie van de temperatuur en de CO druk met RAIRS, LEED en TDS. Bij lage bedekkingen adsorbeert CO voornamelijk in lineaire adsorptie-sites, tot een bedekking van 0.5 monolaag (ML), waar een $c(2 \times 2)$ LEED-patroon wordt waargenomen. Bij toenemende bedekking worden gebrugde sites meer en meer bezet en bij 300 K is het oppervlak verzadigd, bij een bedekking van 0.75 ML. Bij deze bedekking wordt een $p(4\sqrt{2} \times \sqrt{2})R45^\circ$ LEED-patroon gevormd en bezet CO een gelijk aantal lineaire en gebrugde sites. Bij hogere CO drukken en temperaturen ruim onder kamertemperatuur wordt de adsorbaatlaag verder verdicht in een $c(6 \times 2)$ structuur met een bedekking van 0.83 ML. Deze verdichte structuur wordt niet gevormd bij CO drukken lager dan 5×10^{-7} mbar. Tijdens desorptie gaat de adsorbaatlaag met de $c(6 \times 2)$ structuur over in een toestand waar domeinen met een $c(6 \times 2)$ en een $p(4\sqrt{2} \times \sqrt{2})R45^\circ$ structuur gelijktijdig voorkomen. Rond 280 K is er een adsorbaatlaag over gebleven die alleen een $p(4\sqrt{2} \times \sqrt{2})R45^\circ$ patroon geeft. Tussen 350 en 380 K desorbeert gebrugd gebonden CO en wordt een $c(2 \times 2)$ structuur gevormd. Boven 370 K bezet CO hoofdzakelijk nog lineaire adsorptie-sites, waarvan het desorbeert als de temperatuur verder wordt verhoogd. Uit TDS-experimenten blijkt dat er een mobiele precursortoestand is betrokken bij het adsorptiemechanisme van CO. De activeringsenergie voor desorptie is ongeveer 131 kJ/mol en de preëxponentiële factor voor desorptie ligt in de buurt van $4 \times 10^{16} \text{ s}^{-1}$. Het werk laat zien dat RAIRS, LEED en TDS een krachtige combinatie vormen om adsorbaten op katalytische oppervlakken te bestuderen.

Publications

Comparative test of procedures for thermal desorption analysis.

A.M. de Jong and J.W. Niemantsverdriet, *Vacuum* **41**, 232 (1990).

Thermal desorption analysis: comparative test of ten commonly applied procedures.

A.M. de Jong and J.W. Niemantsverdriet, *Surface science* **233**, 355 (1990).

Preparation of zirconium oxide on silica and characterization by X-ray photoelectron spectroscopy, secondary ion mass spectrometry, temperature programmed oxidation and infrared spectroscopy.

A.C.Q.M. Meijers, A.M. de Jong, L.M.P. van Gruijthuisen and J.W. Niemantsverdriet, *Applied catalysis* **70**, 53 (1991).

Preparation of ZrO_2 on flat, conducting $SiO_2/Si(100)$ model supports by wet chemical techniques; X-ray photoelectron spectroscopy and Auger depth profiling.

L.M. Eshelman, A.M. de Jong and J.W. Niemantsverdriet, *Catalysis letters* **10**, 201 (1991).

Preparation and surface characterization of silica supported ZrO_2 catalysts; comparison of layered model systems with powder catalysts.

A.M. de Jong, L.M. Eshelman, L.J. van IJzendoorn and J.W. Niemantsverdriet, *Surface and interface analysis* **18**, 412 (1992).

Evaluation of take-off angle-dependent XPS for determining the thickness of passivation layers on aluminium and silicon.

P.L.J. Gunter, A.M. de Jong, H.J.H. Rheiter and J.W. Niemantsverdriet, *Surface and interface analysis* **19**, 161 (1992).

Sulfidation mechanism of molybdenum catalysts supported on an $SiO_2/Si(100)$ model support studied by surface spectroscopy.

A.M. de Jong, H.J. Borg, L.J. van IJzendoorn, V.G.F.M. Soudant, V.H.J. de Beer, J.A.R. van Veen and J.W. Niemantsverdriet, *Journal of physical chemistry* **97**, 6477 (1993).

Improved activity of a silica supported ruthenium catalyst by CO pretreatment.

T. Koerts, J.H.M.C. van Wolput, A.M. de Jong, J.W. Niemantsverdriet and R.A. van Santen, *Applied catalysis*, accepted for publication (1994).

The adsorption of CO on Rh(100)

A.M. de Jong and J.W. Niemantsverdriet, submitted for publication to the *Journal of chemical physics* (1994).

Dankwoord

Vanwege hun betrokkenheid bij het tot stand komen van dit proefschrift, wil ik graag de volgende mensen bedanken. Mijn promotoren en copromotor: Rutger van Santen, Rob van Veen en Hans Niemantsverdriet. Mijn collega's: Herman Borg, Rob Gubbels, Pieter Gunter, Martijn van Hardeveld, Ton Janssens, Hannie Muijsers, Tiny Verhoeven, Thomas Weber en de rest van TAK voor de prima tijd die ik gehad heb. Tamara Ast, Lyn Eshelman, Toon Meijers, Mirjam van Rij en Vincent Soudant voor hun bijdragen aan dit proefschrift. San de Beer voor de vele nuttige discussies bij het molybdeen werk. Leo van IJzendoorn voor de RBS metingen. Lud Antonie, Carlo Battistella, Mark van der Leur, Jeroen Mathijssen, René van Oosterhout, Adri Pelders en Arjen Vromans voor het vele programmeerwerk en de automatisering van diverse opstellingen. Wout van Herpen voor al het werk en de hulp bij het bouwen van de RAIRS opstelling. De CTD, met name Peer Brinkgreve, Theo Maas, Rob van den Berg, Piet van den Hoogen en Meindert Janszen voor de vele klussen en goede ideeën. Jan Wiggers voor de bouwtekeningen van de preparatie-kamer van de SIMS. Toon van Kleef, Henk van Lieshout en Bart Michiels voor alle hulp bij de vele bestellingen.

Curriculum vitae

Arthur de Jong werd geboren op 31 juli 1966 te Dordrecht. In 1984 behaalde hij het Atheneum-B diploma aan de Rijks Scholen Gemeenschap te 's-Hertogenbosch. In datzelfde jaar begon hij de studie Scheikundige Technologie aan de Technische Universiteit Eindhoven. Zijn afstudeer-onderzoek deed hij bij de vakgroep Anorganische Chemie en Katalyse. Dit betrof het testen van analyse methoden op gesimuleerde thermodesorptie spectra en het bouwen van een vacuüm opstelling voor thermodesorptie spectroscopie. In juni 1989 behaalde hij het ingenieursdiploma. Op 1 september 1989 startte hij zijn promotie-onderzoek in dienst van NWO, bij de vakgroep Anorganisch Chemie en Katalyse aan de Technische Universiteit Eindhoven.

Stellingen

behorende bij het proefschrift

Surface spectroscopy of model catalysts

A.M. de Jong

- 1 Desorptieparameters kunnen alleen op een betrouwbare manier uit thermische desorptiespectra verkregen worden met methoden die rekening houden met de bedekkingsgraadafhankelijkheid van deze parameters.
A.M. de Jong and J.W. Niemantsverdriet, Surf. Sci. **233**, 355 (1990).
- 2 Het bepalen van de bedekkingsgraad als functie van de gasdosering aan de hand van LEED patronen kan gemakkelijk resulteren tot een foutieve verzadigingsbedekking.
Y. Kim, H.C. Peebles and J.M. White, Surf. Sci. **114**, 363 (1982).
- 3 Leung e.a. kennen de twee IR absorptiebanden van lineair gebonden CO van CO geadsorbeerd op Rh(100) toe aan domeinen met verschillende lokale CO bedekking. Zij ondersteunen dit met het feit dat er twee domeinen met een $p(4\sqrt{2} \times \sqrt{2})R45^\circ$ LEED structuur bestaan. Hun toekenning kan niet juist zijn daar in beide domeinen de bedekking gelijk moet zijn.
L.-W.H. Leung, J.-W. He and D.W. Goodman, J. Chem. Phys. **93**, 8328 (1990).
- 4 De beschrijving van molekuul-trillingen in termen als *collapsing pianostool* maken de vibratie spectroscopie niet inzichtelijker, maar zeggen meer over de fantasie van de auteurs.
M.A. Chesters, S.F. Parker and R. Raval, J. Elec. Spectr. Rel. Fenom. **39**, 155 (1986).

- 5 De door Kennedy en Hamnett met XPS waargenomen Pt-oxides op Pt:C electrodes zijn ontstaan of beïnvloed door het transport door de lucht van de electrochemische cel naar de XPS spectrometer.
B.J. Kennedy and A. Hamnett, J. Electroanal. Chem. **283**, 271 (1990).
- 6 De tweede zuurstof piek bij 532 eV in XPS spectra van ZnO films wordt door Meng e.a. toegeschreven aan OH of H₂O. Gezien het feit dat in het XPS overzichtsspectrum pieken van silicium aanwezig zijn is het aannemelijker dat deze zuurstof piek afkomstig is van het glas substraat.
L.-J. Meng, C.P. Moreira de Sá and M.P. dos Santos, Appl. Surf. Sci. **78**, 57 (1994).
- 7 De door Iida en Abe geobserveerde oxidatie van titaan dat is afgezet op een SiO₂ film wordt niet veroorzaakt door een reactie met het SiO₂, daar de getoonde AES sputter-diepteprofielen laten zien dat de titaanlaag is geoxideerd aan het oppervlak en niet aan het Ti-SiO₂ interface.
S. Iida and S. Abe, Appl. Surf. Sci. **78**, 141 (1994).
- 8 Gezien de afmetingen van de *tip* waarmee met AFM een oppervlak wordt gescand is het niet zonder meer te verwachten dat dit met atomaire resolutie wordt afgebeeld.
- 9 De campagne van de overheid tegen vreemdelingenhaat en voor meer begrip voor allochtonen strookt niet met haar politieke beleid.
- 10 Naarmate tekstverwerkingsprogramma's meer zelf "nadenken", wordt het voor de gebruiker steeds moeilijker ermee te werken.